ENGINEERING RESEARCH INSTITUTE
UNIVERSITY OF MICHIGAN
ANN ARBOR

THE UNDERWATER SPARK:

AN EXAMPLE OF GASEOUS CONDUCTION AT ABOUT 10,000 ATMOSPHERES

by

Edward A. Martin

Approved by H. C. Early
Research Engineer
Project Supervisor

Approved by W. G. Dow
Professor of Electrical
Engineering, Chairman
of Doctoral Committee

Final Report

Contract Title "Arc Discharge
through a Liquid"

OFFICE OF ORDNANCE RESEARCH
ORDNANCE CORPS, U.S. ARMY
CONTRACT NO. DA-20-018-ORD-12242
ARMY PROJECT NO. 599-16-005
ORD Project No. TB 3-001(317)

Submitted in partial fulfillment of the requirements for the Degree
of Doctor of Philosophy in the University of Michigan

July, 1956

PREFACE

Throughout the following dissertation I have presented the experimental data and the calculated results in greater detail than the bare minimum which would be necessary for adequate coverage of the subject matter. This serves two purposes. From the experimental data, others may be able to develop competing theories which explain the data more completely than the theory presented here. Also, the final conclusions may be directly utilized by others for the purpose of interpreting their own experimental observations. The reader is therefore free to select information from any part of this study which is applicable to his needs or interests.

I am grateful for the willing assistance and advice contributed by the members of my doctoral committee, Professors S. S. Attwood, R. C. F. Bartels, J. M. Cork, L. N. Holland, and especially the committee chairman, Professor W. G. Dow. I also appreciate the administrative policy adopted by Mr. H. C. Early, project supervisor. In addition to attending to administrative details he contributed many suggestions of a technical nature, especially concerning high-voltage laboratory techniques. Thanks are also due Professor G. Hok for his participation in discussions throughout the course of the work.

The major portion of this work was supported by funds from the Office of Ordnance Research, U. S. Army, as a study in basic science.

Ann Arbor, Michigan
July, 1956

Edward A. Martin

TABLE OF CONTENTS

LIST OF TABLES

LIST OF ILLUSTRATIONS

ABSTRACT

The underwater spark is treated as a problem in gaseous electrical conduction at pressures of the order of 10,000 atmospheres. Four basic spark parameters are determined as functions of time: the channel size, the energy input, the pressure, and the temperature. These four quantities permit carrying out a particle balance and an energy balance as functions of time. The mutually consistent results provide an extension of the theory of gaseous conduction into the domain of extremely high pressures.

The four basic quantities were obtained as follows: The channel size was scaled from quarter-microsecond Kerr cell photographs of the spark. The spark energy input was obtained by a circuit energy balance in terms of spark current and discharge circuit parameters. The channel pressure was calculated from the rate of channel expansion and the hydrodynamic characteristics of water. The channel temperature was obtained from absolute measurements of radiation by means of phototubes. These four quantities provide information from which the energy stored in the spark channel may be calculated by two independent procedures. First, the significant energy losses from the channel may be subtracted from the measured energy input. The mechanical work to generate the shock wave in the water was found to be the greatest energy loss. Radiation was found to be a smaller, but appreciable, loss. Thermal conduction was found to be negligible. Second, the spark-channel energy may be obtained from the solution of a simultaneous set of particle-balance equations. These equations, including Saha thermal-ionization equations and Boltzmann's relations, yield the amount of dissociation, excitation, and ionization in the channel. The channel energy computed by these two methods is given as a function of time.

The following conclusions were reached concerning the underwater spark as produced by the discharge of a 5.8-microfarad capacitor charged to 25 kilovolts. The peak current is 85,000 amperes. At the moment of peak current the channel external pressure, including average pinch pressure, is 8330 atmospheres. The channel is in thermal equilibrium and radiates diffusely a continuum corresponding to a blackbody at about 29,900°K. The total particle density in the channel is approximately 2×10^{27} per cubic meter. The particles consist primarily of dissociated oxygen and hydrogen; and the degree of ionization is 30 percent. The major portion of the spark input energy is initially stored within the channel in the form of kinetic energy and energy of dissociation, excitation, and ionization. This energy is then relatively slowly dissipated in the form of mechanical work to the shock wave and in thermal radiation. There is evidence that the spark plasma has an internal pressure due to Coulomb interparticle forces; an approximate calculation of this pressure is carried out. Channel magnification caused by refraction in the compressed shock wave is found to be appreciable.

The Kerr cell photographs reveal the formation of spherical structures on the spark electrodes under certain conditions. These have not been previously reported. A short discussion of them is included. Their presence is ascribed to the highly polar nature of the water molecule.

The experimental value of plasma electrical conductivity is compared to values calculated from the work of Gvosdover and of Spitzer and Harm for completely ionized gases. The agreement is excellent. The theory of Spitzer and Harm is also applied to thermal conductivity in the plasma. It is concluded that wall recombination is more than ample to supply the required energy to vaporize water at the spark-channel wall. Various applications of the underwater spark are discussed, such as its use as a light source, as a sonic source, or for punching metal. Finally a discussion and derivation of the Saha thermal-ionization equation are included.

CHAPTER I

INTRODUCTION

Knowledge of the subject of electrical discharge in gases is in an early stage of development at the present time. This early period is characterized by a high ratio of empirical knowledge to theoretical knowledge. A large proportion of the present effort in this field is devoted to assembly of empirical data on the variation of such quantities as mobility, collision cross section, mean free path, and ionization coefficient as functions of such parameters as pressure, type of gas and impurities, electrode geometry, and applied electric and magnetic fields. While such information is useful in the design of new gas-discharge devices, it is generally not of direct value for clarifying the detailed physical processes taking place within the gas-discharge plasma. This is primarily a consequence of the difficulty of experimentally isolating a single physical phenomenon for study. An outstanding example of this situation is provided by the second Townsend coefficient. Many years have elapsed since electrical conduction in gases was first analyzed, but it is still not definitely known whether the feedback factor which causes emission of electrons from the cathode of a glow discharge, and hence renders the discharge self-maintaining, is the result primarily of ion bombardment, photoemission, or emission produced by metastable atoms. Of course, one may in principle set up simultaneous mathematical relations describing all possible physical processes which could conceivably take place in a discharge plasma; but the result would be a vastly complex set of equations, much too difficult to treat analytically. Furthermore,

advancement of knowledge in the field of gas discharges has been hampered by the attraction of qualified research personnel to newer, rapidly expanding fields of physical research such as solid-state and nuclear engineering. Recently, however, interest has been increasing in the production of high temperatures in the laboratory. An electric arc or spark will provide a highly ionized region at high temperature which is somewhat analogous to a nuclear explosion or to the ionized regions of space. The production of diamonds, which has recently been announced, is carried out in a high pressure electrical discharge. Perhaps a revived interest in the basic physics of electrical discharges will result in the growth of the more firm theoretical foundation which is necessary for a satisfactory understanding of the subject.

Low Pressure and High Pressure Electrical Discharges

Electrical discharges which are self-sustaining may be grouped into two major categories. The first category contains the low pressure discharges, which have pressures below approximately one-tenth atmosphere. These discharges are characterized by a low coefficient of thermal energy transfer between the electrons and the heavier particles of the plasma. The current density and input power density are typically low, and recombination of electrons and ions takes place primarily at the boundaries of the discharge region. The second category of electrical discharges contains the high pressure discharges, which have pressures above approximately one-tenth atmosphere. In discharges of this class, the coefficient of thermal energy transfer between the electrons and the heavier particles of the plasma is sufficiently high so that the two types of particles have substantially the same temperature. The current density and input power density are typically high, and recombination of

electrons and ions occurs chiefly throughout the volume of the discharge region. The field of low pressure discharges has received by far the major portion of research effort in the past, principally because low pressure discharges have been of greater commercial importance, and also because of the greater experimental difficulties encountered in studying high pressure discharges.

A large part of the research on high pressure discharges has been carried on under steady-state conditions; the notable exceptions to this are circuit-breaker and fuse studies, and lightning and overvoltage breakdown studies. In general, for steady-state discharges, the research worker in the field of high pressure discharges encounters the problems of supplying the required high rate of power input to the discharge, confining the discharge in order to maintain the high pressure, and removing energy from the confining container so that the walls and electrodes will not be destroyed by the high temperatures which are characteristic of such discharges. In addition, if the discharge is to be observed or photographed, one requires a transparent window material capable of withstanding the pressures and temperatures without distortion or damage.

The major research work in this country on high pressure steady-state discharges was carried out during the 1930's by Suits and associates. Using two methods to measure the velocity of sound in an arc plasma, Suits was able to calculate the temperature of the plasma (1, 2). His work encompassed a range of pressures from 1 to 1000 atmospheres, and currents from 1 to 10 amperes. Temperatures ranged from about 4000 to 10,000 degrees Kelvin. Suits was also able to obtain the discharge voltage gradients by use of a vibrating electrode (3). Gradients were

found to be as high as about 300 volts per centimeter. On the basis of recent literature, it appears that most of the present work on steady-state high pressure discharges is being done in Germany. Burhorn, Maecker, and Peters have studied arcs confined within the void produced by the centrifugal forces of rotating water (4). Most of the work was done at atmospheric pressure, and arc temperatures of 50,000 degrees Kelvin were measured at currents of 1500 amperes. The temperatures were determined from relative intensities of spectral lines. A modification of the apparatus permitted measurements to be made at pressures up to 1000 atmospheres (5). In this case a 200-ampere arc radiated a continuous spectrum similar to that of a blackbody at 12,000 degrees Kelvin. The temperature was measured by the amount of broadening of hydrogen spectral lines. Elenbaas in Holland has reported a large amount of work on mercury vapor discharges confined by quartz and hard glass tubes at pressures up to 200 atmospheres (6). Again temperatures were of the order of 4000 to 6000 degrees Kelvin.

The production of high-power, high-pressure arcs is more easily accomplished on a transient basis. Energy may be stored relatively slowly, and then transferred rapidly to the discharge channel. Measurements can be taken before the pressure-confining walls of the discharge chamber or the electrodes are appreciably vaporized, and photographs taken before damage occurs to a transparent window. However, all measurements then become dynamic measurements, and the sensitivity of the measuring equipment must often be sacrificed for speed of response. Furthermore, the measuring equipment must operate in proximity to rapidly varying electric and magnetic fields; the research is encumbered by isolation and grounding problems. The many researches on exploding wires

are studies of transient high pressure discharges, the usual technique being to discharge a capacitor through a wire to produce a high pressure arc in the wire-metal vapor. Some of the classic works in this field are those of Anderson and Smith (7), Conn (8), Eiselt (9), and O'Day. These studies, though usually performed at atmospheric pressure, are actually concerned with discharges at pressures substantially above atmospheric, since the accompanying loud sonic report when the discharge takes place confirms that a high pressure shock wave has been produced in the air by the rapid expansion of the spark channel. Glaser has presented excellent work on sparks in various gases at pressures up to 16 atmospheres (10, 11). He reports temperatures of the order of 40,000 degrees Kelvin on the basis of radiation measurements.

The Underwater Spark

The subject of this dissertation, the underwater spark, is produced experimentally by causing electrical breakdown to take place between electrodes submerged in a water tank. The energy for the discharge is stored in capacitors in the present case, but similar studies could be carried out with the energy stored in inductors or in rotating machinery. As energy is rapidly transferred to the spark channel, its temperature and pressure rise. In contrast to sparks in a fluid medium of low mass density, such as a gas, the mechanical inertia of the water exerts a nearly rigid opposition to the spark-channel expansion. The result is that extremely high pressures are developed due to the confining action. For the experimental parameters involved in the present study the pressures exceed 10,000 atmospheres. The underwater spark therefore provides a means of studying gaseous conduction at pressures which are a factor of ten greater than in any of the work which has been reported

previously in the scientific literature.

The underwater spark has been used for many years as a spectroscopic light source (12). A small capacitor, charged from a high-voltage transformer, was connected across closely spaced underwater electrodes. A succession of "condensed" sparks of several joules per discharge were thus produced. In spite of the low stored energy per discharge, the light which was emitted had a continuum in the ultraviolet suitable for spectroscopic absorption studies.

Very little work has been done on the detailed characteristics of underwater sparks. Wilson has measured the relative intensities of OH absorption bands in the spectrum of an underwater spark (13). On this basis he concludes that the temperature is about 5000 degrees. This is probably low, because the absorption would take place in the cooler outer layers of the channel in a manner analogous to the formation of Fraunhofer lines in the solar spectrum. Wyneken measured the continuous spectrum of the underwater spark and concluded that the spectral distribution is most like that of a blackbody at 10,000 degrees Kelvin (14). The research staff of Westinghouse has recently investigated the use of water in circuit breakers; but there is apparently little practical application for them, probably because of evaporation, freezing, and corrosion problems (15). Früngel has published a paper on the mechanical effectiveness of underwater sparks, which dealt with the height of vertical projection of a known weight by the pressure pulse from the spark (16). He reports that one percent of the energy stored on the capacitors may be converted to mechanical work to lift the weight. More recently, Rust and Drubba have studied the underwater spark as a sound source; this subject will be discussed later, in the chapter on applica-

tions (17). Otherwise, when the present investigation was undertaken, very little was known about the pressures, temperatures, particle densities, degree of ionization, and other properties of an electrical discharge in the 10,000-atmosphere pressure range as characterized by the underwater spark.

The objective of the present investigation has been to ascertain as many characteristics of an extremely high pressure discharge as possible in order to furnish a foundation for the planning of possible future studies. In carrying out the work, ultimate accuracy of the data was not sought; the emphasis has been placed on reliability of the data. For planning purposes, reliable information to one significant figure is much more desirable than an accuracy of two or three significant figures in which questionable methods or assumptions are involved. In most cases data will be presented in terms of three significant figures. This should not be interpreted as an implication that the data has three-figure accuracy, rather, it was done to reduce the accumulation of round-off error in the calculations which have been made or in those which others may wish to make. In general the final calculated results are believed to be accurate to at least one significant figure, and in some cases to two significant figures.

The rationalized MKS system of units will be used throughout, with the following two exceptions: Pressures will be expressed in atmospheres rather than in newtons per square meter, and inch or centimeter units will occasionally be used in the body of the text when the use of meter units would be awkward. A pressure of one atmosphere is very closely equal to 10^5 newtons per square meter.

Summary of Characteristics of Underwater Spark Used in This Study

In order to serve as an orientation as to the ranges of the various spark parameters to expect later, the finally determined characteristics of the underwater spark will be summarized. The spark as discussed in this dissertation is produced by a 5.8-microfarad capacitor charged to 25 kilovolts. The copper electrodes are spaced 1.5 centimeters apart, and the spark is initiated by a one-mil tungsten wire. The orienting magnitudes occurring at the current maximum, 1.9 microseconds after initiation of current flow, are as follows:

The current is 85,000 amperes.

The channel diameter is 2.51 millimeters.

The radiation consists of a continuous spectrum having a blackbody distribution corresponding to a temperature of 29,950 degrees Kelvin.

The electrical power input is 390 megawatts.

The average spark-channel pressure is 8330 atmospheres.

The total particle density is of the order of 2×10^{27} particles per cubic meter.

The particles are primarily dissociated oxygen and hydrogen, with a degree of single ionization of about 30 percent. Most of the electrical input energy to the underwater spark is stored within the channel in the form of dissociation, excitation, and ionization. During the early stages of the spark the major energy loss from the channel is that used in generating the shock wave. The radiation output, which persists for a long time on the microsecond time scale of the underwater spark, becomes the major loss during the later stages. There is evidence that there is an internal pressure in the spark plasma due to the interparticle Coulomb forces. Wall recombination appears to be important even though most of

the ion recombination occurs throughout the plasma volume.

Investigational Procedure

The general procedure employed in the investigation has been as follows. From a circuit analysis of the spark discharge circuit, the power input to the spark was obtained as a function of time. The result was checked by a circuit energy balance. Kerr cell camera photographs of the spark were used to obtain the channel size as a function of time. The spark-channel pressures as a function of time were obtained by hydrodynamic calculations based on the rate of expansion of the spark channel. The channel temperature was obtained as a function of time by measurement of the radiation. These four quantities, channel energy, size, pressure, and temperature, were sufficient to carry out a detailed energy balance for the spark plasma, again as a function of time. The Saha and Boltzmann relations played a significant part in this energy balance. The result is a self-consistent picture of the physical conditions in the plasma of an extremely high-pressure, high-power electrical discharge.

CHAPTER II

THE DISCHARGE CIRCUIT AND INSTRUMENTATION

The design of the basic equipment used for the study of the underwater spark is summarized by the block diagram in Fig. 1. The corresponding general view of the equipment is given in Fig. 2. In operation, the charging of the storage capacitors is begun after the physical underwater spark electrode setup is complete. When the desired voltage is reached, the charging current is decreased until it just compensates for leakage and corona loss. While the voltage is thus held at the desired value, the operator is free to pull the dark slide on the Kerr cell camera, open the oscilloscope camera shutter, and carry out any other last-minute operations which may be necessary. The manual air gap is then closed by means of a fiberglas cord, which completes the circuit and initiates the spark. After the transient is completed, the oscilloscope camera shutter is then closed, and the Kerr cell dark slide replaced.

The discharge circuit is shown in Figs. 3 and 4. When the equipment was in use, the five inverted storage capacitors at the top were surrounded by 3/4-inch boards to give protection in case one capacitor should short internally, resulting in the dissipation of the entire stored energy within the shorted capacitor. The supporting cabinet performs the dual function of protecting personnel from the high voltage and reducing the stray interference with the recording instruments. The access door of the cabinet was mechanically interlocked, and all other doors were bolted to prevent them from being opened inadvertently.

The particular discharge circuit used was evolved gradually through-

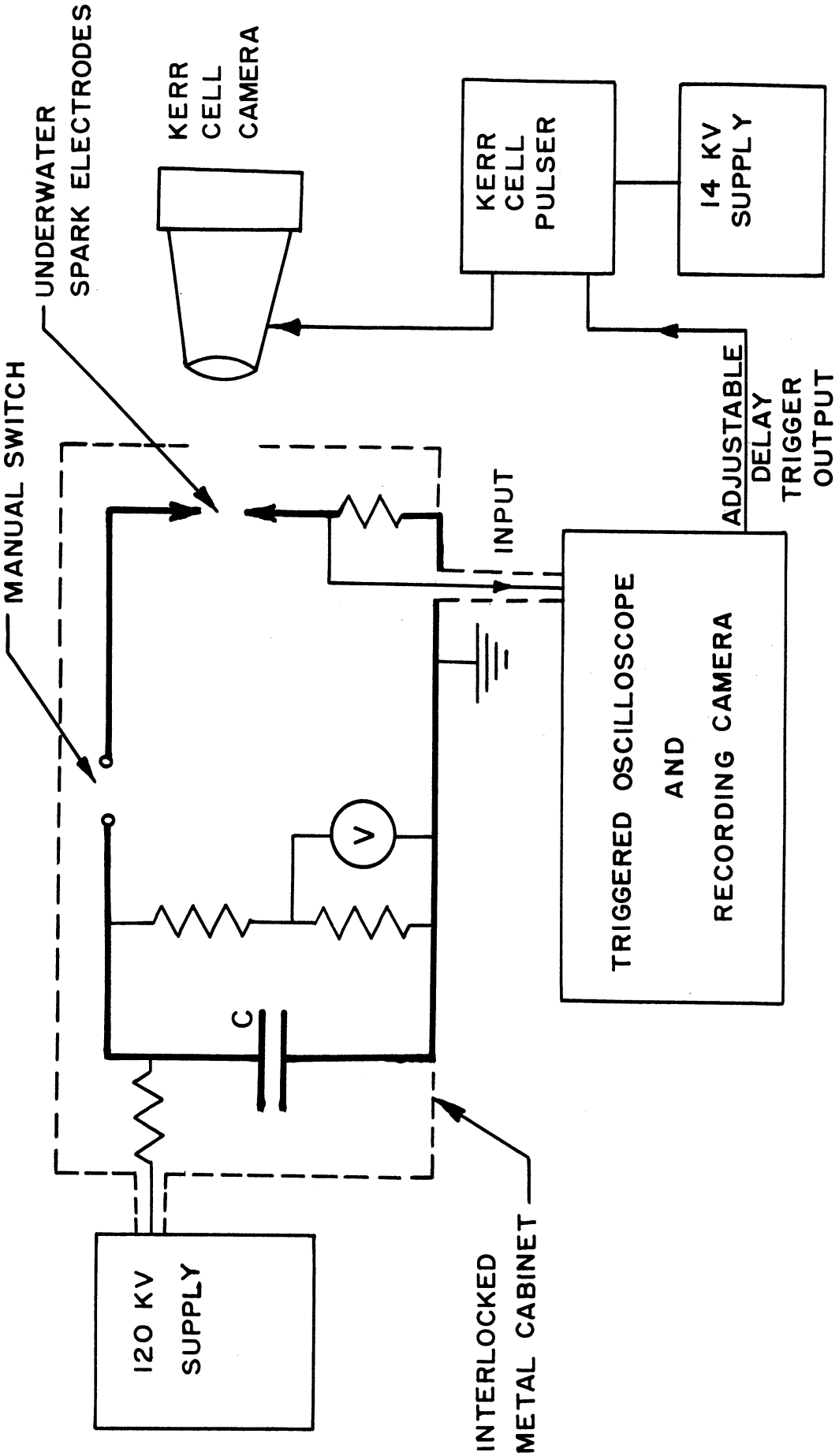

FIG. 1 BASIC DIAGRAM OF APPARATUS

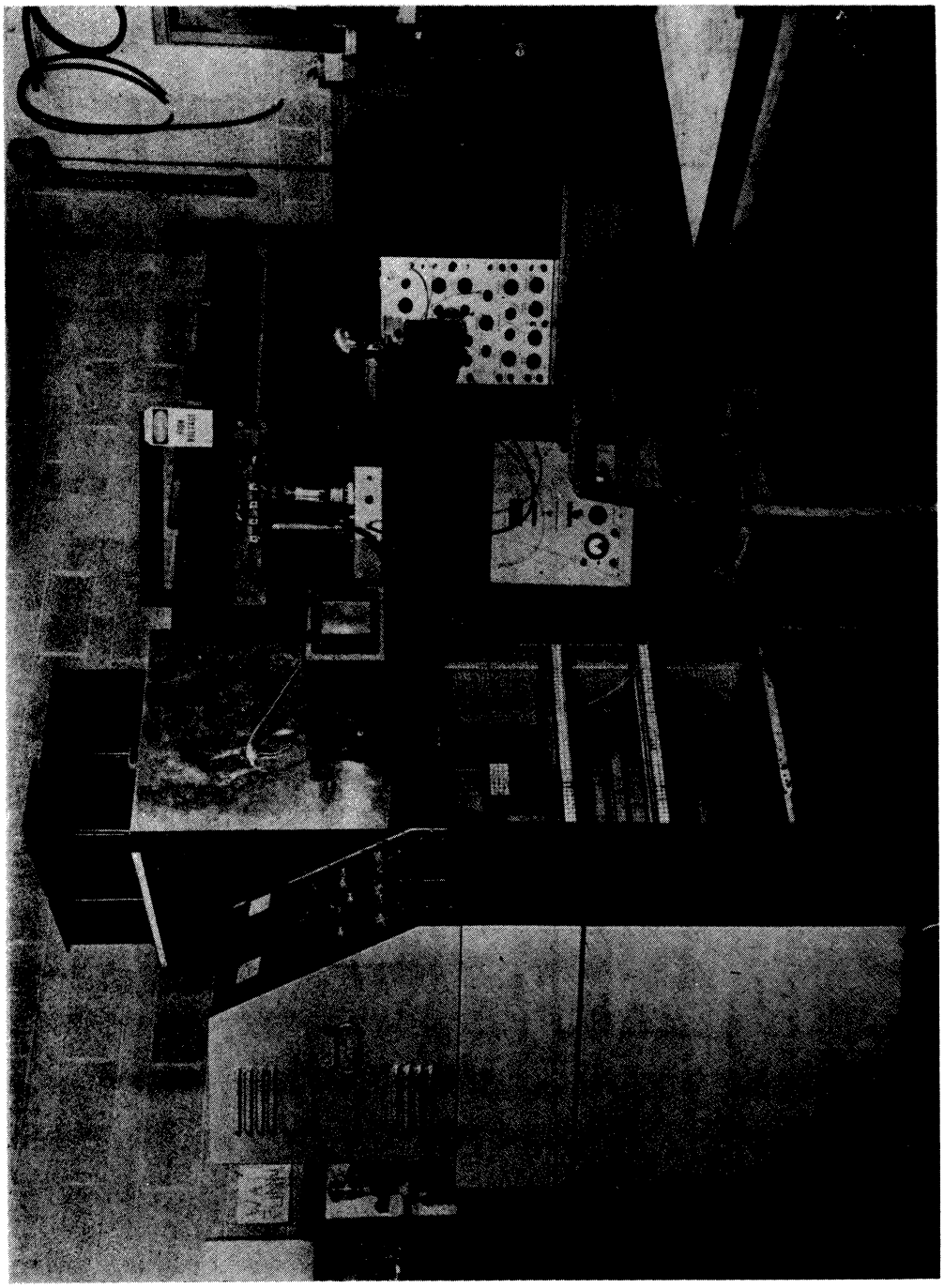

FIG. 2 GENERAL VIEW OF EQUIPMENT

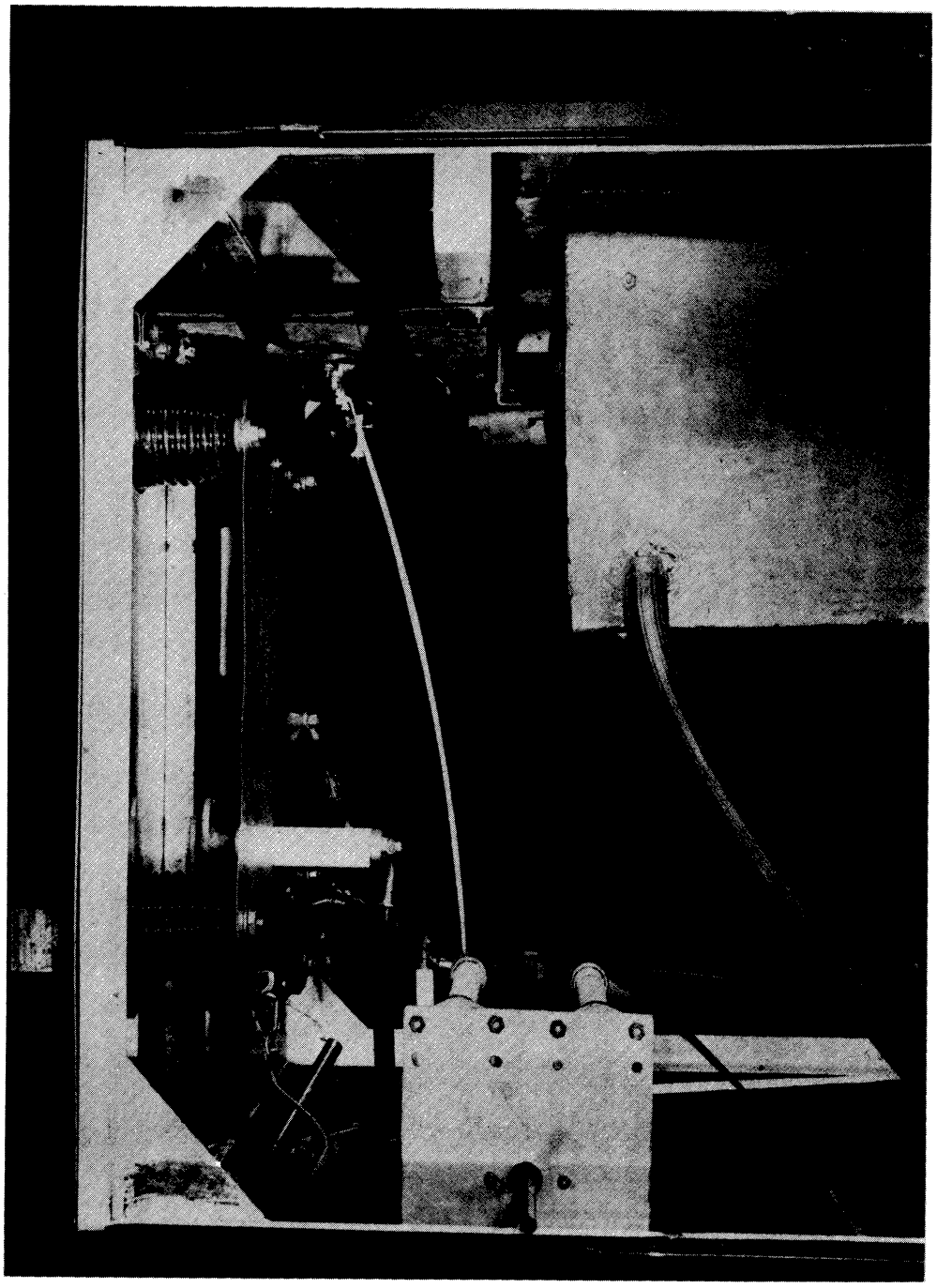

FIG. 3 THE DISCHARGE CIRCUIT

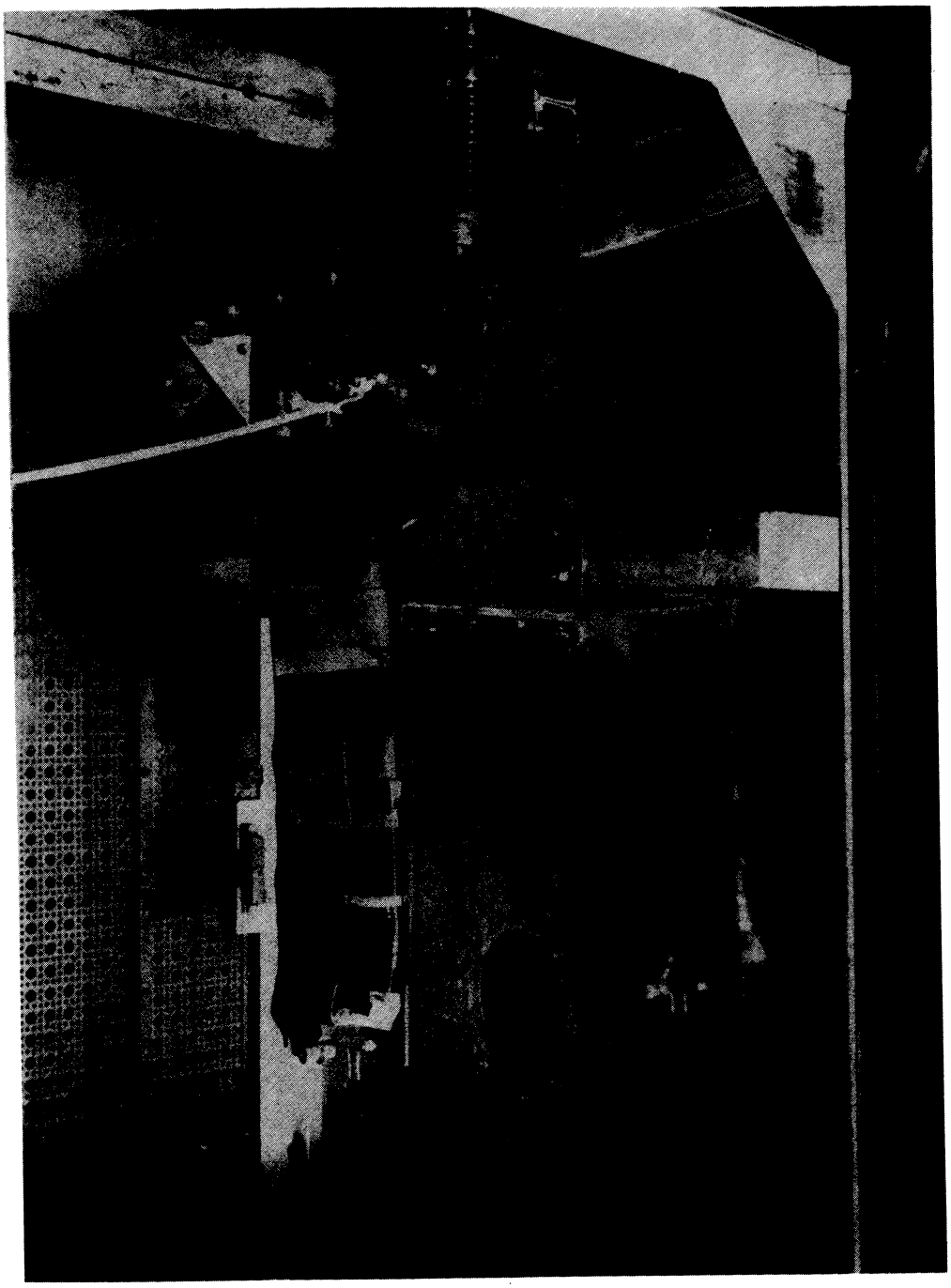

FIG. 4 THE DISCHARGE CIRCUIT
(TANK REMOVED)

out the course of the investigation as additional experience was acquired. Initial work was carried out with a capacitance of 11 microfarads charged to voltages under 10 kilovolts. Further work was done with 3/4 microfarad at 20 kilovolts, and with 1/2 microfarad charged to 50 kilovolts. The final discharge circuit, with which the measurements discussed in this dissertation were made, using 5.8 microfarads charged to 25 kilovolts, is designed for maximum rate of transfer of energy to the spark during its early stages.

The discharge circuit employs 5 GE Pyranol capacitors in parallel, each rated 25 kilovolts and one microfarad, and each having a measured internal inductance of about 1/3 microhenry. The measured total capacity of 5.8 microfarads gives a stored energy of 1810 joules. The effective series inductance of the circuit has been made as small as possible so that the initial rate of rise of current will be a maximum. By use of wide and closely spaced copper straps for leads the effective series inductance of the circuit has been limited to 0.26 microhenry as determined from the period of the current oscillations. The theoretical initial rate of current rise, 9.6×10^{10} amperes per second, is not quite attained. If the circuit had no resistance, the peak discharge current would be 118,000 amperes. The actual value as measured by the current shunt is 85,000 amperes. The state of charge of the storage capacitors is indicated by a five-kilovolt DC voltmeter connected across a five-to-one resistance voltage divider. The calibration of this divider and voltmeter combination was checked with an accurate electrostatic voltmeter (Rawson, Type 518C). The accuracy was found to be within several percent at full scale.

Instrumentation

The problem of electrical interference with the measuring equipment was a serious one. All units of the apparatus were grounded to a large aluminum sheet on the front of the cabinet. This sheet was then grounded to the building water system. Multiple grounding of any unit of equipment was found to be undesirable, since this resulted in a low impedance loop through which circulating currents could flow. Interference was confined within the cabinet as much as possible by having the minimum number of leads to the outside. For example, the interference was prevented from reaching the building power lines via the high-voltage supply by means of a 3-megohm charging resistor. Without such isolation, interference could enter the oscilloscope through its power cord. The signal lead to the oscilloscope, and the Kerr cell triggering leads, were coaxial cables. The shielding provided by the metal cabinets of the oscilloscope and Kerr cell pulser produced additional isolation. Checks were frequently made during the course of the investigation to confirm that the stray pickup was not causing a spurious signal on the oscilloscope.

The spark current oscillograms and the photocell light output traces were displayed by means of a Tektronix type 513D Cathode Ray Oscilloscope. This oscilloscope is specifically designed for observing fast single-sweep traces of rapid events. It has a 12-kilovolt accelerating potential on the cathode ray tube, and the fastest sweep rate is 0.1 microsecond per centimeter. The vertical amplification is by means of a direct-coupled push-pull distributed amplifier having a nominal bandpass from DC to 18 megacycles. Most work was carried out using only this amplifier. There is also a built-in RC-coupled preamplifier which was used for the photocell measurements. It operates single-ended and reduces the nominal

bandwidth to the range from 2 cycles to 16 megacycles. The distributed amplifier transient response permits satisfactory recording of a risetime of 0.025 microsecond (10 percent to 90 percent).

The oscilloscope sweep can be adjusted to be free running, or it may be triggered. The trigger signal may be obtained from the signal under observation, from any external source, or from a periodic internal source. All input signals are fed through a 1/4-microsecond delay network in order that the sweep may get underway and the spot be intensified before the amplified signal is applied to the vertical-deflection plates. There is also a trigger output with adjustable delay so that various equipments, such as the Kerr cell pulser in the present study, can be triggered at any desired time later than one microsecond after the sweep initiation.

The oscilloscope trace is very linear with time, nonlinearity being almost undetectable visually when a one-megacycle sine-wave signal is applied to the amplifier. There is an internal calibration voltage for determining the value of the continuously adjustable vertical-deflection sensitivity. The input impedance of the oscilloscope is nominally one megohm of resistance in parallel with 40 micromicrofarads of capacity, but a ten-to-one RC-compensated attenuator probe increases the effective impedance to 10 megohms in parallel with 14 micromicrofarads of capacity. In all applications in which the oscilloscope was used for measurements, a check was made for stray electromagnetic pickup. After a measurement was made, all equipment was left connected in the same relative position, the signal was blocked from reaching the oscilloscope, and the underwater spark was discharged as usual. It was found that in all measurements the stray pickup had been reduced to a completely negligible value.

The oscilloscope traces were recorded by means of a Dumont type 297 Polaroid Land Oscillograph Camera having a lens with an aperture of f.2.8. Conventional type 41 "Picture in a Minute" Polaroid film was used. This material has a photographic speed corresponding to the faster conventional films, about ASA 100. In order to record as fast a sweep as possible, and hence record more detail in the oscillograms, a cathode ray tube with a P-11 phosphor was obtained. This is a blue phosphorescent material made especially for photographic recording. As seen by the eye, the P-11 phosphor has no perceptible persistence. It was found necessary to pre-expose the type 41 film to remove its emulsion inertia in order to record single traces with a sweep speed of one microsecond per centimeter.

The current through the underwater spark was measured by means of a noninductive resistor connected in series with the spark. This current-viewing resistor, or current shunt, develops a voltage proportional to current, which may be displayed on the oscilloscope. The shunt is a folded-ribbon type designed by H. C. Early. It has excellent electrical and mechanical characteristics and is relatively easy to construct as compared to the coaxial type shunts.

A photograph of the shunt is shown in Fig. 5, and the method of construction in Fig. 6. Several strips of Chromel ribbon are folded as shown, and the tabs are brazed to the edges of the two copper plates. The width, length, and number of ribbons depend on the amount of resistance desired. Three very thin strips of clear mica are inserted as shown so that the Chromel ribbons are insulated. The entire assembly is then clamped securely with four insulated brass studs so that it becomes a secure "sandwich." The shunt is mechanically very sound, and in the present work it supports the entire electrode structure which is immersed

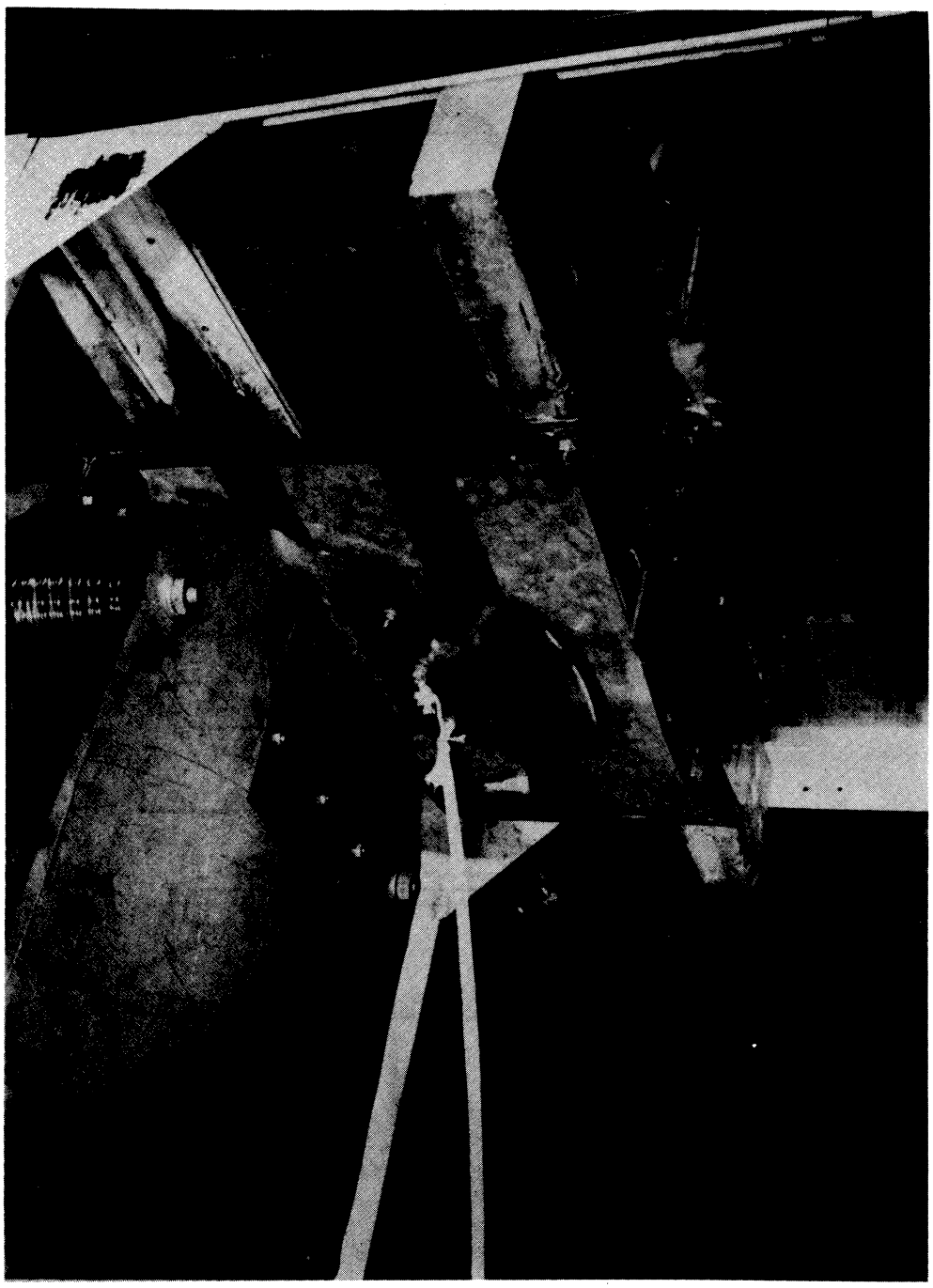

FIG. 5 CURRENT SHUNT

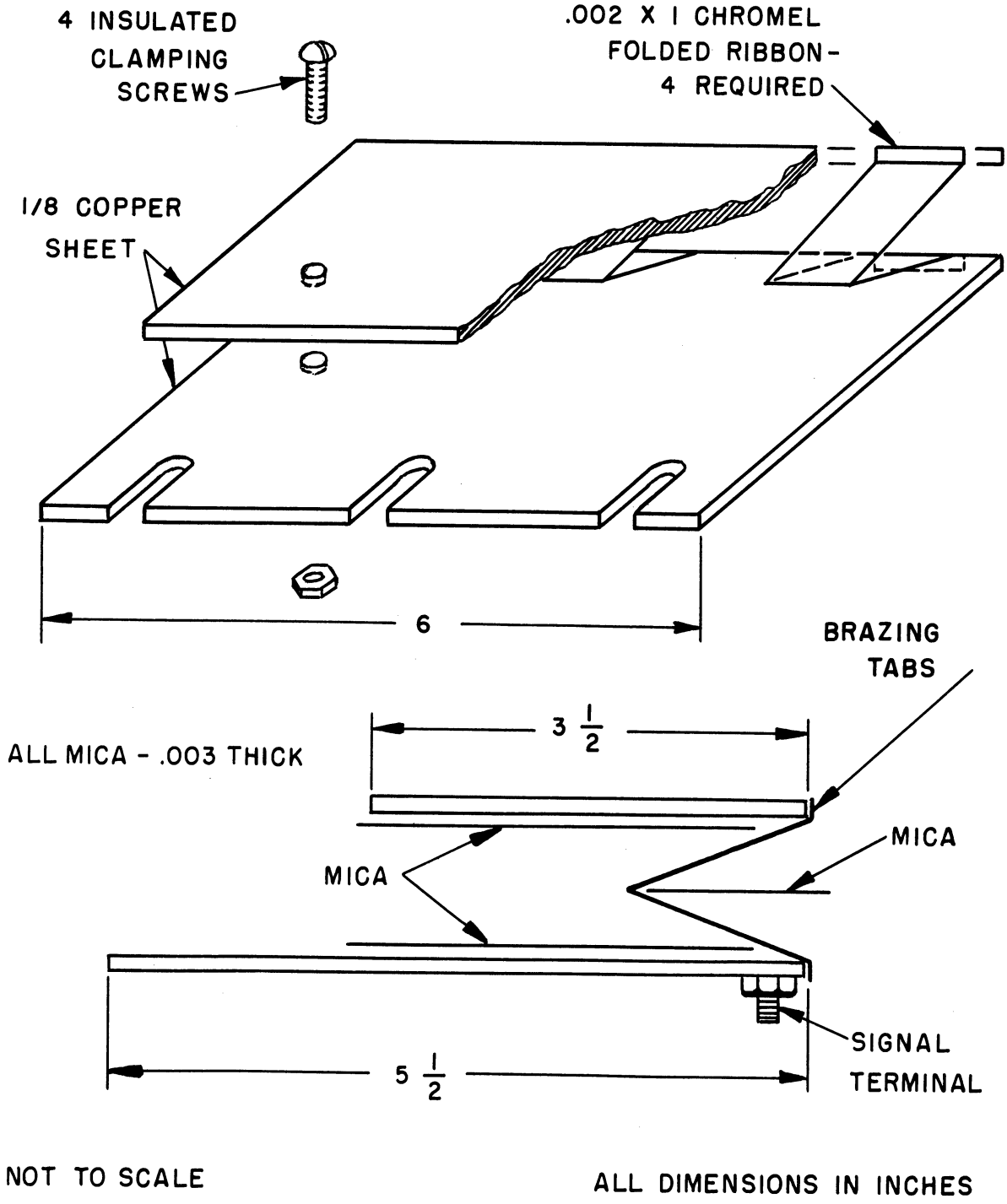

FIG. 6 CONSTRUCTION OF CURRENT SHUNT

in the water.

The shunt which was used to take the current oscillograms on which the calculations in this paper are based contains four Chromel ribbons, each one inch wide, two mils thick, and 1-1/4 inches long (not including the brazing tabs). The mica insulating sheets are three mils thick, and the outer copper plates are 1/8 inch thick. The resistance of this shunt, measured on a Kelvin double bridge, is 0.00693 ohm. This is a DC measurement and does not take into account skin and proximity effects; however, the skin depth for 137-kilocycle current in Chromel is about 50 mils, and thus the current distribution over the 2-mil ribbon is essentially constant. As a check, the resistance of the shunt was calculated using the manufacturer's data for resistivity of Chromel and the result was 0.00664 ohm. This is a difference of 4.2 percent which is sufficiently close agreement to confirm the measured value. The self-inductance of the shunt is below that which can be conveniently measured by conventional laboratory methods; a very refined and sensitive method would have to be developed. A calculation of the inductance based on the dimensions of the shunt gives a value of 2.5×10^{-11} henrys. The maximum rate of change of current obtained with the present discharge circuit, about 6×10^{10} amperes per second, would cause an induced voltage of about 1.5 volts across the shunt. This may be compared with the signal, or resistive, voltage developed across the shunt at current maximum of about 590 volts. Thus the current shunt is probably not being used to the limit of its capabilities in the present application. Even if the actual shunt inductance were ten times the calculated value, the shunt performance would be adequate to the accuracy with which the current oscillograms can be measured.

The temperature stability of the current shunt is of no concern to the present investigation since the duty cycle is extremely small. After a discharge lasting approximately 25 microseconds, there is a long period while the electrodes are removed from the tank, cameras reset, and a new setup made. The calibration of the shunt has been observed to drift gradually with time over a period of months. Usually the drift consists of an increase in resistance, but the amount of change is very small. Calibration of the shunt by means of the Kelvin bridge at intervals of several months compensates adequately for this drift. More frequent use of the shunt, or a higher duty cycle, would make more frequent calibration advisable.

Equivalent Circuit for the Discharge Circuit

For the purpose of carrying out an energy balance for the underwater spark, to be discussed later in this dissertation, it will be necessary to know the spark power input as a function of time. This spark power input will be obtained by use of an equivalent circuit for the actual discharge circuit. Knowledge of the equivalent-circuit constants and the spark current will supply the information necessary for determining the spark power.

The discharge circuit may be represented by the equivalent circuit shown in Fig. 7. In this equivalent circuit R_1 and L_1 represent the effective series resistance and self-inductance of the part of the actual discharge circuit which is on the storage-capacitor side of the manual air gap. R_2 and L_2 represent similar values for the part of the circuit from the air gap to and including the underwater spark electrodes. This equivalent circuit is approximate in that the actual circuit properties are not lumped, but are distributed along the lead straps. Also

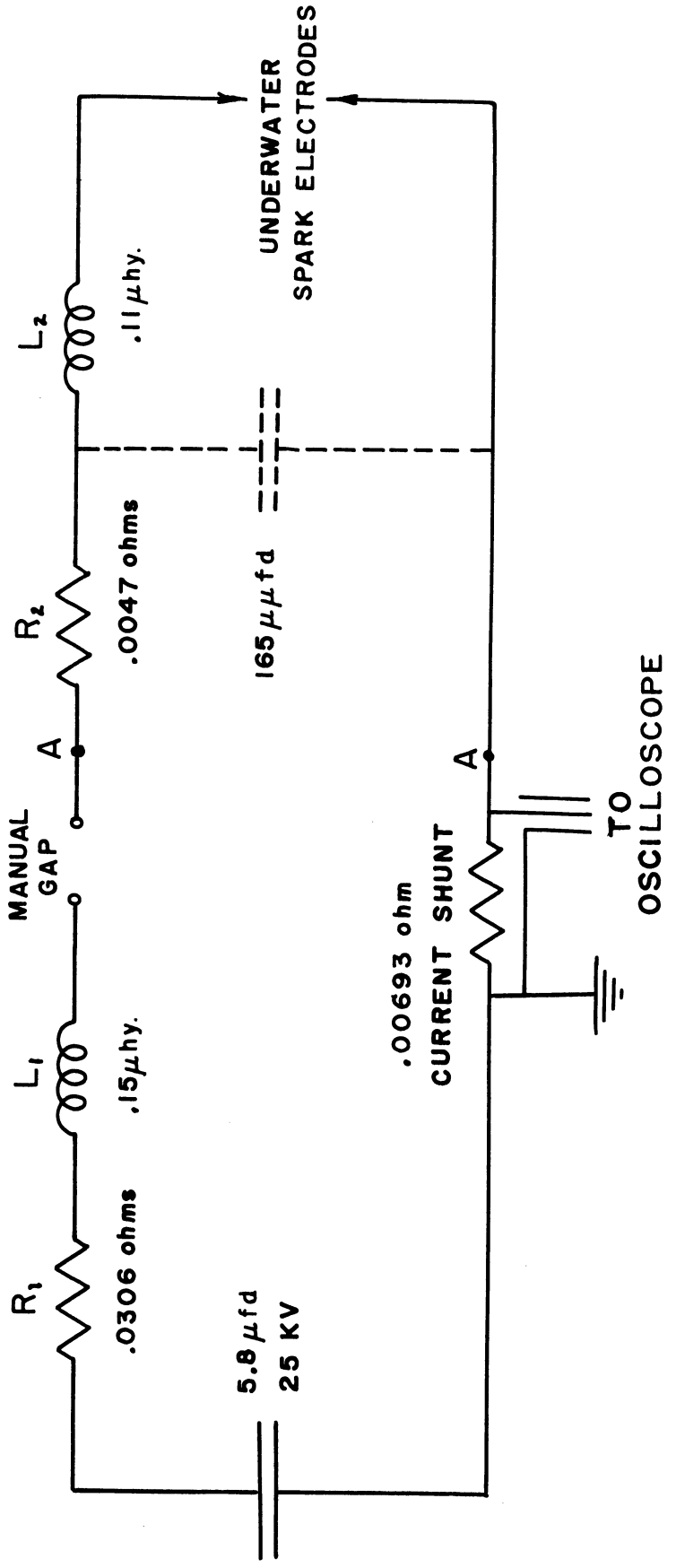

FIG. 7 EQUIVALENT CIRCUIT OF DISCHARGE CIRCUIT

various stray capacitances are neglected, as well as the mutual inductances between the two parts of the circuit on each side of the manual air gap. To the degree of accuracy sought in this analysis, these effects are all negligibly small.

The values of the equivalent-circuit parameters were determined in the following manner: The capacitance of the energy storage capacitors was determined by charging them with a constant current and noting the time rate of change of voltage. As a check, the capacitance was measured using a General Radio impedance bridge. The two measurements checked with an error of 1.7 percent; a mean value of the two readings was taken to be the measured value. Next, the value of $(L_1 + L_2)$ was determined by taking an oscillogram of the discharge current when the circuit was used in its normal way, i.e., with 25 kilovolts on the storage capacitor and a one-mil tungsten initiating wire 1.5 centimeters long between the underwater electrodes. Under this condition the current reaches a peak of 85,000 amperes, has a resonant frequency of about 130 kilocycles, and persists for approximately four cycles. From the period of the damped current oscillation, the total effective series inductance was found to be 0.26 microhenry. The correction to be made to this value in order to allow for the effect of damping upon the oscillation period amounted to only 2 percent, which is negligible in view of the limited accuracy with which the oscillogram can be measured.

The damping of the current is more nearly exponential than the approximate straight-line relationship which is often encountered in spark discharges. Straight-line current damping indicates an effective series resistance which increases as current decreases. This situation may exist in the present case during the initial expansion stage of the

spark channel, but the resolution of the oscillograms is not sufficient to make a definite determination. All that can be said is that during the latter stages of the spark history, the damping is caused by an approximately constant resistance. From the amount of damping, the effective average total series resistance was found to be 0.0690 ohm. This includes R_1, R_2, the current shunt, the spark resistance, the coupled cabinet resistance, the resistance of the air spark across the manual gap, and any modification of these caused by proximity and skin effects.

The effective series resistance and inductance of the discharge circuit on the capacitor side of the manual air gap switch, R_1 and L_1, were determined in a similar manner. A copper strap about six inches wide and two inches long was clamped so it shorted the discharge circuit across the points corresponding to A-A on the equivalent circuit. The capacitor was then charged to approximately 10 kilovolts, this lower value being chosen to limit the current to a typical value. The current oscillogram was taken and the appropriate values calculated from the period and damping factor as before. The value of R_1, 0.0306 ohm, includes the lead resistance, equivalent resistance of the air arc across the manual gap, and coupled cabinet resistance. The modification of resistance caused by skin effect is only approximately taken into account since the new frequency was 170 kilocycles, of the same order as the original 130 kilocycles. The value L_1 was found to be 0.15 microhenry. Next the short circuit across A-A was removed, and a copper wire was used to short circuit the underwater spark electrodes. This was done in such a manner that no additional contact resistance was introduced into the circuit. The circuit was again discharged, with the storage-capacitor

voltage being chosen so that the peak current would again be about 85,000 amperes. The damped sine wave indicated a series inductance of 0.26 microhenry, and an effective series resistance of 0.0422 ohm. From these three sets of data, the values of the parameters of the equivalent discharge circuit may be assigned. The data indicate that the spark has an average effective resistance of about 0.027 ohm during the later stages of the current oscillations.

The removable electrode leads which go down into the water tank are large in area and closely spaced, the insulation being provided by a non-porous rubber sheet. The interlead capacitance was determined in order to confirm that it did not seriously affect the results of the circuit analysis. It was measured and found to be 165 micromicrofarads, which is negligible.

All measured values of the equivalent-circuit parameters were checked by calculation. The geometry and dimensions of the actual discharge circuit were taken, and the approximation of lumped parameters was used. All calculations checked the measured values within 30 percent or better. The larger discrepancies were primarily the result of neglecting the resistance and inductance coupled into the discharge circuit as a consequence of currents induced in the shielding cage. These calculations served their purpose in establishing that the measured circuit constants were not in error by a factor approaching an order of magnitude. It will be noted that the power loss in the manual air gap arc is taken into account in the resistor R_1. However, this arc has an unrestricted cross section and a falling voltage characteristic, so that the voltage across it is probably small compared to other voltages around the discharge circuit. The fact that power dissipated by this arc has not

been neglected will become evident when the underwater spark power input is computed later. Further, since breakdown of an atmospheric gap occurs in times of the order of 10^{-8} second, for the purposes of this study the closure of the discharge circuit may be considered instantaneous.

The Water Tank

The water tank in which the spark took place is 12 by 15 by 20 inches. It is welded from 3/32-inch sheet steel and is painted with a commercial rust-preventing paint. Splash covers are used, since the water is rather violently disturbed when the discharge takes place. The 3-inch diameter window is 5/16-inch-thick plexiglas, clamped between sheet rubber gaskets. It was found that glass was too fragile for this application, since the underwater spark is only 4-3/4 inches from the window surface. Evidently the inherent flexibility of the plexiglas (a plastic), together with the flexibility of the mounting gaskets, is the reason for the success of this window. Optical distortion caused by pressure deflection of the window is of no concern since approximately 75 microseconds are required for the shock front to reach the window. The spark electrodes are located about 7 inches below the free surface of the water. All work was carried out in Ann Arbor city water. The water was constantly undergoing change by continuous flow, and the temperature was not artificially altered. The temperatures showed a seasonal variation over the range from 9 degrees centigrade to 22 degrees centigrade.

CHAPTER III

KERR CELL PHOTOGRAPHY AND THE DETERMINATION OF SPARK CHANNEL SIZE

The initial impressions of the nature of the underwater spark were obtained by means of photographs. In fact, photography has formed the backbone of the present method of investigation. It provided the spark size as a function of time, which was used in the calculation of channel pressures, and played an important part in the temperature and energy balance calculations. In addition to this quantitative type of data, many conclusions have been reached concerning underwater-spark phenomena from the qualitative information contained in the photographs. This chapter is a discussion of the photographic equipment and of the conclusions which have been drawn from this qualitative information, as well as a presentation of the growth curve of the underwater spark as a function of time.

Photographing Rapid Events

In the first exploratory stages of the investigation, pictures of the underwater spark were taken by use of a conventional camera. The spark voltage was of the order of 6 kilovolts, and the exposure was made by holding the camera shutter open during the entire course of the discharge. These photographs lacked suitable resolution for a detailed study of the spark channel. They were blurred, and one could not establish the time sequence of the various images on the final picture or the rapidity with which phenomena took place. For these reasons a photographic system having a time resolution of the order of one micro-

second was considered necessary.

When photographing rapid events, the length of the exposure time may be determined either by using a source of illumination of known or controllable duration, or by use of a shutter which forms an integral part of the camera. If the event is a self-luminous one so that it supplies the light necessary to expose the film, then only the second method is suitable. Conventional blade-type and focal-plane camera shutters can only be made to give reliable operation at speeds not appreciably higher than that corresponding to exposures of one millisecond. Suitable rotary methods, such as rotating mirrors or slits, may be used to get exposures in the one-to-ten microsecond range. For single exposures of one microsecond or less, it is desirable to use one of the various electrical shutters. These shutters have no moving parts, and hence are not limited in their speed of operation by problems of mechanical design of fast-moving components.

There are a number of optical effects which may be utilized to construct an electrical shutter (18, Chap. 19). One class of phenomena is referred to as magneto-optics, which is concerned with the origination or transmission of light through matter in a magnetic field. The Faraday effect is the magneto-optical effect most used for building electrical shutters. Water and glass are usually employed as the optically active materials in which magneto-rotation takes place. Thus the light beam to be controlled is passed through a polarizer, then through a glass block or water cell located in a coil which provides a longitudinal magnetic field, and finally through a second polarizer. However, a magneto-rotary shutter of this type was not chosen for the present application since it requires a short-duration pulse of current through

the magnetizing coil. A pulser to supply a very short current pulse is not as simple and reliable as a pulser built to supply a short-duration voltage pulse.

The second general class of optical effects is referred to as electro-optics. The Kerr electro-optical effect is utilized in the construction of a Kerr cell. Certain liquids become birefringent when placed in an electrical field. Nitrobenzene shows this effect very strongly and hence is usually used in Kerr cells. The liquid behaves like a doubly refracting crystal with its optic axis in the direction of the electric field. The light beam to be controlled is first plane polarized with the plane of polarization selected to be at an angle of 45° with respect to the direction of the applied electric field. The two equal mutually perpendicular components of the incident light, one taken in the direction of the electric field and one at right angles to it, travel at different velocities through the birefringent liquid. Thus the polarization of the beam gradually shifts from plane polarization to circular polarization and back to plane polarization. The second polarizer, which is crossed with respect to the first when there is no applied electric field, is thus able to transmit a component of the beam when the electric field is applied to the liquid.

In spite of its various disadvantages, nitrobenzene is the most generally suitable liquid for use in Kerr cells because of its exceptionally large Kerr constant. The disadvantages of nitrobenzene are that it is quite opaque to light having a wavelength less than 4000 Angstroms, it is volatile and poisonous, it is a good solvent of materials which one would wish to use to seal the junctions of the Kerr cell container, it is inflammable, and the high dielectric constant, 36, requires that the pulser deliver sufficient power to charge the resulting increased elec-

trode capacity very rapidly. The upper limit to the speed of operation of a Kerr cell is set by the molecular relaxation time of nitrobenzene, which, similarly to other polar liquids, is of the order of 10^{-9} seconds. Finally, nitrobenzene tends to absorb contamination, namely moisture, from the atmosphere and thereby increase its electrical conductivity.

The Kerr Cell Camera

A photograph of the Kerr cell used in this study appears in Fig. 8. The glass cell containing the electrodes and the nitrobenzene has two optically plane windows. These windows are held against ground bosses on the cell body by aluminum rings having a shoulder which bears on the plane glass sheets only along a line opposite to the plane supporting surfaces on the cell body. Thus the clamping force does not distort the plane glass windows. Further, by leaving the cell open to the atmosphere, temperature changes cannot cause internal pressure changes and thus distort the windows. The polarizers consist of two one-inch diameter discs of type HN 22 high-extinction polaroid mounted in glass of optical quality. The forward polaroid (on the camera lens side) has no provision for adjustment, but it is mounted on a removable slide so that the Kerr cell may be rendered transparent in order to focus the camera or to do other setup work which may become necessary. The second polaroid (on the film side) is adjustable about the two axes in a plane perpendicular to the light beam for the purpose of attaining parallelism with the other optical surfaces of the cell, and it may be rotated about an axis coincident with the light beam for the purpose of adjusting for maximum extinction when there is no applied electric field. The parallelism of all the optical surfaces of the Kerr cell is important in order to eliminate multiple images on the film due to reflections from the surfaces.

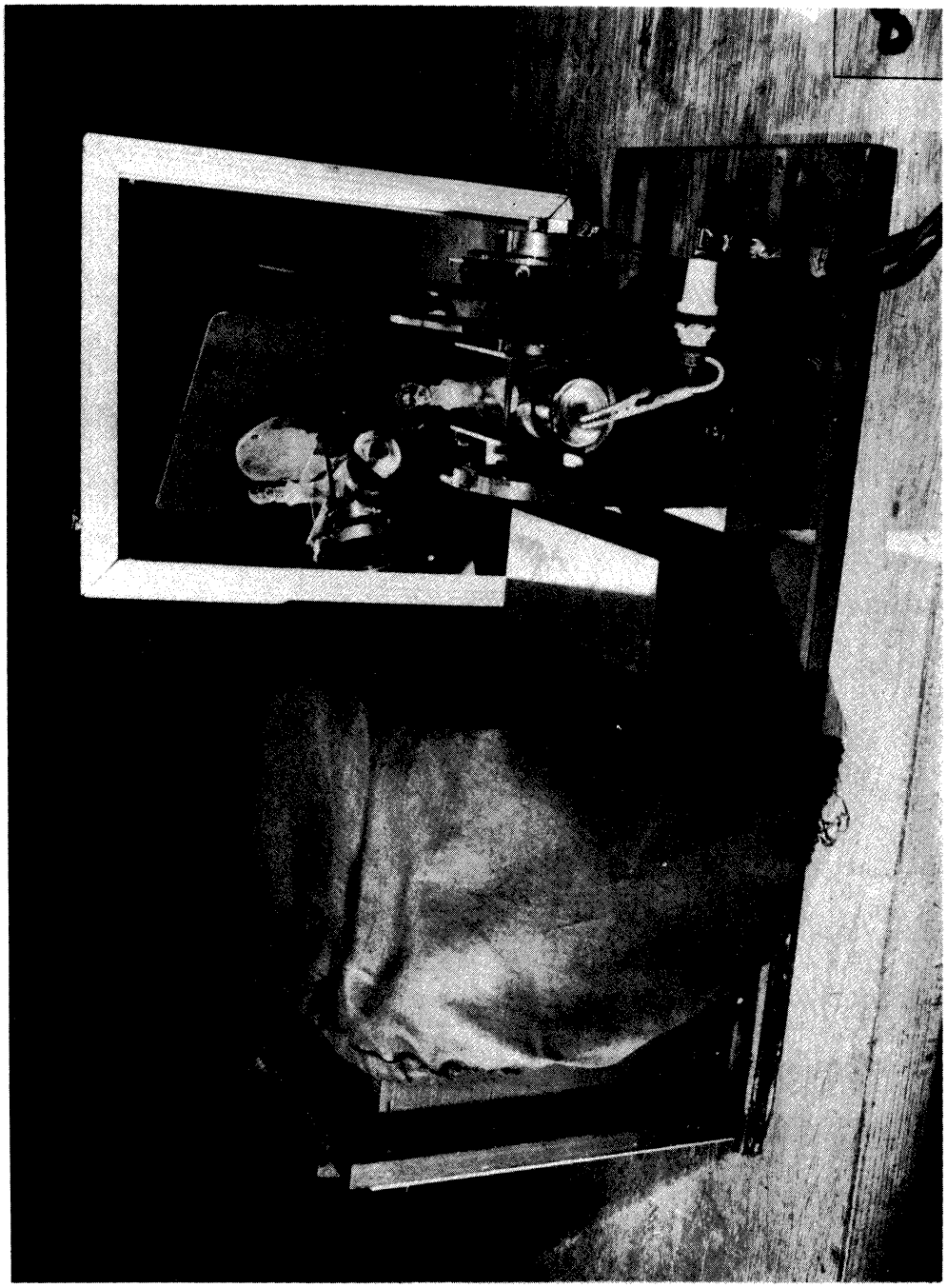

FIG. 8 KERR CELL CAMERA

In practice, the Kerr cell must be realigned whenever there is a possibility that the parallelism has been disturbed. This alignment is carried out by observing the image of a six-volt lamp filament operated well above rated voltage on the camera ground glass.

When the Kerr cell was first constructed, it was found that specular reflection at grazing angles from the electrodes caused extraneous "ghost" images. These were eliminated by roughening the electrode surfaces with emery paper and applying a thin coating of aquadag. Two metal foil apertures having 6.5-millimeter by 10-millimeter rectangular openings are placed over the plane windows on each side of the Kerr cell. These restrict the light passing through the Kerr cell to those rays which have passed between the cell electrodes. The electrodes are each 12 millimeters by 25 millimeters in area, and are spaced 4.5 millimeters apart. When the Kerr cell is completely adjusted, the light-to-dark ratio is sufficiently high so that no perceptible darkening occurs on the photographic film when the underwater spark discharge takes place with the camera properly focussed on the spark, but with no voltage pulse applied to the Kerr cell electrodes. The adverse effects produced by impurities in the nitrobenzene have not been detrimental to the operation of the Kerr cell camera in this investigation. Apparently a voltage pulse lasting only one-quarter microsecond is short enough so that there is negligible accumulation of field-distorting space charge throughout the volume due to nonuniform electrical conductivity. Thus the electric field remains sufficiently uniform throughout the region between the electrodes, yielding a high light-to-dark ratio.

A dimensional sketch of the optical system of the Kerr cell camera is shown in Fig. 9. The lens is a Kodak f.4.5 Ektar having a focal length of 6 inches. The 4-inch by 5-inch film is held in cut film holders which

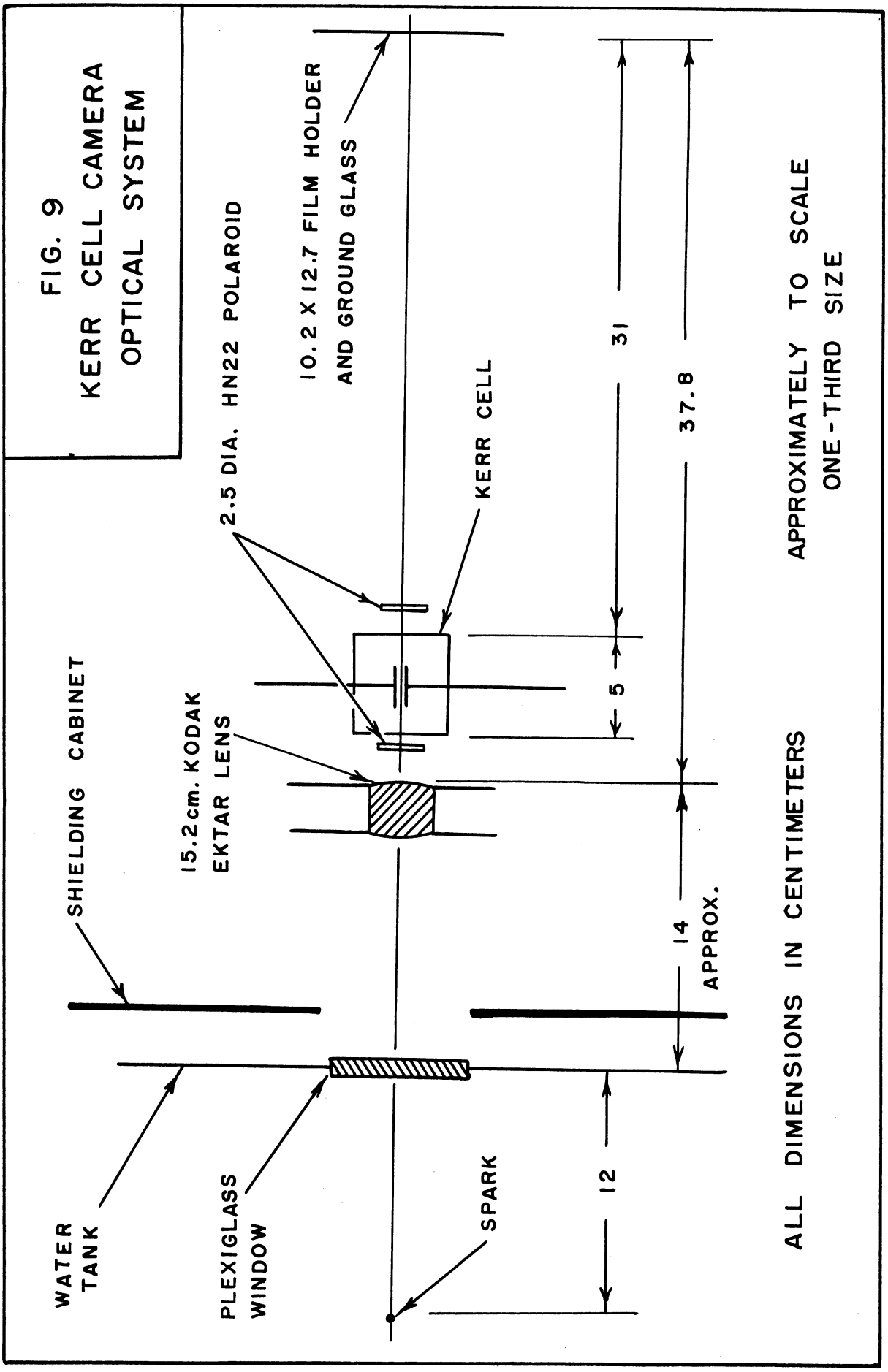
FIG. 9
KERR CELL CAMERA
OPTICAL SYSTEM
WATER TANK
PLEXIGLASS WINDOW
SHIELDING CABINET
15.2cm. KODAK EKTAR LENS
2.5 DIA. HN22 POLAROID
10.2 X 12.7 FILM HOLDER AND GROUND GLASS
KERR CELL
SPARK
12
14 APPROX.
5
31
37.8
ALL DIMENSIONS IN CENTIMETERS
APPROXIMATELY TO SCALE
ONE-THIRD SIZE

in turn mount in a conventional ground-glass camera back. The analysis of the optical system is straightforward. If the iris diaphragm of the lens is set at about f.8 or larger, then the edges of the Kerr cell electrodes toward the film form the aperture stop of the optical system for the object distance at which the underwater spark is located. Under this condition, the forward, or front, edges of the electrodes form the field stop. The photographic speed of the entire optical system used in this way is approximately f.42. If, however, the iris diaphragm of the camera lens is successively stopped down, then it becomes the field stop and finally the aperture stop for the optical system. These two situations are not analyzed since the camera was not used in this way while photographing the underwater spark.

Kerr Cell Pulser

The Kerr cell requires a 7-kilovolt pulse of approximately rectangular form and having a duration equal to the desired photographic exposure time. The Tektronix 513D oscilloscope provides a trigger pulse of approximately 50 volts peak value, and the amount of delay is continuously adjustable. Therefore the Kerr cell pulser was designed to utilize this delay trigger signal. The pulser circuit used is diagramed in Fig. 10, and a photograph is shown in Fig. 11. A Guillemin type-A voltage-fed pulse network is charged to approximately 14 kilovolts. This network is then discharged through its characteristic impedance, the switching being performed by a 5C22 hydrogen thyratron. The voltage pulse developed across the load resistor is conducted to the Kerr cell electrodes by a pair of twisted leads which are arranged to be as short as possible. In order to obtain a control grid signal sufficiently large to trigger the 5C22 thyratron reliably (200 volts is recommended by the manufacturer), a 2D21 thyratron

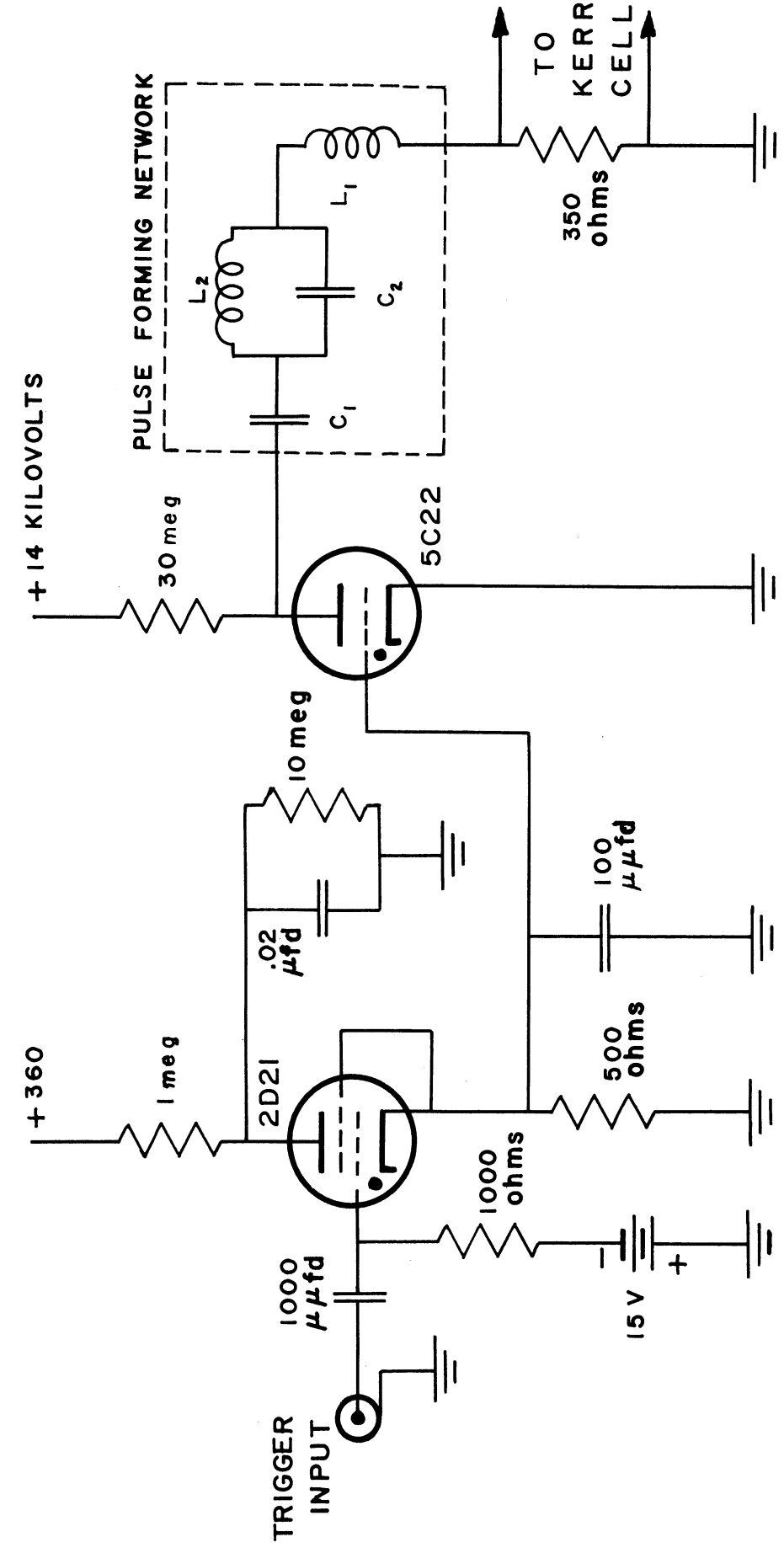

FIG. 10

KERR CELL PULSER CIRCUIT

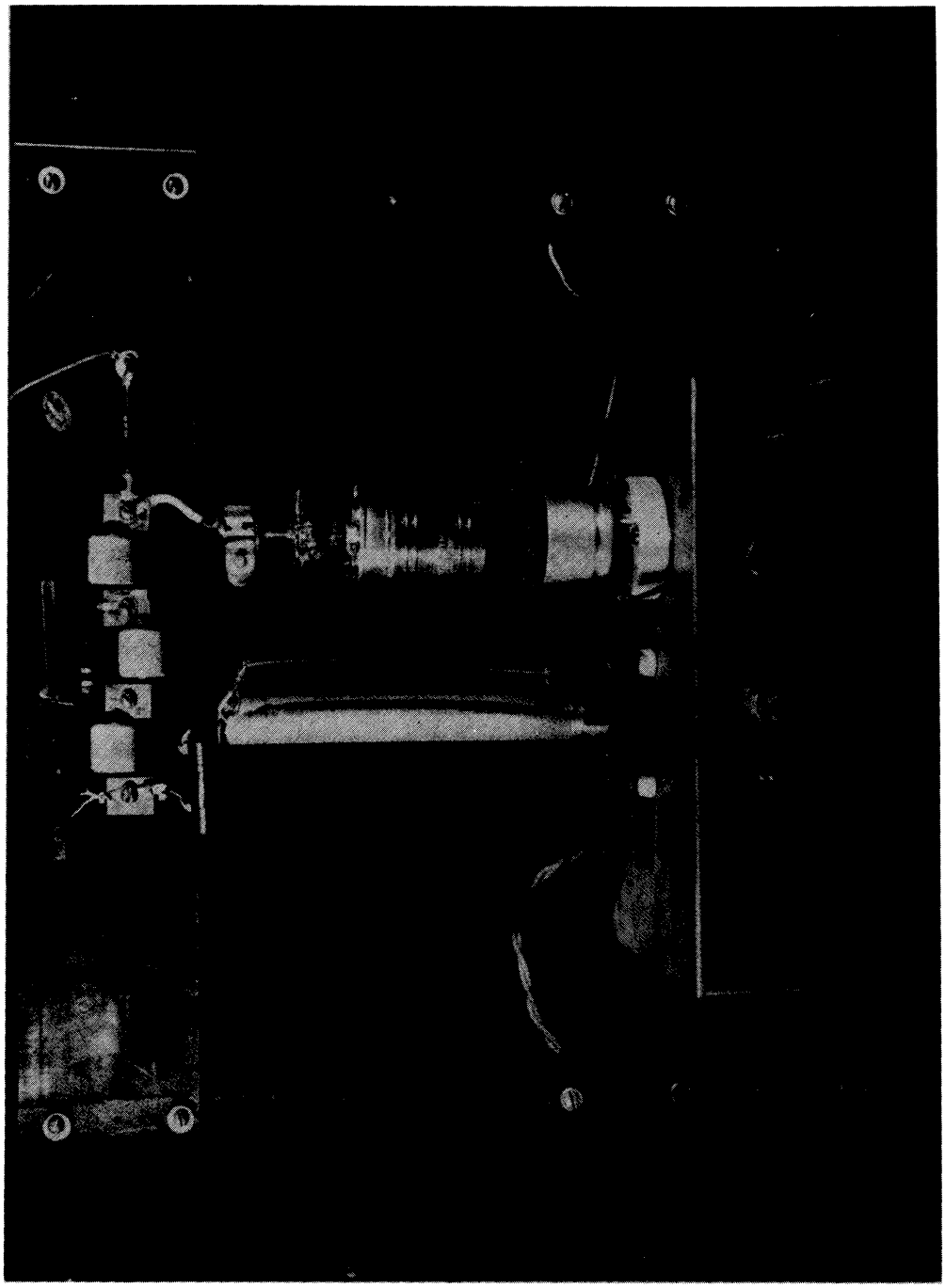

FIG. 11 KERR CELL PULSER

is triggered from the oscilloscope delay trigger signal, and the resulting output is used for triggering the 5C22. The total time delay through this circuit is approximately 0.4 microsecond.

In the initial stages of this investigation, a General Electric one-microsecond radar pulse network was utilized as the pulse-forming network. However, when the underwater spark discharge circuit was subsequently redesigned so that greater power was fed into the spark, the resulting Kerr cell photographs were found to be overexposed. Since improving the time resolution of the photographs was important, it was decided that a shorter exposure time would be a more desirable solution to the overexposure problem than attenuating the light by absorbers, or by decreasing the camera aperture or film speed. The pulse network which was built is a two-section network, design formulas being taken from the literature (19, p. 203). The network develops a 7-kilovolt pulse across a 350-ohm Globar resistor, the duration being approximately one-quarter microsecond. The voltage pulse shape is shown in Fig. 12. The pulse could be shaped more ideally by the addition of more sections to the pulse-forming network, but the present requirements are amply met with the two-section network. The open construction of the pulser circuit causes the oscilloscope to pick up a small interference signal which appears as a one-quarter microsecond gap in the oscilloscope trace. This has served a useful purpose in that the desired delay time may be set before a Kerr cell photograph is taken, and after the oscilloscope current trace has been developed, the location of the small gap identifies the instant at which the picture was taken.

Most of the photographs taken with the Kerr cell camera were on Kodak Super Panchro Press Type B film. This panchromatic film has an optimum ratio of speed to graininess which has been suitable for the

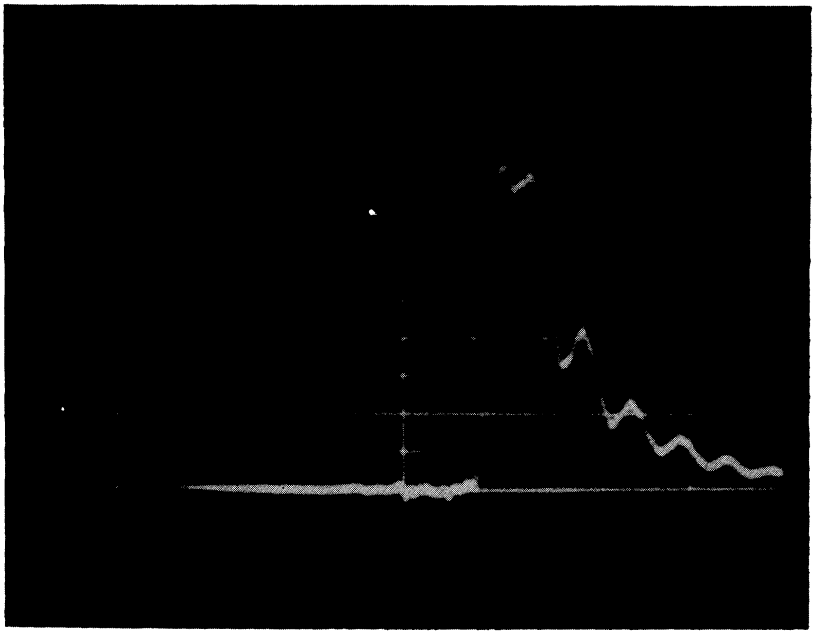

FIG. 12 OSCILLOGRAM OF PULSER OUTPUT

SCALE FACTORS:

VERTICAL— 2000 VOLTS PER DIV.

HORIZONTAL— 0.2 MICROSEC. PER DIV.

PULSE-FORMING NETWORK CONSTANTS:

(SEE FIG. 10)

C_1— 440 MICROMICROFARADS

C_2— 263 MICROMICROFARADS

L_1— 11.1 MICROHENRYS

L_2— 2.99 MICROHENRYS

present work. Development was carried out in Panthermic 777 to a gamma of one as recommended by the developer manufacturer. The final prints which were studied were on 8 by 10 glossy paper, the spark image being approximately 8 or 9 times natural size. With this degree of enlargement, the grain was not at all noticeable, in fact the amount of enlargement could be further increased if it were desirable. In some of the photographs where optimum photographic speed was required, so that a nonluminous object in the spark vicinity would be visible, Kodak Royal Pan film was used. Development was in Kodak SD-19A. This is a combination of a highly active developer and a chemical fogging agent. Use of this exceptionally fast emulsion and active developer requires very carefully controlled darkroom processing, or else the grain size will be objectionably large, resulting in loss of definition. It should of course be realized that a large amount of emulsion sensitivity is lost due to failure of the film exposure reciprocity law in cases where the exposure times are as short as one microsecond or less.

All photographs taken of sparks should be recognized as distortions of the actual appearance of the spark as it would look if it were viewed directly by the human eye. In general, the spectral response of photographic emulsions is much different from that of the eye, so that blue radiation is overemphasized, and the invisible ultraviolet radiation is probably the dominant contributor to film exposure. In the present study, this distortion factor is practically eliminated (unintentionally) by the very low transmission of nitrobenzene at wavelengths less than 4000 Angstroms. A second factor introducing distortion in all spark photographs is the limited latitude of the film emulsion. For modern fast films, the latitude is of the order of 100, so that the film can encompass a brightness ratio of only 100 on the object photographed. Printing on photo-

graphic paper further distorts the image tones, since paper has even less latitude. Thus it should be remembered, when viewing the spark photographs, that a region which appears dark on the photograph may actually be quite luminous; it appears dark only by comparison with the adjacent brighter areas.

In the present study, no attempt has been made to use photographic emulsions as a tool for photometric measurements. The dependence of the amount of emulsion darkening on such factors as spectral character of the source, exact condition of the photographic developer, development time and temperature, age and previous storage conditions of the film, film batch number, and the deviations from reciprocity, would make such a photometric measurement completely unreliable. It would be very complicated to standardize every sheet of film used in such a measurement, as is presently done in spectroscopic work.

Spherical Structures

The first Kerr cell photographs were taken of underwater sparks which were produced by discharging an 11-microfarad capacitor charged to 4 to 10 kilovolts. The resulting currents were approximately critically damped and reached maxima of about 10,000 to 15,000 amperes in about 8 microseconds after establishment of the gaseous conducting channel. Figs. 13 and 14 are typical photographs taken with an exposure time of one microsecond. The spherical structures which form on the two electrodes have not been previously reported in the literature. Although the detailed study of these spheres is not within the realm of extremely high pressure gaseous conduction, a short discussion of their characteristics will be included because of their novelty. They present essentially a problem in the molecular structure of a highly polar liquid.

(21). In this same manner secondary unduloids have been produced, and tertiary unduloids are considered possible. The fact that unduloids are created in almost all work with exploding wires may be realized by reference to works in which pictures are presented of the early stages of exploded wire discharges (7, 22). A striated pattern is almost always evident.

The pinch force will not cause a liquid current-carrying wire to constrict unless there is a small initial constriction; a perfectly uniform cylindrical wire would be in unstable equilibrium. This fact, by itself, suggests that the unduloid droplets would be randomly spaced, and correspondingly random in size. This would not give the consistently uniform and reproducible striation spacing which is observed in the various melting-wire studies. There is a mechanism which is probably effective in determining the striation spacing. In 1878, Rayleigh presented a theoretical investigation of the stability of a liquid cylinder issuing from a nozzle (23). One part of this work is concerned with instability caused by surface tension of the liquid. The parts of Rayleigh's work which apply to the present case can be summarized in terms of two equations. The spacing of the droplets which form as a consequence of the instability of the cylinder is given by the equation,

$$\lambda = 4.508 \times 2a \tag{3.1}$$

where

a is the initial radius of the liquid cylinder, and

λ is the droplet spacing.

The rate at which the droplets form is expressed as an exponential time-constant of growth, β; thus

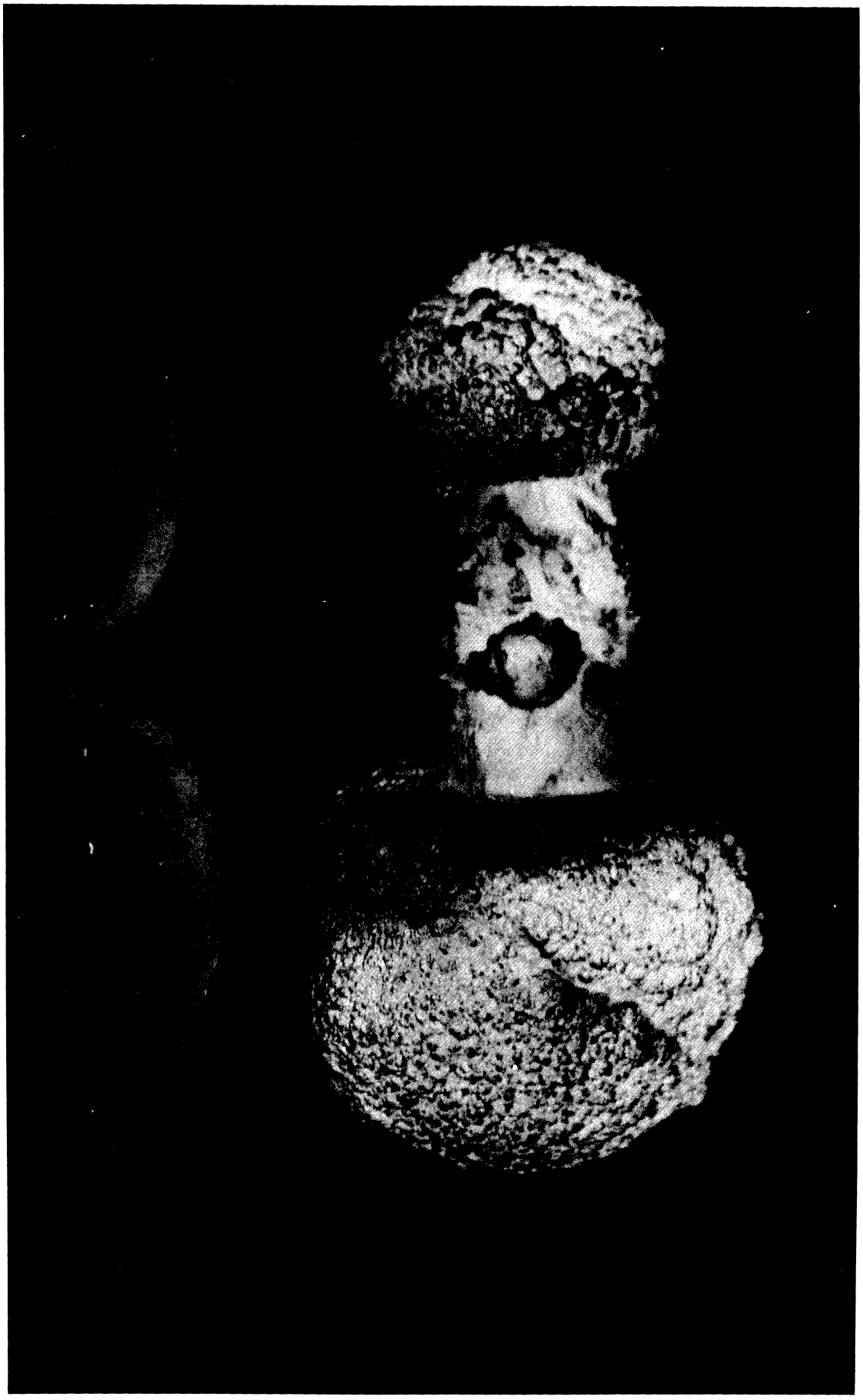

FIG. 14 SIX - KILOVOLT SPARK AT 10 MICROSECONDS

The spheres originate and grow during the prebreakdown, or formative, period of the underwater spark. As soon as electrical breakdown is complete, their growth is arrested or considerably retarded. During the period of their growth, a current of the order of one ampere flows. Any alteration of the breakdown conditions which tends to extend the formative period causes larger spheres to be formed. One such variable is water temperature. When the temperature is about 10 degrees centigrade, the formative period may last several milliseconds, and the spheres grow very large. At 15 degrees centigrade the formative period is short, and the spheres are small. No pronounced spherical structure has been observed for temperatures above 15 degrees centigrade. The formative period may also be extended by inserting a solid dielectric barrier between the electrodes, as was done in Fig. 15. In this case the spheres are large, and it appears that they are reluctant to contact a solid object in their vicinity. A third method of extending the formative period is to charge the capacitors to a reduced voltage. The formative period then becomes increasingly longer in a manner quite similar to that encountered in the electrical breakdown of a gas. At the lower voltages the formative time becomes so long that the capacitors are discharged before the breakdown process is completed. This occurs at capacitor voltages of the order of 5 kilovolts, depending on water temperature and the amount of capacity.

In Figs. 13 to 16 the left electrode is positive. The sphere on this electrode is always larger, having a surface similar to an orange. The smaller sphere on the right may have a texture varying from a milky to a glassy appearance. The spheres appear to be nonluminous; the light from them probably originates from the spark channel within their volume. The spheres also form when the capacitors are charged to a voltage less

FIG. 15 SEVEN-KILOVOLT SPARK
WITH DIELECTRIC BARRIER

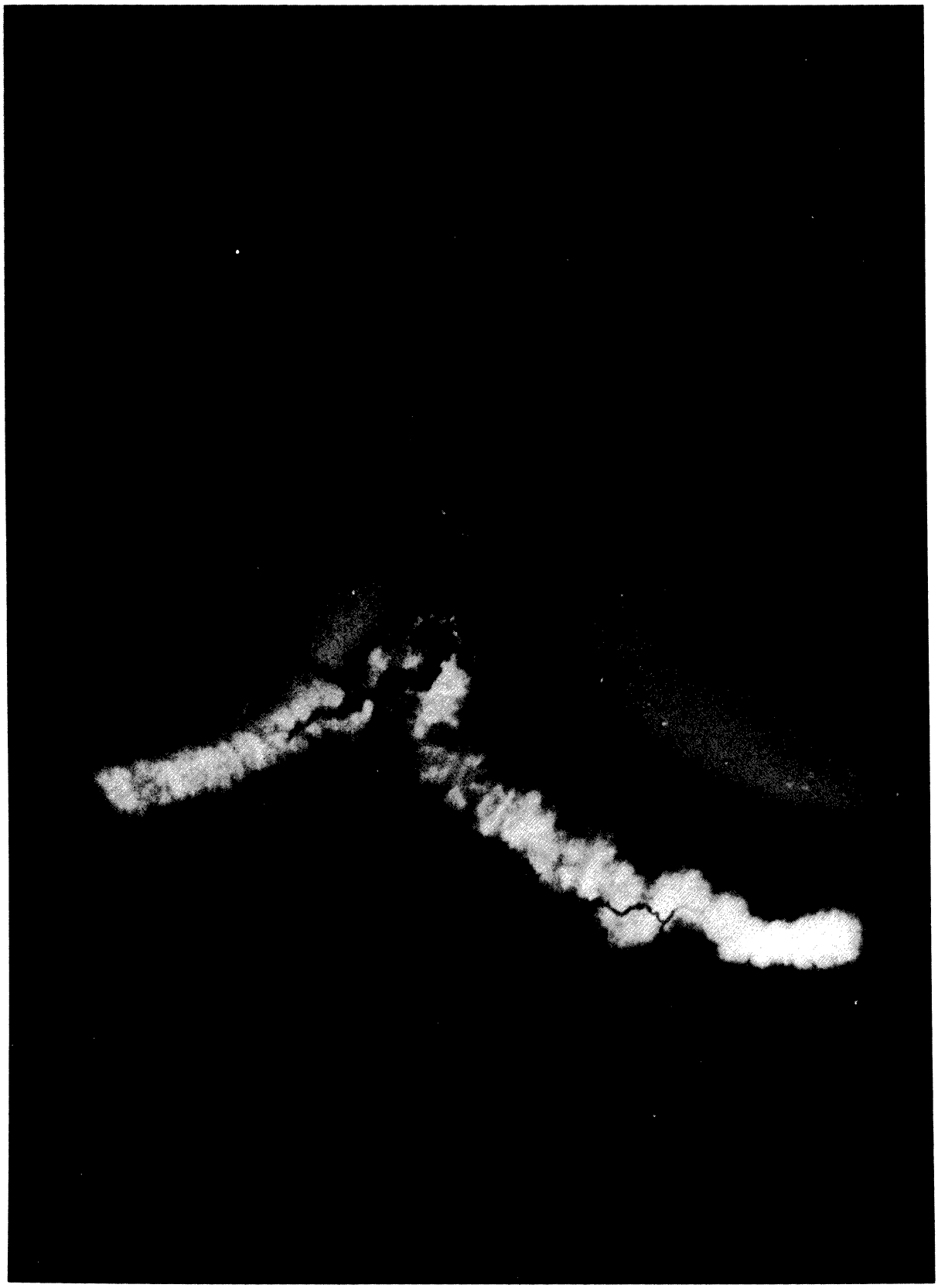

FIG. 16 EIGHTEEN-KILOVOLT SPARK
AT 1 MICROSECOND

than that required for breakdown. This was noted by using an auxiliary flash light source to provide illumination for the photograph. When complete breakdown does not take place, there is no noise generated in the water, indicating that the spheres do not represent an appreciable change in the water density. One of the most interesting characteristics of the spheres is their consistently uniform spherical shape. The electric field between the parallel-wire electrodes is far from being spherically symmetric. One possible explanation of the spheres is that they are regions of spontaneous electric polarization somewhat analogous to the domains in a ferromagnetic material. Light, upon leaving or entering these liquid electric domains, would be refracted at the (irregular) boundary due to an alteration of the index of refraction, thus rendering the boundary visible.

When the capacitor voltage is approximately 10 kilovolts or greater, the formative time of the underwater spark becomes short, of the order of a microsecond. The breakdown proceeds by means of branched streamers which advance from each electrode without formation of the spheres. When the gap is finally bridged, the discharge takes place. This causes the unsuccessful streamers to become dormant, and their presence is revealed by reflected light from the main discharge channel. Fig. 16 is a typical example of streamer formation.

Initiating Wire and Striations

It became evident early in the investigation that obtaining data suitable for quantitative interpretation would be hampered by the random nature of the spark breakdown process. The statistical formative time lag, the presence of the spheres, the irregular unpredictable path of the discharge, and the nonuniform cross section along the length of the channel

all made reproducible sparks impossible. All these undesirable features of the spark were overcome by one procedure. This consisted of starting the spark immediately upon the application of voltage by means of a fine initiating wire. The use of the initiating wire reduced considerably the rate at which data could be taken; but in return, the reproducibility of behavior of successive sparks was very rewarding. Thus data taken on different sparks could be correlated, and the character of the underwater spark could be followed as a function of time. As will be shown later, the presence of the initiating wire affects the characteristics of the discharge only during the initial quarter-microsecond or so; its presence does not appreciably affect the spark during later times which are of interest in this study.

Many of the Kerr cell photographs of underwater sparks initiated by an initiating wire show pronounced striations, especially during the early stages of spark development. Fig. 17 is an example. The appearance of the striations is not appreciably modified by moderate changes in spark voltage or current, or by changes in initiating wire material. The spacing of the striations is however quite dependent on the initiating-wire diameter. It is quite probable that these striations have as their origin the unduloids which are produced by the melting of the initiating wire. Unduloids are the succession of droplets of molten metal which are formed when a wire is rapidly melted by a high-current discharge. They are a consequence of the pinch forces produced by the magnetic field of the current reacting upon the current itself. Photographs of melting fuse wires often show clearly this phenomenon (20). Kleen has produced solid unduloids by sending a pulse of current through a wire; if the current magnitude and duration are properly controlled, the wire will melt, form unduloids, and then solidify into a structure resembling a string of beads

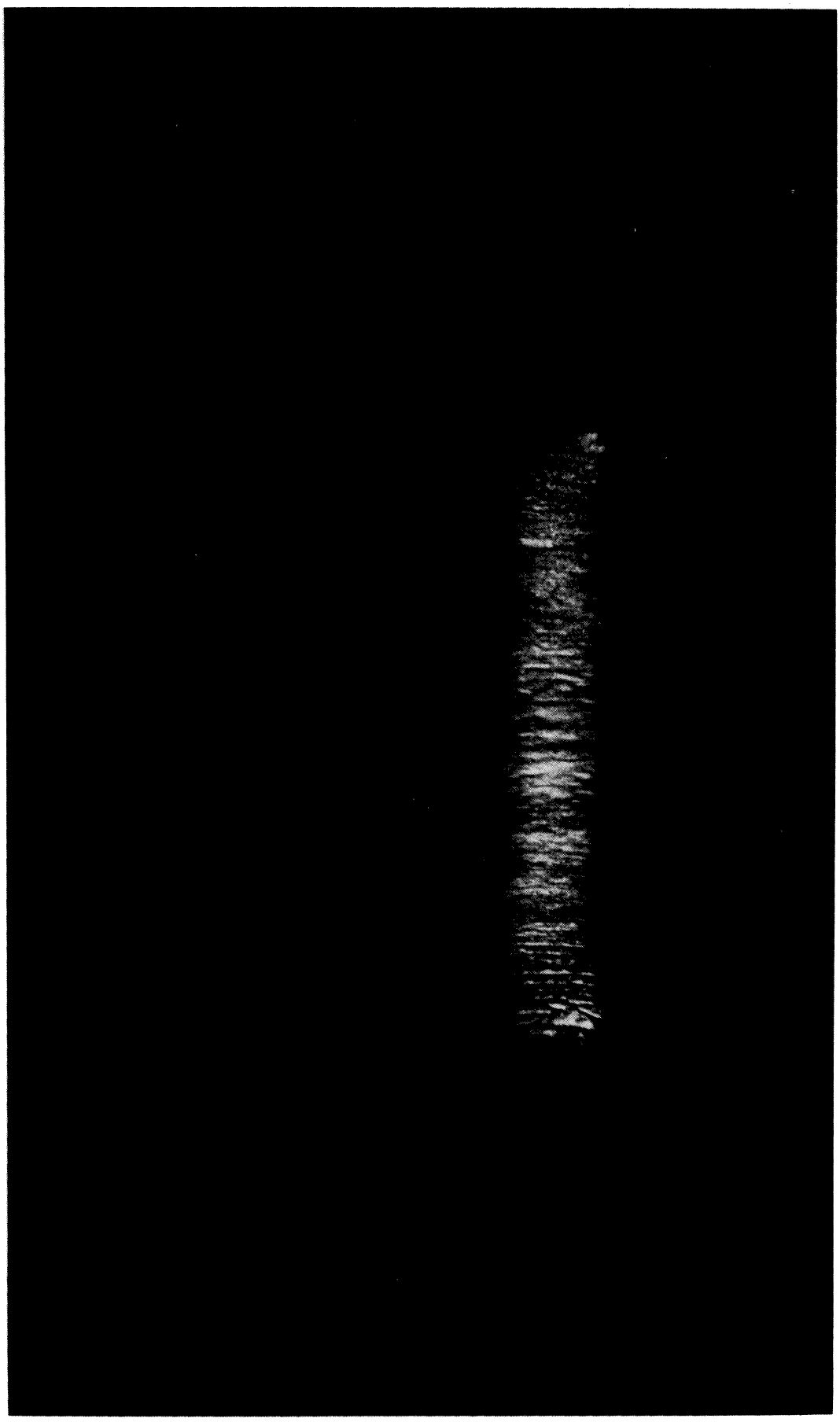

FIG. 17 SIX-KILOVOLT SPARK INITIATED BY THREE-MIL COPPER WIRE

(21). In this same manner secondary unduloids have been produced, and tertiary unduloids are considered possible. The fact that unduloids are created in almost all work with exploding wires may be realized by reference to works in which pictures are presented of the early stages of exploded wire discharges (7, 22). A striated pattern is almost always evident.

The pinch force will not cause a liquid current-carrying wire to constrict unless there is a small initial constriction; a perfectly uniform cylindrical wire would be in unstable equilibrium. This fact, by itself, suggests that the unduloid droplets would be randomly spaced, and correspondingly random in size. This would not give the consistently uniform and reproducible striation spacing which is observed in the various melting-wire studies. There is a mechanism which is probably effective in determining the striation spacing. In 1878, Rayleigh presented a theoretical investigation of the stability of a liquid cylinder issuing from a nozzle (23). One part of this work is concerned with instability caused by surface tension of the liquid. The parts of Rayleigh's work which apply to the present case can be summarized in terms of two equations. The spacing of the droplets which form as a consequence of the instability of the cylinder is given by the equation,

$$\lambda = 4.508 \times 2a \tag{3.1}$$

where

a is the initial radius of the liquid cylinder, and

λ is the droplet spacing.

The rate at which the droplets form is expressed as an exponential time-constant of growth, β; thus

$$\tau = 0.35 \left(\frac{T}{\rho a^3} \right)^{1/2} \qquad (3.2)$$

where

T is the surface tension of the liquid, and

ρ is its density.

The effects of viscosity have been neglected. Equation 3.1 will be discussed first. Kleen has made a large number of measurements of the spacing of unduloids and related them to the original wire size (21). As a typical example he finds experimentally for silver,

$$\frac{\lambda}{2a} = 4.62 \qquad (3.3)$$

He also refers to the work of others who have obtained substantially the same results. The experimental constant in Equation 3.3 has been found to be slightly dependent on wire material and surface condition. In the case of the present study of the wire-initiated underwater spark, striation spacings were measured from Kerr cell photographs for copper and tungsten initiating wires of several sizes. In all cases the measured spacings were exactly (within the error of measurement) one-half or one-fourth the spacing predicted by Equation 3.1. If secondary unduloids were formed, the spacing would be exactly half that given by Equation 3.1; and if tertiary unduloids were formed, the spacing would be one-fourth that given by Equation 3.1. Thus the complete absence of an experimental spacing one-third that in Equation 3.1 is especially significant. It appears, then, that tertiary unduloids may be formed in some cases when the initiating wire melts. Now consider Equation 3.2. If values of surface tension and density which are typical of molten metals are inserted in this equation, the growth time-constant τ is approxima-

tely 100 microseconds for wires of the order of several mils diameter. The forces due to surface tension are thus not large enough to form unduloids in the short times involved in work with exploding wires. The role of the surface tension forces is only to provide the initial, regularly spaced, incremental constrictions which are necessary to allow the magnetic pinch forces to become operative. The pinch forces for a small-diameter wire, carrying a current sufficient to cause rapid melting, are very large, so that the liquid droplets are formed before the metal vaporizes. Thus at some stage in the vaporizing of the initiating wire, the discharge consists of a succession of metallic droplets connected by short electric arcs in the metal vapor.

Possibility of a Fine Filamentary Channel within a Luminous Column

The question often arises as to whether an electrical discharge at extremely high pressure consists of a fine filamentary current-carrying channel within a larger luminous column defined by the constraining walls of the discharge region. Such a filament would be laterally unstable due to its self-magnetic field, so that it would be continually whipping and writhing about, forming loops similar to oxbows in a river. These oxbows would become short-circuited and decay as the current assumed a new shorter path. If the lateral velocity of such a fine channel were sufficiently high, the entire volume of gas in the luminous column could be maintained in an excited state, and a photograph taken with an exposure time as long as one-quarter microsecond would only give the summation of a large number of lateral trips of the current-carrying channel. It would not be necessary to require that the ions or atoms of the gas attain a correspondingly high lateral velocity, since the current-carrying channel need be only a path of high ionization; and it could

pass on, leaving the slower moving atoms and recombining ions behind it. There are two reasons for anticipating such a fine channel. The similarity relations which hold for low pressure discharges predict that the equilibrium diameter of the current-carrying channel varies directly as the particle mean free path. If these relations were to hold for high pressures, the current-carrying channel would be small in cross section, similar to that in a lightning discharge or a conventional spark at atmospheric pressure. The second reason is based on pinch effect. If the rate-of-rise of current in an arc can be made high enough, so that large currents flow while the channel diameter is still small, it is conceivable that the pinch force would increase to such an extent that it alone would prevent expansion of the channel cross section. The pressures and temperatures within such a channel would be exceptionally high. This possibility has brought about several attempts, by researchers here and abroad, to try to develop temperatures of the order of one million degrees for the purpose of initiating a controlled thermonuclear reaction. No successful attempt in producing such temperatures has been announced to date. However, since the first draft of this dissertation was written, Russian scientists have announced the successful production of neutrons and hard X-rays in a high-current discharge in deuterium. The mechanism of production is ascribed not to an extremely high temperature but to ordered acceleration of electrons and ions in rarefied regions of the spark channel (24).

A diligent attempt was made, in the study of the underwater spark, to prove or disprove the existence of a fine filamentary channel. Photographs were taken of the spark while it was confined between closely spaced parallel blocks of glass or transparent plastic. The spark was bent around corners. A hairpin initiating wire was used, as well as parallel initiating wires, in order to see if the mutual magnetic fields would cause

the fine channel to be driven out of the luminous column. A large number of pictures were taken; not a single one gave any evidence of a fine channel. If there were a fine channel, the spark inductance would thereby be increased. With the discharge circuit used for the study of the underwater spark, the anticipated amount of increase would not be an appreciable fraction of the circuit equivalent inductance and would therefore be difficult to detect. The conclusion was therefore reached that the existence of a filamentary channel had been neither demonstrated nor disproven. Throughout the remainder of this study no attempt will be made to differentiate between the current-carrying channel and the luminous column. The current density across the cross section will be assumed uniform within an order of magnitude.

The 25-Kilovolt Underwater Spark

A complete sequence of Kerr cell camera photographs of the underwater spark is presented in Figs. 18 to 24. These are a part of the sequence of photographs which were scaled for the purpose of obtaining the channel diameter as a function of time. The 25-kilovolt, 5.8-microfarad discharge circuit was used; the sparks were initiated by a one-mil tungsten wire. The exposure time was one-quarter microsecond. The spark was 1.5 centimeters long, and the electrode on the right in the photographs was positive. The irregularities along the channel were created by bubbles of hydrogen which were produced electrolytically with the intent of measuring the spark pressure. The pressure measurement was unsuccessful, but the distortion of the bubbles gives an idea of the behavior of the water near the expanding channel. The water volume elements adjacent to the channel are being elongated in a direction tangent to the channel surface and perpendicular to the spark axis. The bubbles appear to fill with plasma from

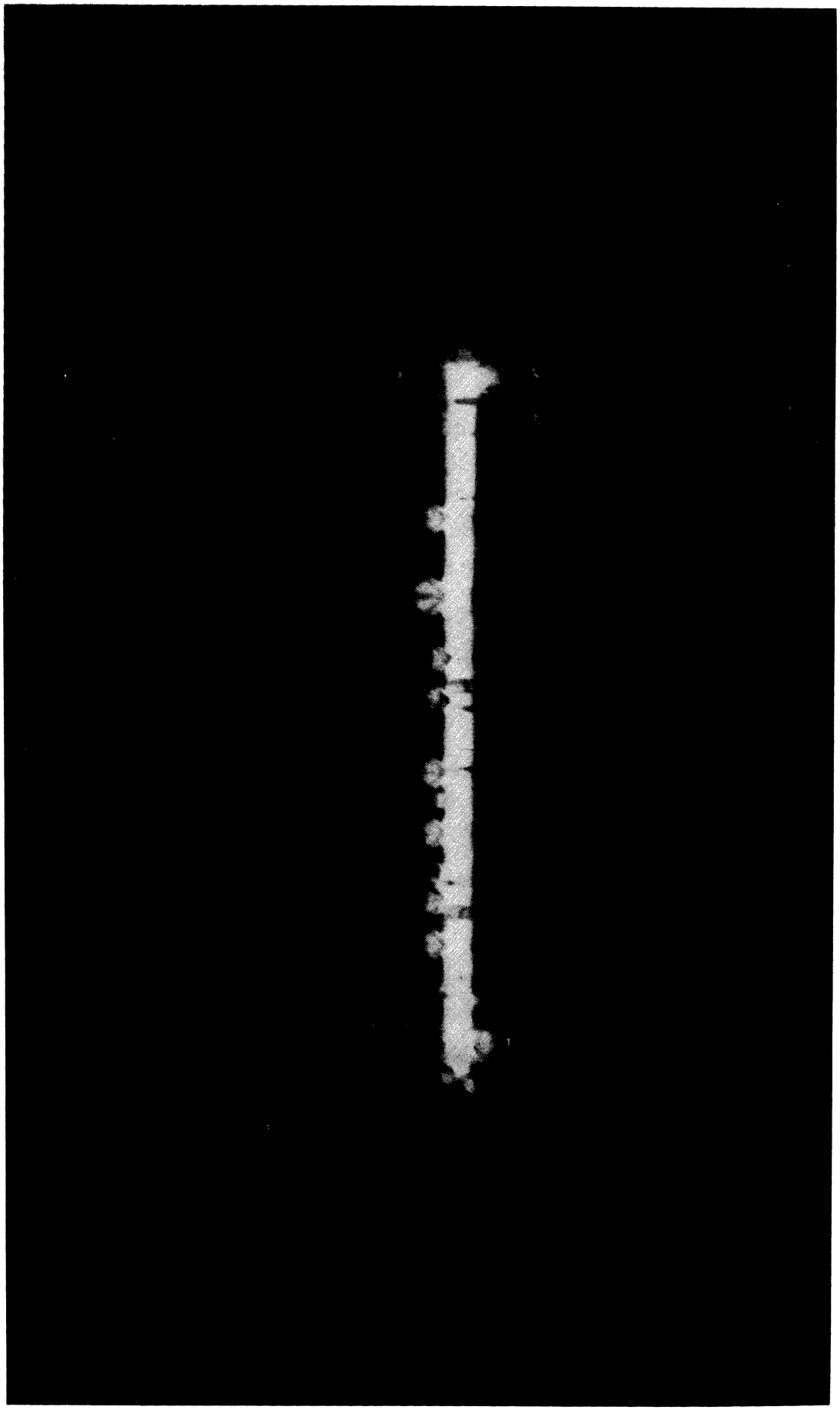

FIG. 18 TWENTY-FIVE-KILOVOLT SPARK AT 1/5 MICROSECOND

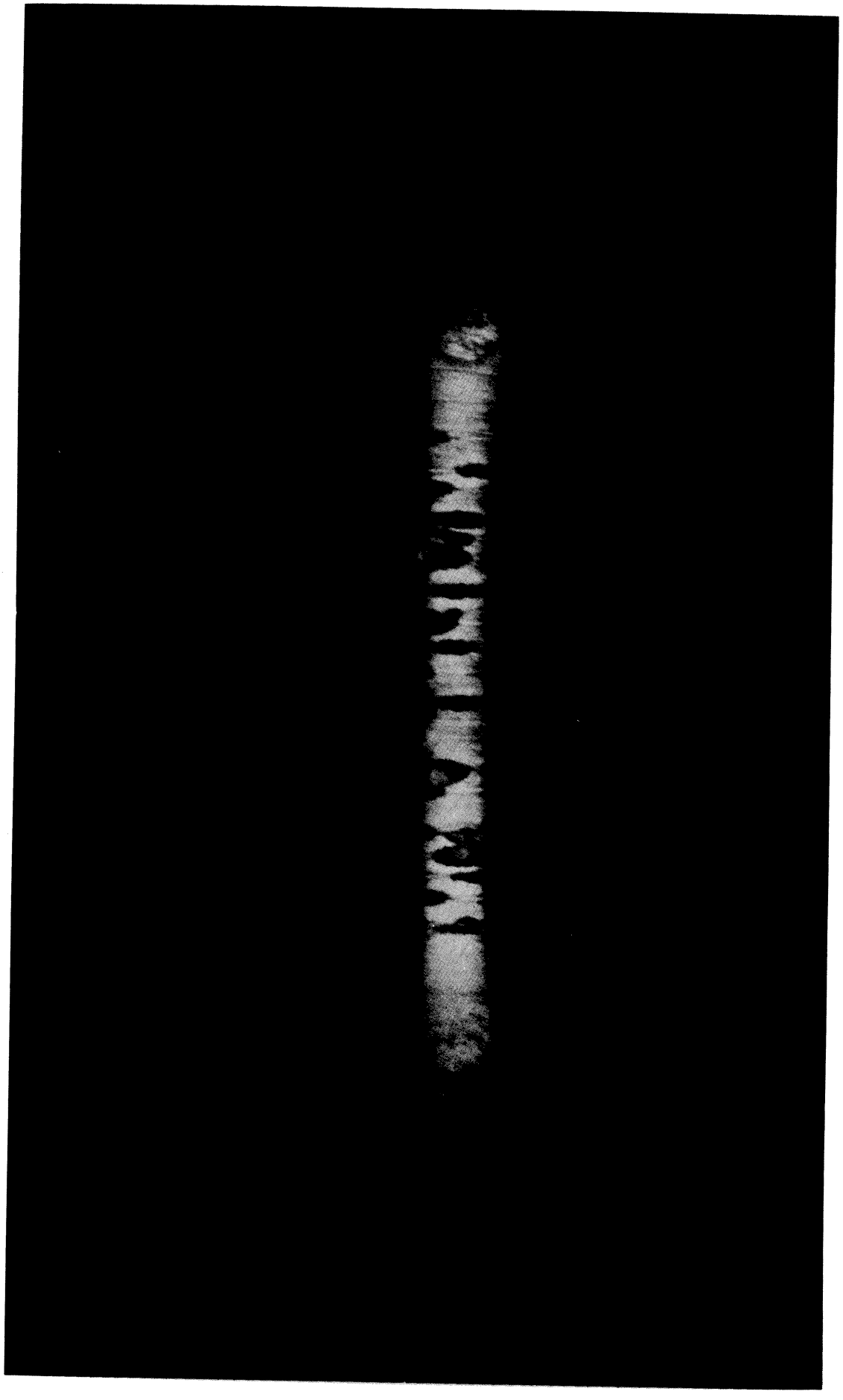

FIG. 19 TWENTY-FIVE-KILOVOLT SPARK AT 1 MICROSECOND

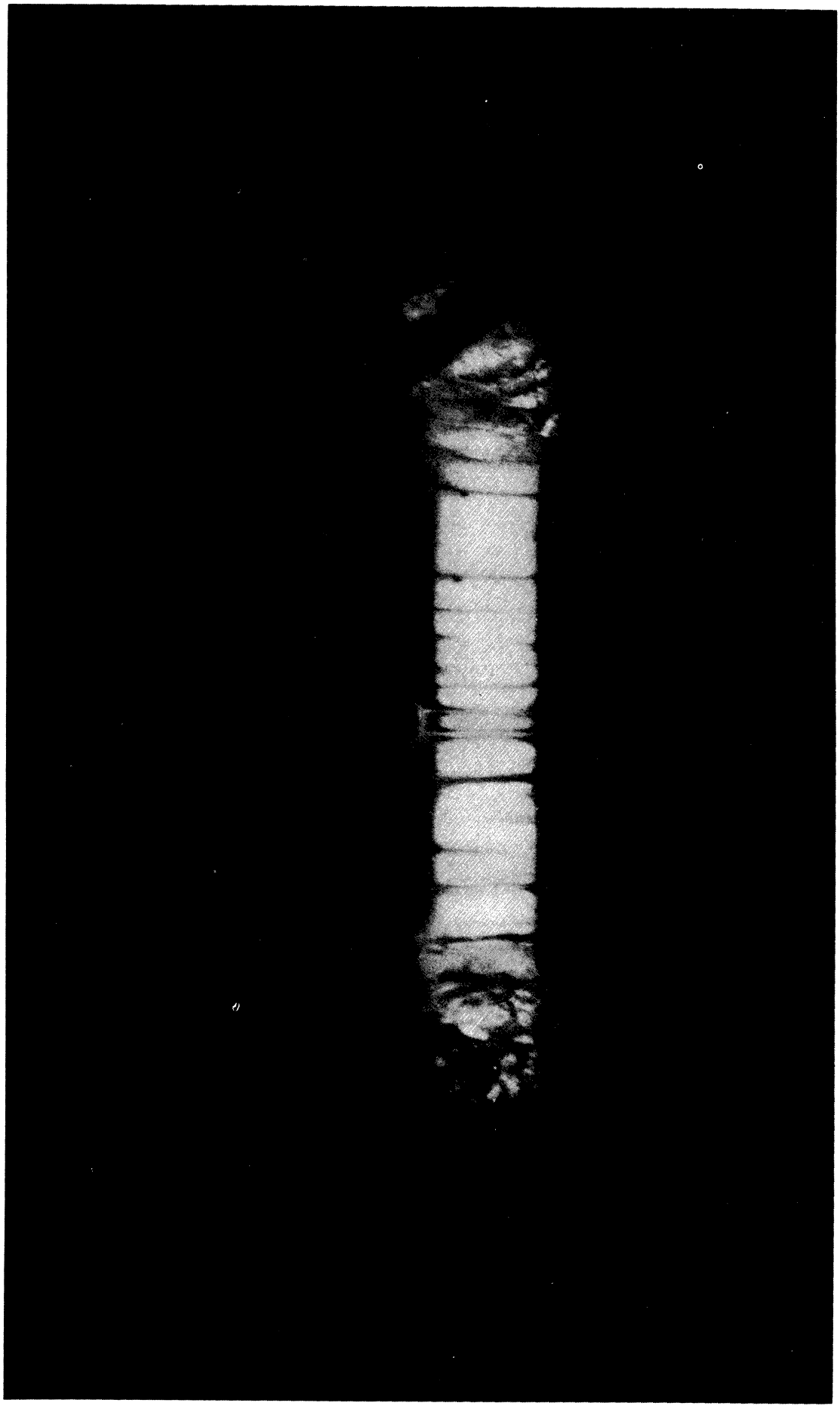

FIG. 20 TWENTY-FIVE-KILOVOLT SPARK AT 2.2 MICROSECONDS

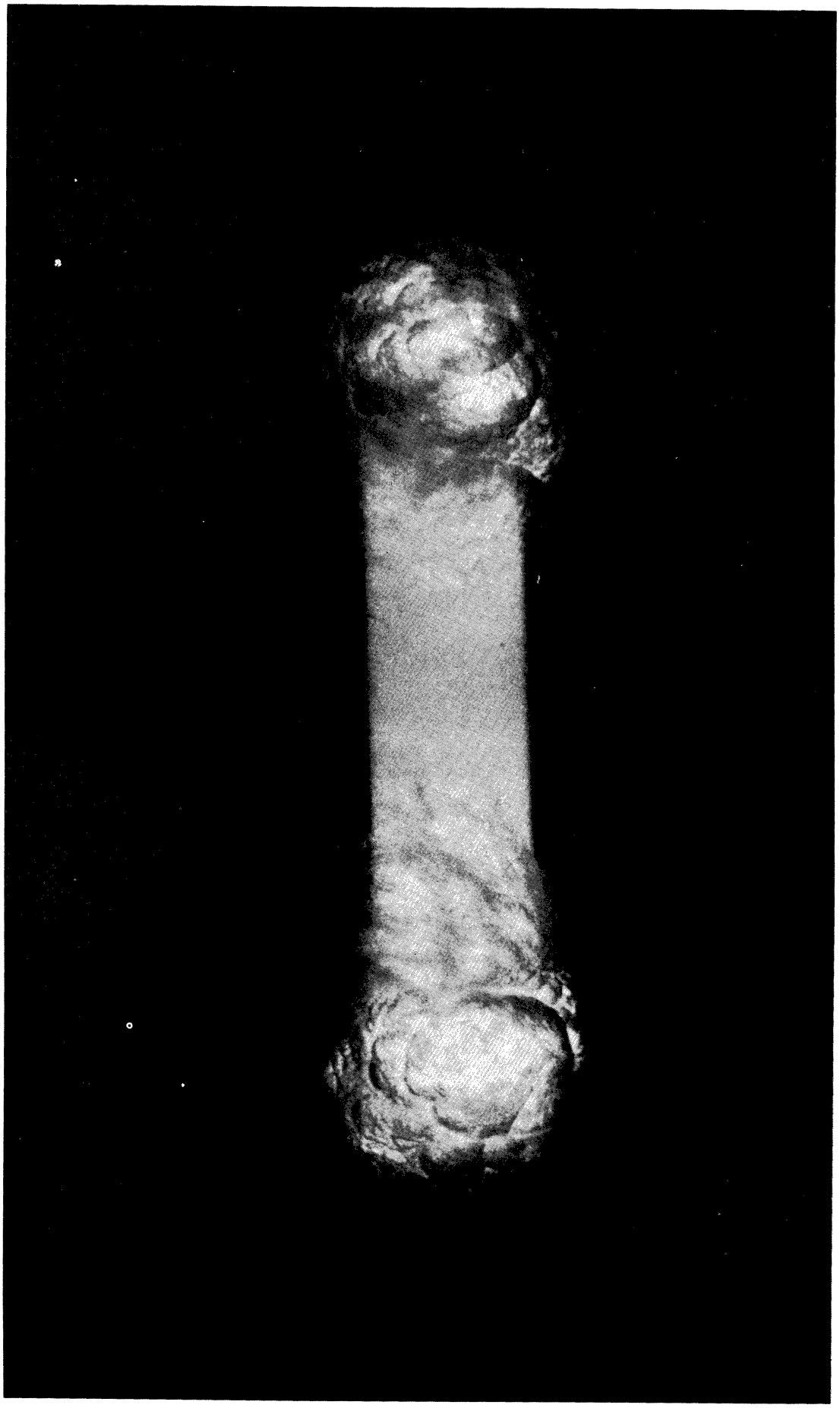

FIG. 21 TWENTY-FIVE-KILOVOLT SPARK AT 4.1 MICROSECONDS

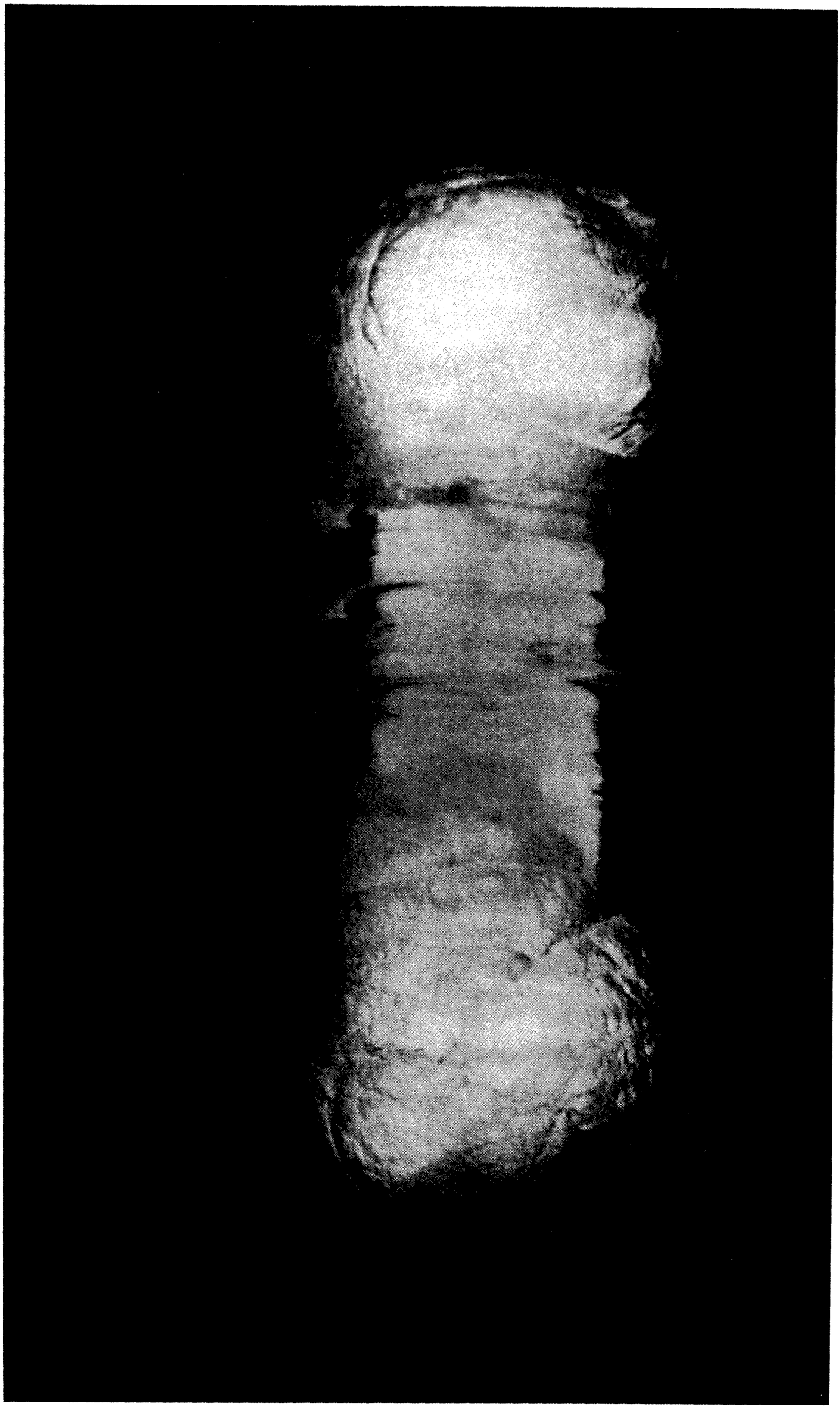

FIG. 22 TWENTY-FIVE-KILOVOLT SPARK AT 7.9 MICROSECONDS

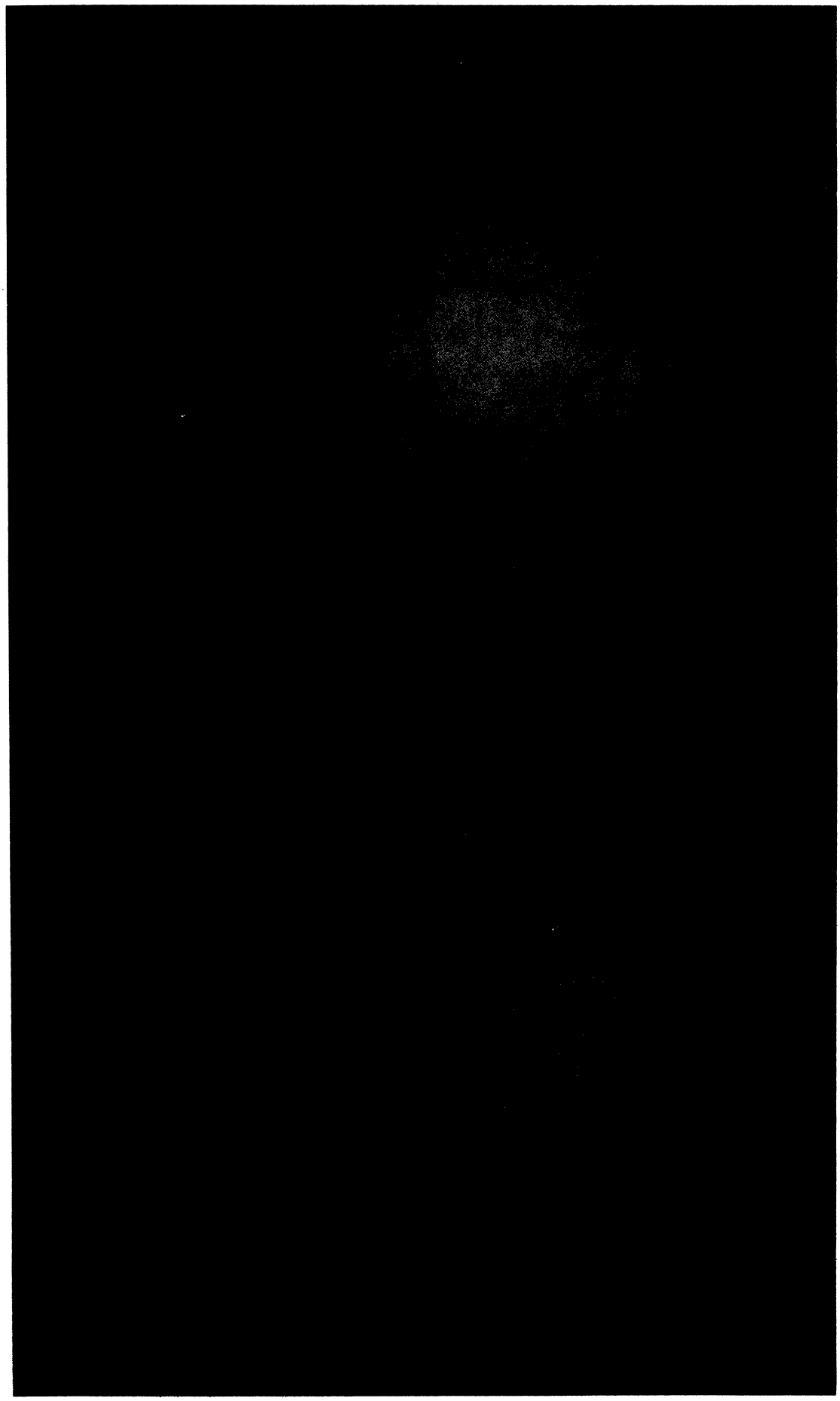

FIG. 23 TWENTY-FIVE-KILOVOLT SPARK AT 12 MICROSECONDS

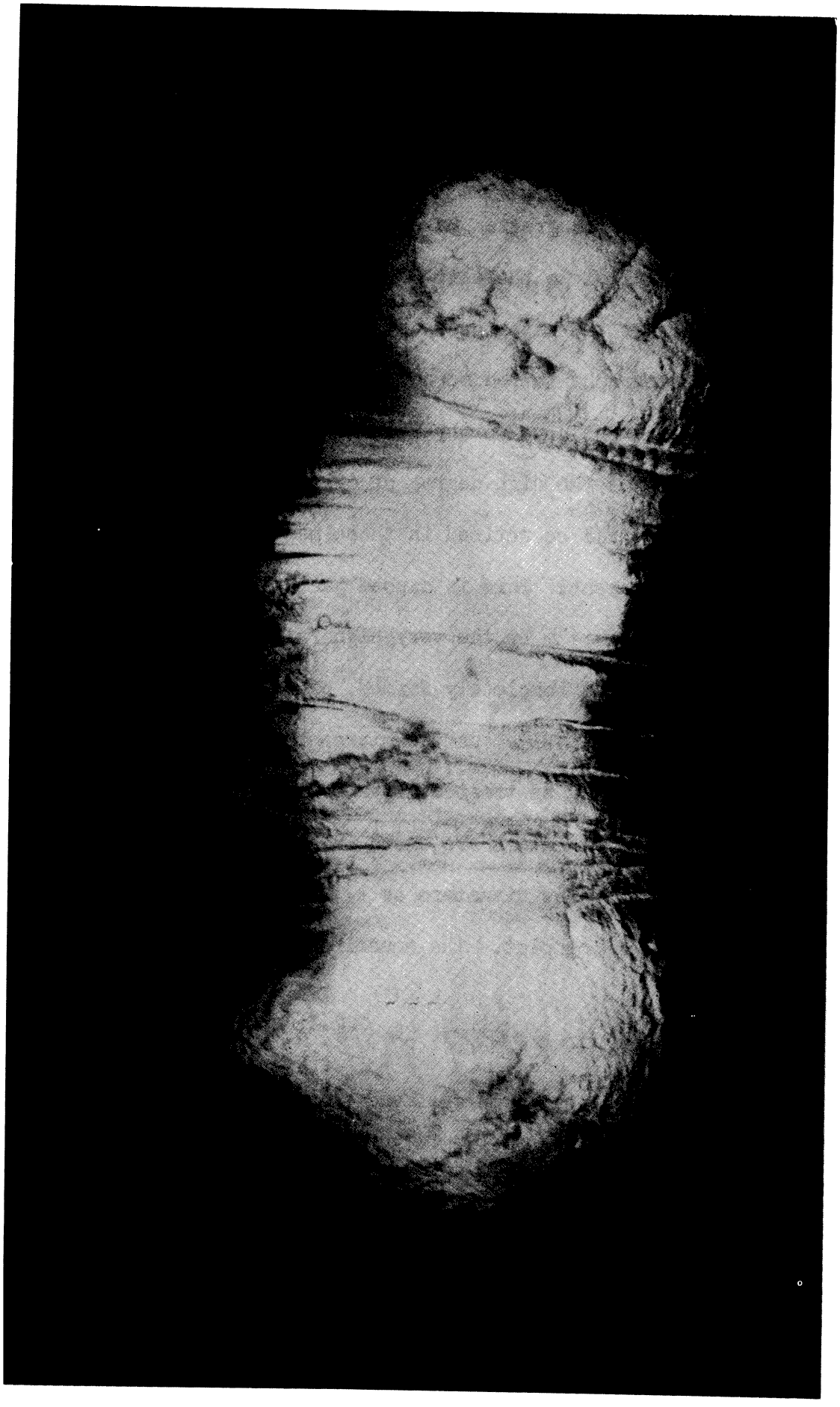

FIG. 24 TWENTY-FIVE-KILOVOLT SPARK AT 20 MICROSECONDS

the channel, and since no current flows through the bubbles, the isolated plasma begins decaying and cooling. The magnetic field at the surface of the channel is large, 13.5 webers per square meter at current maximum. This causes the coefficient of diffusion of the particles in the decaying plasma in the bubbles to be greater in a direction transverse to the channel axis than parallel to the axis. This, in combination with the transverse extension of the water produced by expansion, causes the bubbles in some photographs to become concentric rings which almost encircle the channel. One note-worthy feature of all the sparks produced by an initiating wire is the high degree of cylindrical symmetry about the channel axis. It will be noticed in these photographs that the striations are not apparent. This is caused partly by use of an initiating wire of small size and partly by the very high rate of power input. The unduloids are probably not completely formed, since vaporization of the wire follows melting so closely. On the microsecond time scale of this investigation, the wire may be treated as vaporizing instantaneously.

The scaled channel diameters are shown in Fig. 25. The simple empirical equation giving the diameters as a function of time was determined by means of a log-log plot. The equation for the 25-kilovolt spark is:

$$D = 1.80\, t^{0.523} \qquad (3.4)$$

where D is the diameter in millimeters, and t is the time in microseconds. Similar expansion curves were plotted for underwater sparks at different voltage and storage-capacitor values, and the curves were always approximately square-root curves. This general expansion characteristic is consistent with other published work on the rate of channel growth of spark channels (25, pp. 392, 396, 489).

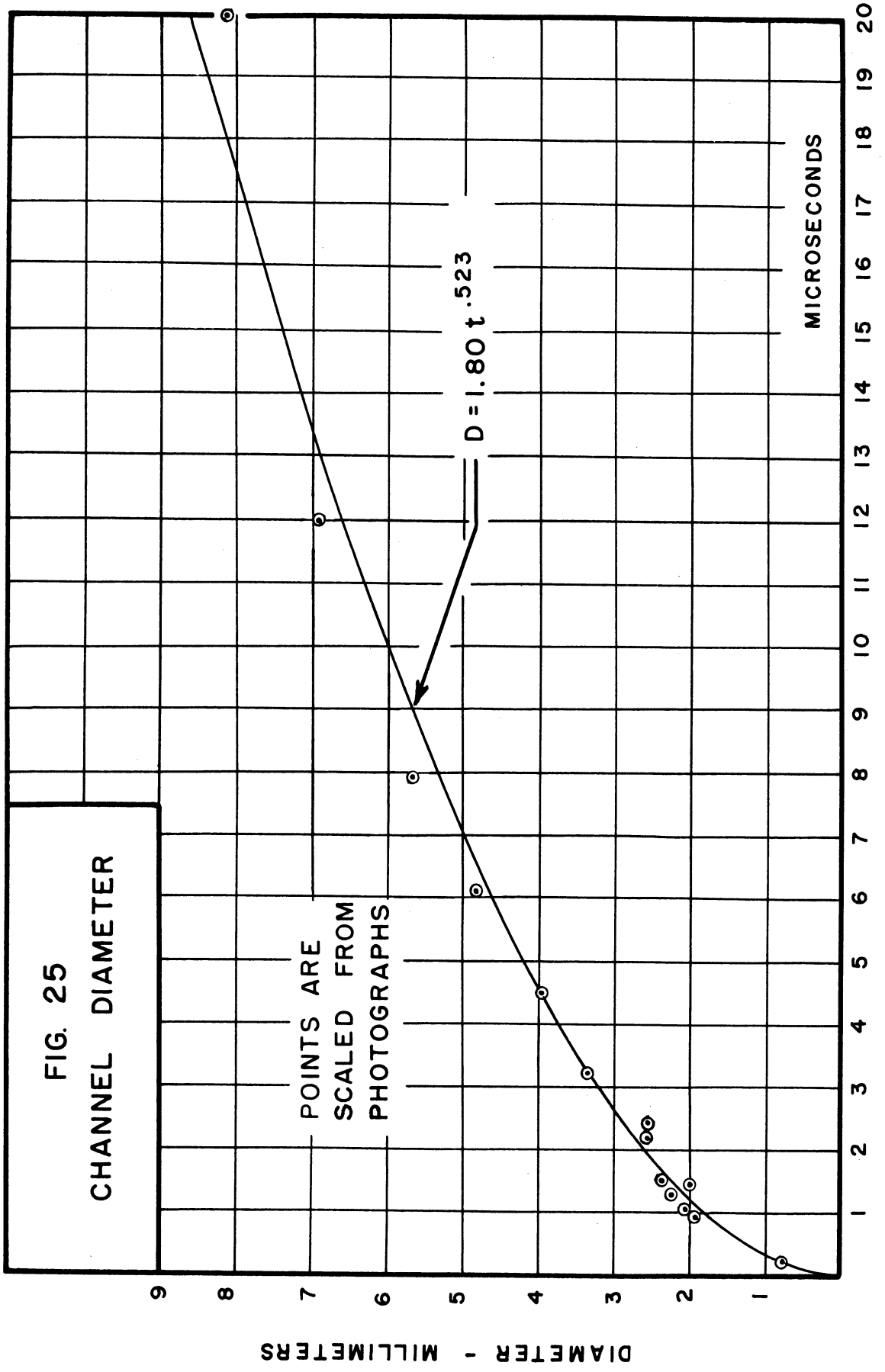
FIG. 25
CHANNEL DIAMETER
POINTS ARE SCALED FROM PHOTOGRAPHS
D = 1.80 t .523
MICROSECONDS
DIAMETER - MILLIMETERS

CHAPTER IV

THE PRESSURES DEVELOPED BY THE UNDERWATER SPARK

The feature of the underwater spark which gives it unique properties is the high pressure developed by the expanding spark channel. This pressure is transmitted to the surrounding water and generates a hydrodynamic shock wave. The pressures developed are not as high as those produced in materials by static compression as obtained by P. W. Bridgman, nor are they as high as those encountered in the submarine explosions employed in naval warfare. However, they are approximately one order of magnitude greater than the pressures of gas discharges which have been comprehensively studied and reported in the scientific literature, such as the work of Suits and of Peters at 1000 atmospheres which was mentioned earlier. From the viewpoint of the hydrodynamic problem, the underwater spark may be considered to be a small version of an underwater explosion.

The high pressures are developed by the inertia of the surrounding medium and not by the hydrostatic pressure. Thus the characteristics of the underwater spark do not depend markedly on the depth of the spark below the water surface, at least down to depths corresponding to pressures of the order of a thousand atmospheres. If one wished to develop higher pressures for a given rate of channel expansion, it would be necessary to use a surrounding medium having a density greater than that of water. Carbon tetrachloride has been suggested as a more dense liquid having the requisite transparency and low electrical conductivity.

Measurement of Pressure

A direct measurement of the pressures in the vicinity of the underwater spark presents a formidable problem. A suitable instrument for this measurement would require a sensitive element with an area of the order of one square millimeter or less and a properly damped response time much less than one microsecond; it must not be bulky enough to disturb the fluid flow pattern, and it must be insensitive to stray pickup from exceedingly strong varying electric and magnetic fields. Finally, unless the sensitive pickup were exceptionally strong, it would have to be expendable since most solids are ruptured by being placed close to the spark channel.

A reasonably accurate instrumentational determination of the pressures developed by the underwater spark has been found to be virtually impossible. The first indication of the magnitude of these pressures was obtained from the fact that the spark pressure is sufficient to punch a slug from a metallic sheet backed by a massive die. For the dimensions used, the hydrostatic pressure necessary to perform this operation may be calculated to be of the order of several thousand atmospheres. This "measurement" is analogous to the measurement of pressures in firearms by crusher gauges and is subject to the same criticism. The second approach to obtaining the pressure was to suspend several soft cotton fibers adjacent to the spark channel and parallel to each other. By discharging the spark and taking a Kerr cell photograph, and noting the change in spacing of the fibers on the photograph, the amount of water compression should be indicated provided that the cotton, which is completely permeated by the water, remains stationary with respect to the water for a time of the order of a few microseconds. Several

pictures showed that some of the water had apparently been compressed to one-third its normal volume. Such a compression ratio would require in excess of a million atmospheres. This pressure seemed too high, and in the light of later work it was concluded that the fibers had moved relative to the water or that optical refraction in the compressed water had displaced the fiber images.

Another attempt to measure the shock-wave pressures met with greater success, although the accuracy was low. The amount of refraction of a light ray traversing the compressed region was measured (Fig. 26). A regularly spaced wire grid was suspended near the underwater spark in such a position that it formed a background for a Kerr cell photograph of the spark. The grid was silver plated to increase its reflectivity, the necessary illumination coming from the spark itself. In order to obtain sufficient exposure so that the grid would be visible in the photograph, it was necessary to pre-expose or partially fog the film to increase its sensitivity. As a result the channel proper was overexposed. In the photographs the position of the shock front in the water could be seen by the discontinuity it produced in the image of the grid wires. The displaced images of the grid wires were visible behind the high-pressure region, but the wires were not sharply focussed because of the finite exposure time, and also because the compressed region itself produced defocussing.

The amount of refraction of the light rays was of the order of 3 degrees or less, and a large proportion of this was probably produced at the discontinuous shock front where the rays entered and left the high-density region. The variation of the index of refraction of liquids as a function of pressure has not been measured with a suitable degree of accuracy, nor over a sufficiently great pressure range, to be useful

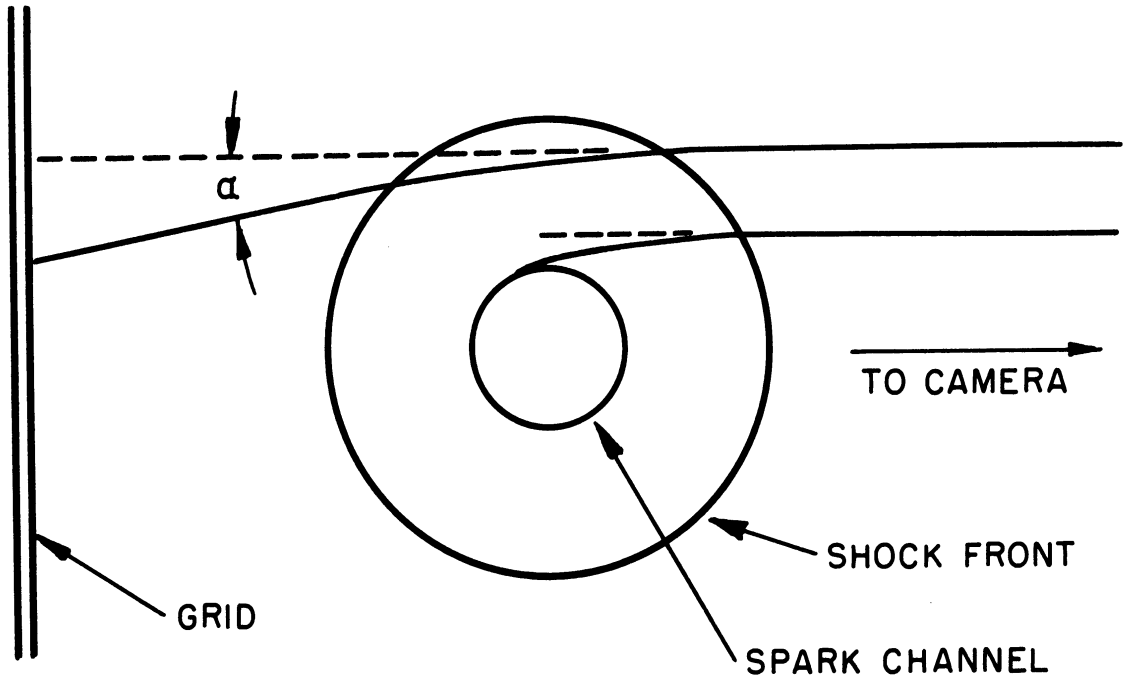

FIG. 26 LIGHT REFRACTION IN THE VICINITY OF THE UNDERWATER SPARK

here (26, p. 368). The difficulty is that either the measuring equipment must be completely contained within the pressure vessel, or else windows (which distort) must be used. An approximate relationship which has been found to apply at pressures up to several atmospheres is given by $\frac{n-1}{\rho}$ = constant, where n is the index of refraction, and ρ is the mass density of the liquid. This relation, as well as an equation of state to be discussed shortly, was used, since the present application does not call for a high degree of accuracy. The low resolution of these measurements as well as the uncertainty concerning the pressure variation of refractive index limited the accuracy of the determination to the order of magnitude only. The refraction approximately two microseconds after current initiation was found to be about the same as would be produced by a uniform cylinder of water under a pressure of from 2500 to 5000 atmospheres.

A final attempt to measure the shock-wave pressures was made by locating small bubbles near the spark. The electrodes and bubbles were first photographed under normal illumination from a lamp to establish the bubble sizes and then a Kerr cell photograph of the spark was taken as soon as possible thereafter to find the compressed size of the bubbles The bubbles were hydrogen, produced by electrolytic dissociation of the water. They were grown on the initiating wire or on some other object near the wire. The measurement was unsuccessful because the compressed bubbles became formless patches of light, to which definite boundaries could not be ascribed. Also, the presence of a solid supporting object seriously distorted the normal shock flow. When the bubbles were supported directly on the initiating wire, they merely filled with decaying plasma from the channel and did not compress appreciably. However, the distortion and subsequent behavior of the bubbles which were originally on the wire does give some insight regarding the behavior of the water adjacent to the spark-channel wall.

Shock Waves in Water

When it became evident that a measurement of the shock-wave pressures accurate enough for analytic use was not feasible, an extended attempt was made to calculate these pressures. The pressures should depend only on the rate of expansion of the cylindrical channel and on the characteristics of water, provided that the channel wall advances negligibly due to induction of water into the channel through its surface. The latter condition will be shown to be true later.

A large amount of interest has centered around the study of shock waves since World War II with the advent of fast-moving vehicles and missiles, atomic explosions, and increased emphasis on submarine military

operations. The most complicated studies are concerned with shocks in dissociating fluids, primarily air or combustion gases. These studies are a combination of fluid dynamics, chemical reaction equilibria, and thermodynamics. A second group of studies considers shocks in non-dissociating fluids, primarily water. These studies are simpler conceptually, but the mathematics still presents difficulties. Water, in addition to being nondissociating at pressures encountered in underwater explosions, is also a piezotropic fluid (27), i.e., a fluid with separable energy (28, p. 8). The simplest physical meaning of these terms may be summarized as follows:

When water is compressed rapidly, the pressure rises as a function of the increase in density. The resulting increase in temperature is sufficiently small so that the additional increase in pressure associated with the temperature rise is negligible compared to the original pressure increase. In other words, the ratio of specific heats, γ, is very close to unity. [For a rapid compression of water to 25,000 atmospheres, the temperature increases only about 85° C. (29, p. 40).] As a result the equation of state need contain only the pressure and density, and for practical calculations the effect of temperature changes may be neglected. The equation of state which has been found to hold in studies of underwater explosions is given by the following (28, p. 8; 29, p. 44):

$$P = A\left(\frac{\rho}{\rho_o}\right)^7 - B \qquad (4.1)$$

A and B are approximately 3000 atmospheres, and they differ by one atmosphere. P is the pressure at a density of ρ, and ρ_o is the normal density of water. The exponent of the compression ratio, 7, is the term which makes the shock-wave equations highly nonlinear and

difficult to solve. The practical significance of the separable-energy character of water is that, to a moderate degree of accuracy, a mathematical expression of the conservation of mass and momentum is sufficient tc specify the problem completely. The third important relation, conservation of energy, contributes only a small refinement to the solution which may be neglected in all but work of the highest degree of accuracy (28, p. 132).

The differential equations of non-steady, compressible fluid flow are readily available and will not be repeated here (28, p. 12). For the flow in the vicinity of an expanding cylinder, the Euler representation provides two first-order simultaneous partial differential equations, and the Lagrange formulation provides one second-order partial differential equation. At the time the work described in this dissertation was being carried out, the explicit solutions for spherical and cylindrical shocks in water were not available. A group at Stanford Research Institute is presently engaged in obtaining these solutions by use of a digital computer, which means that a step-wise method is being used which achieves accuracy through selection of small increments and continual revision of the solution as computation proceeds (30). Their problem is chiefly that of evolving a computational procedure which is adaptable to the computer.

Calculation of Spark-Channel Pressure

A complete solution to the cylindrical shock-wave problem, which would give the pressure as a function of time and position throughout the compressed region surrounding the underwater spark, could not be obtained. However, a partial solution giving the pressure and pressure gradient on the surface of the expanding cylinder was evolved. This

solution is sufficiently accurate to satisfy the present requirements, and it may also serve as a boundary condition for the more complete problem. The method consists of applying the Rankine-Hugoniot shock-front conditions in differential rather than finite form to the water at the surface of the expanding spark cylinder.

The Rankine-Hugoniot shock conditions are relations between the shock-front velocity and the pressures, densities, particle velocities, and internal energies on each side of the front (29, p. 35). The shock front is conventionally treated as a mathematical discontinuity, although it is realized that it has a finite thickness of the order of several mean free paths of the particles of the fluid. The first two shock relations, the so-called mechanical conditions, are expressions of the conservation of mass and momentum across the shock front. The third relation, expressing the conservation of energy across the shock front, is not necessary to achieve a solution, as a result of the separable-energy characteristic of water. The first two shock relations will now be applied to an infinitesimal change in pressure, density, etc., rather than to the usual finite, discontinuous change in the variables.

Consider a plane shock front traveling in the positive X-direction (Fig. 27). The so-called "front" in this case represents an infinitesimal change in the pressure, density, and particle velocity. These three parameters ahead of the front are given by P, ρ, and u respectively. The corresponding quantities behind the front are given by $P + \Delta P$, $\rho + \Delta\rho$, and $u + \Delta u$ respectively, where the increments all approach zero as the front is approached from behind. The velocity of the front is given by U. All velocities are, of course, X-directed. It will be shown later that U is always greater than u. Therefore, if the

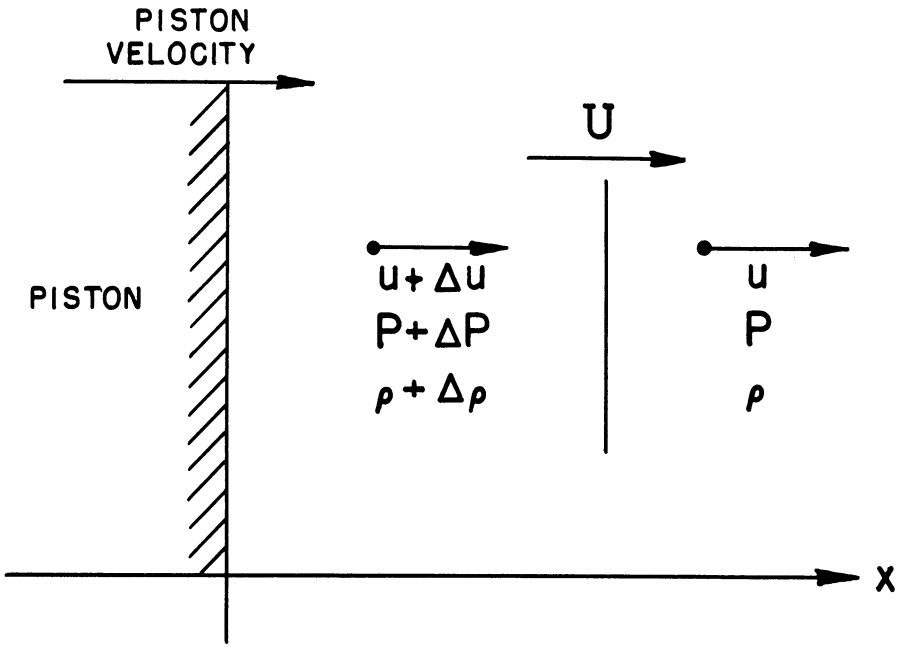

FIG.27 INCREMENTAL SHOCK FRONT

front is taken as the reference, fluid ahead of the front continually enters the front where its pressure, density, and particle velocity are changed by small amounts. Conservation of mass requires that the following relation be true:

$$\rho(U-u) = (\rho+\Delta\rho)\left[U-(u+\Delta u)\right] \qquad (4.2)$$

If the higher-order increment is neglected, one may convert this to the following:

$$U = u + \rho\frac{\Delta u}{\Delta\rho} \qquad (4.2a)$$

Conservation of momentum at the front gives the following equation:

$$(P+\Delta P) - P = \rho(U-u)(u+\Delta u-u) \qquad (4.3)$$

This may be written as follows:

$$\Delta P = (\rho U - \rho u)\Delta u \tag{4.3a}$$

Substitute 4.2a into 4.3a to obtain:

$$\Delta P = \frac{\rho^2 (\Delta u)^2}{\Delta \rho} \tag{4.4}$$

One may obtain the following from the equation of state of water, 4.1:

$$\Delta P = \left(\frac{7A}{\rho_0^7}\right) \rho^6 \Delta \rho \tag{4.5}$$

Eliminate $\Delta \rho$ between 4.4 and 4.5 to give

$$\Delta P = \left(\frac{7A}{\rho_0^7}\right)^{1/2} \rho^4 \Delta u \tag{4.6}$$

The equation of state also gives the following:

$$\rho^4 = \rho_0^4 \frac{(P+B)^{4/7}}{A^{4/7}} \tag{4.7}$$

Substitute into 4.6 to obtain

$$\frac{\Delta P}{\Delta u} = \frac{(7\rho_0)^{1/2}}{A^{1/14}} (P+B)^{4/7} \tag{4.8}$$

If the pressure is a continuous function of the velocity u, then as Δu approaches zero, so will ΔP and $\Delta \rho$ approach zero. None of the underwater-spark data which have been taken gives any evidence of a discontinuous change in pressure or density as the spark channel continuously expands. In fact, one would not expect a discontinuity in the pressure at the surface of the expanding cylinder unless the velocity of expansion were to change abruptly, or discontinuously. Therefore, as the

shock front is approached from behind, ΔP and Δu will both approach zero, and their ratio will approach the limit $\frac{dP}{du}$. Therefore Equation 4.8 gives

$$\frac{dP}{du} = \frac{(7\rho_0)^{1/2}}{A^{1/14}}(P+B)^{4/7} \tag{4.9}$$

The variables may be separated for integration, and the result is:

$$(P+B)^{3/7} = \left(\frac{3\rho_0^{1/2}}{7^{1/2}A^{1/14}}\right)u + K \tag{4.10}$$

The constant K is evaluated by noting that if the expanding cylinder were to stop expanding in such a manner that the velocity decreased to zero continuously, the pressure at the surface would decrease to one atmosphere. Since one atmosphere is small compared to B, substitution of the limit zero for P will not give an error greater than that caused by uncertainty in the equation of state, 4.1. K therefore may be assigned the value $B^{3/7}$, and the final equation is obtained as

$$(P+B)^{3/7} = \left(\frac{3\rho_0^{1/2}}{7^{1/2}A^{1/14}}\right)u + B^{3/7} \tag{4.11}$$

Equation 4.11 will be applied in such a manner as to give the pressure on the surface of an expanding cylinder having a wall velocity u. However, the magnitude of the pressure on the cylinder may be further modified by geometric divergence of the fluid flow lines, so that the actual pressure would be a function of two parameters, cylinder wall velocity and wall curvature. In the absence of a more comprehensive solution, Equation 4.11 will be used as a first-order approximation to the actual pressure. It will be found that Equation 4.11 gives pressures

which are in excellent agreement with those determined by Schaaffs for sparks in several kinds of organic liquids (31). Schaaffs measured the pressures adjacent to low-power underliquid sparks by means of X-ray absorption. His results give pressures of the order of 10,000 atmospheres for trichlorethylene. In the derivation and application of Equation 4.11, all effects produced by fluid viscosity have been neglected.

Application of the Pressure Equation

To establish a physical picture of the application of Equation 4.11 to a pressure calculation, a planar case will be discussed. Consider a planar piston initially at rest in water. Let the piston abruptly begin moving at a constant velocity. At the instant of starting, the pressure at the piston surface will instantly become a value which is given by the usual finite form of the Rankine-Hugoniot shock-wave relations. As the piston continues in motion, this step function of pressure will move away from the piston into the surrounding water. Provided that the piston continues at constant velocity, a lengthening column of compressed water will build up in front of the piston, and the pressure throughout the length of the column will be constant and equal to the original value when motion started. The important feature to note is that as long as the piston continues at a constant velocity, the pressure on its surface remains constant. The particle velocity behind the shock front is equal to the piston velocity, and ahead of the front the particle velocity is zero (Fig. 28). If the piston then abruptly increases its velocity to a new value, a second shock front will advance into the previously compressed region. The discontinuous increase in pressure is again given by the Rankine-Hugoniot equations; but as long as the piston continues in motion at this new velocity, the pressure on its surface

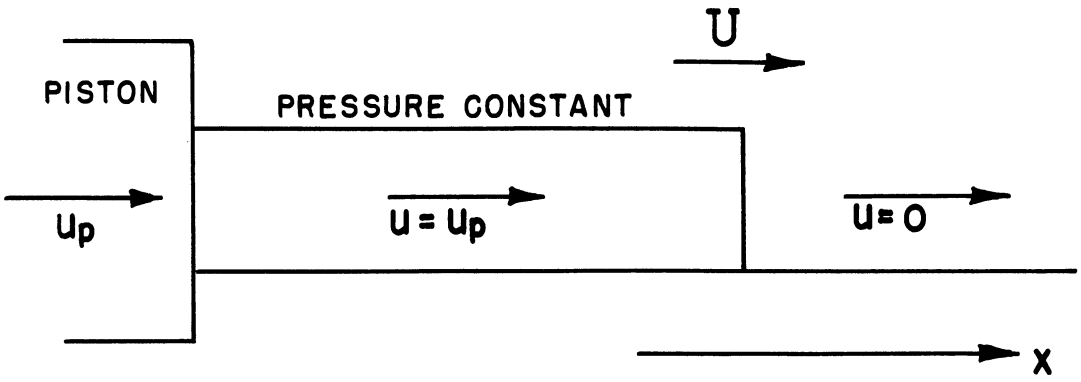

FIG. 28 PLANE SHOCK WAVE FOR CONSTANT PISTON VELOCITY

remains constant. Thus, whenever the piston changes its velocity, a shock front leaves its surface and advances into the water. This physical concept is now applied to the calculation of pressure on the piston surface by considering that the piston originates a continuous succession of fronts as the piston velocity varies in a continuous manner. Thus the front referred to in the development of Equation 4.11 is always the one at the piston surface. As soon as that front departs from the surface, a front immediately behind it is under consideration. From this it may be seen that u (Fig. 27) is the piston velocity since the water immediately adjacent to the piston must move at the same velocity. Equation 4.11 gives no information, and does not directly apply, at any finite distance from the piston; the equation gives only the pressure on the surface.

One requirement which must be satisfied if Equation 4.11 is to

have any physical meaning is that all incremental fronts must move away from the piston surface regardless of whether the incremental changes in piston velocity are positive or negative. U must therefore be greater than u, regardless of the sign of Δu. Equation 4.2a may thus be rewritten as follows:

$$U = u + \rho\left(\frac{\Delta u}{\Delta P} \cdot \frac{\Delta P}{\Delta \rho}\right) \tag{4.2b}$$

Equation 4.8 then gives

$$\frac{\Delta u}{\Delta P} = \frac{A^{1/14}}{(7\rho_0)^{1/2}\,(P+B)^{4/7}} \tag{4.8a}$$

and Equation 4.5 gives

$$\frac{\Delta P}{\Delta \rho} = \left(\frac{7A}{\rho_0^{7}}\right)\rho^{6} \tag{4.5a}$$

The proof is completed by substituting 4.8a and 4.5a into 4.2b, and using the equation of state, Equation 4.1, to give

$$U = u + \frac{7^{1/2}\,A^{1/14}}{\rho_0^{1/2}}\,(P+B)^{3/7} \tag{4.12}$$

The last term in Equation 4.12 is always positive. Also, the fact that a compression front will be propagated in **almost** all fluids whereas a rarefaction front will not, in no way limits the applicability of Equation 4.11 only to cases where the piston velocity, and hence pressure, **is** increasing. Any of the incremental fronts leaving the piston surface

may be propagated or may not propagate after departure from the piston, but this subsequent behavior does not modify the conditions at the piston surface, which is the only place where Equation 4.11 applies.

Calculation of the Off-Surface Pressure Gradient

We now have available the pressure on the surface of an expanding object in water. The preceding work also permits one to determine the pressure gradient on the expanding surface. There are two contributions to the total off-surface pressure gradient. One, independent of geometry, is produced by the changing velocity of the expanding surface, i. e., by the surface acceleration. The second contribution depends on the geometry and is produced by the geometric divergence of the fluid-flow lines. The first contribution to the off-surface gradient, being independent of geometry, will be discussed for the planar case. If the advancing planar piston has zero acceleration at any time, the off-surface gradient is zero. If the piston velocity varies continuously as a function of time, the off-surface gradient is given by the relation

$$\frac{dP}{dx'} = \frac{-\frac{dP}{dt}}{\frac{dx'}{dt}} \tag{4.13}$$

Here X' is distance in the X-direction measured from the piston surface, and $\frac{dx'}{dt}$ is the relative velocity between the piston and an incremental pressure change. This can be stated as

$$\frac{dx'}{dt} = U - u = \frac{7^{1/2} A^{1/4}}{\rho_0^{1/2}} (P+B)^{3/7} \tag{4.14}$$

Therefore the off-surface gradient is

$$\frac{dP}{dx'} = -\left(\frac{dP}{dt}\right)\left(\frac{\rho_o^{1/2}}{7^{1/2} A^{1/14} (P+B)^{3/7}}\right) \qquad (4.15)$$

If one wishes, $\frac{dP}{dt}$ may be evaluated in terms of $\frac{du}{dt}$ by means of Equation 4.11.

The second contribution to the off-surface gradient will be developed for the case of an expanding cylinder, since that suits the present application. However, it should be realized that the method applies equally well to any curved surface. In the case of a complex curved surface, the result is a function of the radii of curvature of the surface in two mutually perpendicular planes whose intersection is the normal to the surface at which the gradient is desired. Consider the volume element in Fig. 29. This element is taken to include a constant mass of fluid, hence its boundaries must continually change to compensate for the effects of the cylindrical geometry and for the expansion of the fluid as the pressure decreases. The mass inclosed is given by

$$m = \rho r \theta \ell \Delta r \qquad (4.16)$$

From the equation of state of water, Equation 4.16 may be rewritten as

$$m = \rho_o \theta \ell \left[\left(\frac{P+B}{A}\right)^{1/7} r \Delta r\right] \qquad (4.16a)$$

Take the time derivative of 4.16a, multiply through by $\left(\frac{P+B}{A}\right)^{6/7}$, and set the result equal to zero, noting that Δu equals $\frac{d}{dt}\Delta r$, to obtain

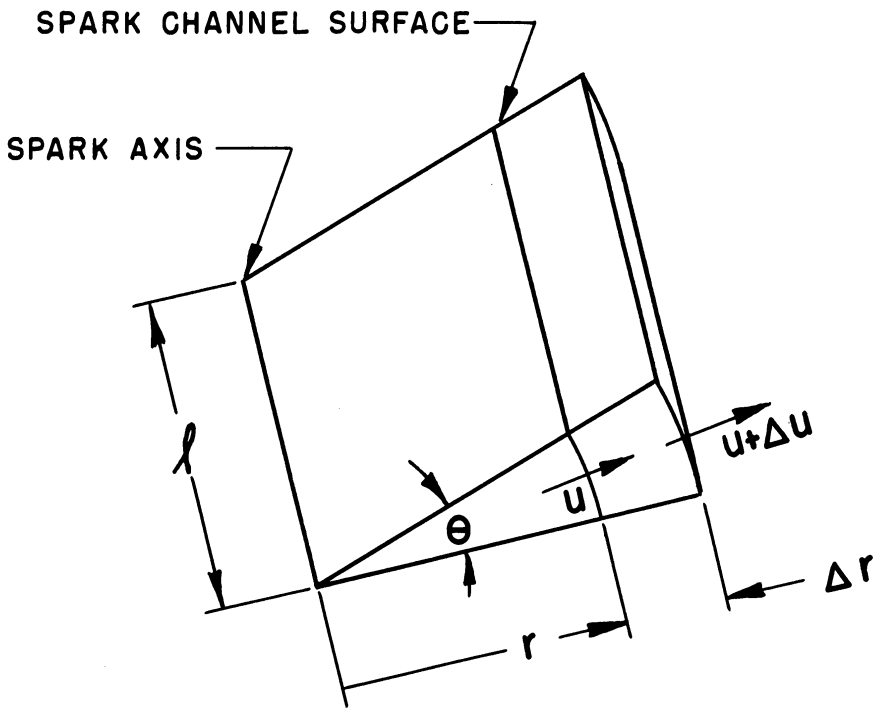

FIG. 29 CYLINDRICAL VOLUME ELEMENT

$$\frac{dP}{dt}\frac{1}{\gamma A}\, r\,\Delta r + \left(\frac{P+B}{A}\right)\left[r\,\Delta u + u\,\Delta r\right] = 0 \qquad (4.17)$$

Now divide through by Δr and take the limit as Δr approaches zero, giving

$$\left(\frac{P+B}{A}\right) r\frac{du}{dr} = -\frac{dP}{dt}\frac{1}{\gamma A}\, r - \left(\frac{P+B}{A}\right) u \qquad (4.18)$$

The result, when rearranged, is the following equation for the space rate of change of u.

$$\frac{du}{dr} = \frac{-\dfrac{dP}{dt}}{\gamma (P+B)} - \frac{u}{r} \qquad (4.19)$$

If the cylindrical surface at $r + \Delta r$ is regarded as a new expanding cylinder, and thus is itself generating the portion of the shock region outside that radius, the pressure at that point may be computed by means of Equation 4.11. Therefore one may state that

$$\frac{dP}{dr} = \frac{dP}{du}\frac{du}{dr} \tag{4.20}$$

Equation 4.9 gives

$$\frac{dP}{du} = \frac{(7\rho_0)^{1/2}}{A^{1/14}}(P+B)^{4/7} \tag{4.9}$$

The final relation is then

$$\frac{dP}{dr} = \frac{-(\rho_0)^{1/2}\frac{dP}{dt}}{7^{1/2}A^{1/14}(P+B)^{3/7}} - \frac{7(P+B)}{3r} + \frac{7(P+B)^{4/7}B^{3/7}}{3r} \tag{4.21}$$

This equation for the off-surface gradient reduces to Equation 4.15 in the case of a plane shock wave. As an example the gradient for the underwater spark may be computed at one microsecond, where P equals 11,600 atmospheres, r equals 0.90 millimeters, and $\frac{dP}{dt}$ equals -8.16×10^9 atmospheres per second. Equation 4.21 gives -21.5×10^{11} newtons per cubic meter, which is -21,500 atmospheres per millimeter.

The pressures at the surface of the underwater spark, as given by Equation 4.11, are plotted in Fig. 30, and are tabulated in Column 7 of Table III (p. 117). The wall velocities were taken from Equation 3.4, which in turn was obtained by scaling the Kerr cell photographs of the

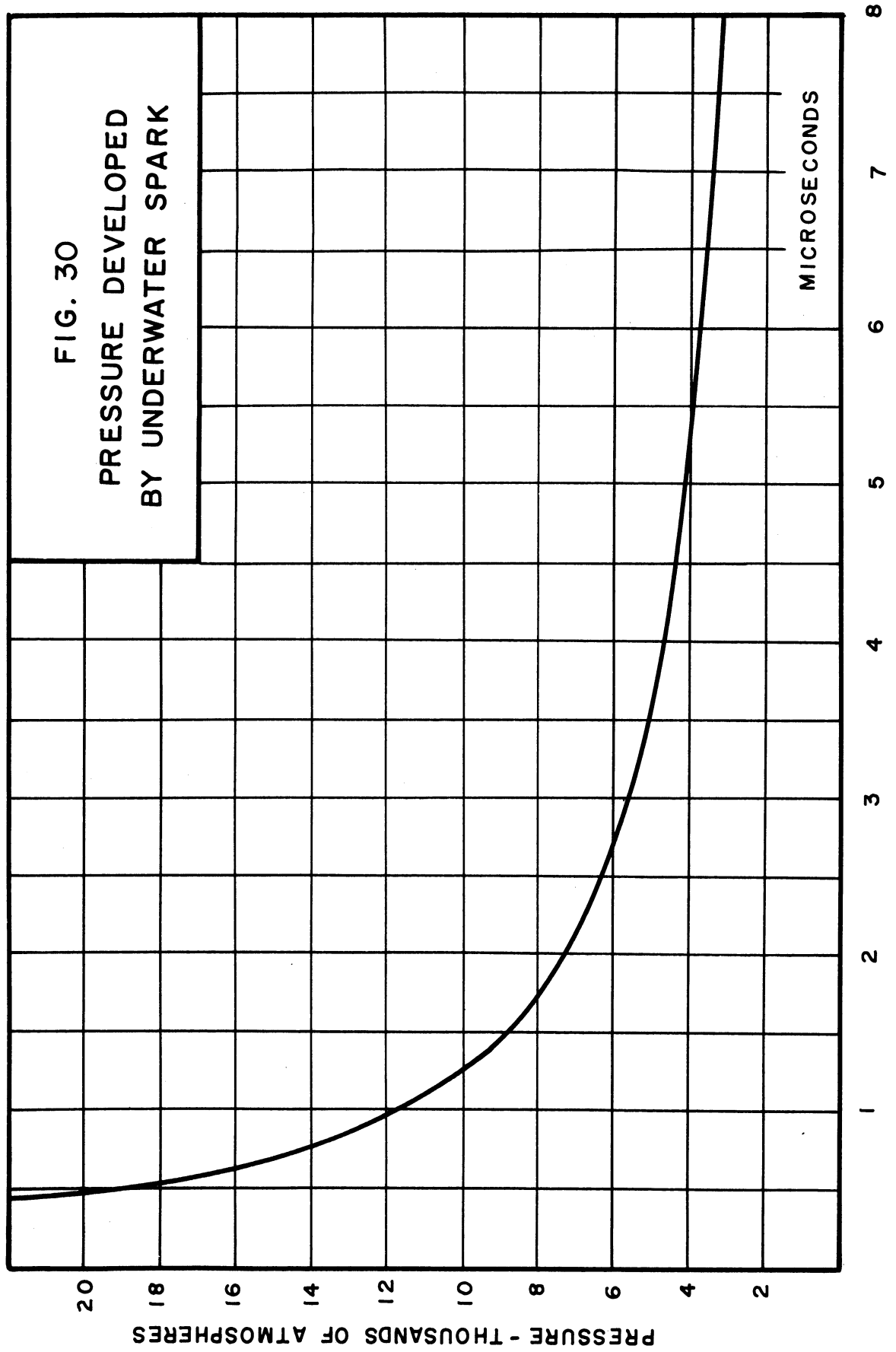
FIG. 30
PRESSURE DEVELOPED
BY UNDERWATER SPARK
PRESSURE - THOUSANDS OF ATMOSPHERES
20
18
16
14
12
10
8
6
4
2
MICROSECONDS
1
2
3
4
5
6
7
8

spark channel. Inasmuch as the expansion equation is approximately a square-root curve, the slope at zero time is infinite, which leads to infinite calculated pressure at zero time. This is not physically realizable, of course. The expansion curve should not be considered at all accurate during the first quarter-microsecond because of experimental inaccuracy during this period.

The pressures which have been computed are the pressures which the spark plasma exerts on its environment, the so-called external pressures. During the periods when the spark is carrying electrical current, the plasma is further confined by the pinch effect due to the self-magnetic field of the discharge. This pinch pressure turns out to be relatively unimportant compared to the total pressure within the plasma. Further, if the plasma does not behave as an ideal gas due to the presence of interparticle forces, the pressure within the plasma volume is greater than that which is obtained by adding the external and pinch pressures. This so-called internal pressure will be discussed later in the dissertation. For the present we will consider that the pressure in the plasma is the sum of the external and pinch pressures, and further, that the pressure is substantially uniform across the diameter of the spark channel. This latter assumption is based on the high ratio of pressure to mass density of the plasma gas, and on the approximately uniform power input per unit volume across the cross section of the spark channel. The evident ineffectiveness of the pinch force in causing an appreciable constriction of the current-carrying channel is the reason for considering that the input power density throughout the channel is constant.

CHAPTER V

THE TEMPERATURE OF THE UNDERWATER SPARK

One of the more noticeable phenomena associated with the underwater spark at high power levels is the brilliant, bluish-white flash emitted by the spark channel. This radiation has a continuous spectrum, and the spectral distribution of the radiant energy is that of a blackbody at approximately 30,000 degrees Kelvin. The light flash has a duration of about 28 microseconds, even though almost all the energy input to the spark channel takes place during the first 4 microseconds after current flow begins. This extended period of radiation indicates that a large portion of the input energy is stored initially in the spark channel, and this energy is relatively slowly radiated as the channel expands and decreases in temperature. This section of the dissertation is a description of the method by which the channel temperature was determined. The determination is based on absolute measurements of the amount of radiation from the spark channel.

Radiation from Electrical Discharges

The radiation from an electrical discharge in a gas may consist of spectral lines or a continuum, or possibly both may be present. Gases at low pressures, below approximately one-tenth atmosphere, radiate almost a pure line spectrum. This light is emitted by individual excited atoms decaying to lower energy states. Since the particle density is low at pressures under one atmosphere, each decaying atom radiates essentially as if it were isolated. A continuum, if detectably present at all, would consist of series-limit recombination continua; however,

these continua are usually not observed except during the early stages of sparks, when the ionization in the channel is very high (32). As the pressure is increased through the range from one-tenth atmosphere to pressures of the order of several hundred atmospheres, the emitted spectral lines gradually broaden and finally merge into a continuum. This broadening may be due to one or more phenomena:

The Doppler effect, arising from random motion of the radiating atoms, depends on the atom temperature, which in turn is usually higher at higher gas pressures. Collisional damping of the wave train from a radiating atom will shorten the duration of radiation and thus increase the line width. The Stark effect, produced by high random interparticle electric fields, distorts the atom wave function so that a group of atoms radiate a given line at slightly different frequencies. Recombination continua become stronger and contribute to the spectral continuum. In addition to the above effects, varying amounts of Zeeman splitting of the lines emitted by atoms in randomly varying local magnetic fields may contribute to the continuous nature of the spectrum. In the case of hydrogen, for example, a complete continuum is obtained at approximately 30 atmospheres (33, p. 188). The spectral continua obtained from discharges at pressures of the order of one-tenth to 100 atmospheres are in general not similar to the spectral distribution of radiation from a blackbody at any specific temperature. The spectra may contain many maxima which are the vestiges of spectral lines or groups of spectral lines; and a continuum may be produced as a result of many contributions from atom types having widely differing average random energies, or temperatures.

As pressures are increased further, appreciably above 100 atmospheres, an additional mechanism contributes to the radiation continuum. This is

the electron acceleration radiation, frequently called "bremsstrahlung." From the point of view of the energy-level diagram of an atom, this radiation may be considered as arising from free-free transitions (34, p. 63; 33, p. 110). In the presence of interparticle fields such as Coulomb forces, the electrons experience large accelerations as their random motions carry them throughout the plasma. For high particle densities, high degrees of ionization, or high temperatures, the corresponding random accelerations are large enough to cause appreciable radiation.

The spectral distribution of the radiation from a gas discharge having extremely high particle density, high pressure, or high temperature is thus seen to consist of broadened lines, recombination continua, and electron acceleration radiation; these types of radiation originate throughout the volume of the plasma. The Kerr cell photographs reveal that the underwater-spark channel has a high degree of opacity, at least in the visible region of the spectrum. Thus in various such photographs, the expanding channel has enveloped a solid object, and an image of the object is not visible below the channel surface. Treating the radiation from the point of view of quanta, the mean free path of a light quantum within the channel may be considered as being short compared to the spark dimensions. Thus a quantum originating deep within the channel is absorbed and re-emitted many times before it reaches and leaves the channel surface. The escaping radiation interacts many times with its environment in a manner analogous to the interaction between radiation in an enclosure and the walls of the enclosure. If the walls of the enclosure have a unique temperature, then a sampling of the radiation by means of a small exit hole reveals that the radiation has a Planckian spectral

distribution corresponding to the wall temperature. Similarly in the underwater spark, if all the particles with which the radiation interacts have the same temperature, i. e., are in thermal equilibrium, then the radiation escaping from the spark surface should have a Planckian spectral distribution corresponding to the particle temperature.

Thermal Equilibrium

The electrons and the heavier particles in low pressure electrical discharges do not attain thermal equilibrium because of the relatively infrequent elastic collisions between the two types of particles. In high pressure discharges, however, the coefficient of elastic energy transfer between electrons and heavy particles is larger because of a higher collision frequency. If the two particle types were assumed to have different average random kinetic energies, or temperatures, initially, then thermal equilibrium would be approached at a rate corresponding to a time constant of the order of 10^{-3} seconds (35, p. 335). If major parameters of the discharge change slowly compared to one millisecond, then all constituent particles may be treated as having substantially the same temperature. For such steady-state high pressure arcs the temperatures are of the order of 6000 degrees Kelvin.

If pressures and temperatures are of the order of magnitude which are encountered in the underwater spark, the time-constant to establish thermal equilibrium is much less than one millisecond. Details of the computation of this accommodation time-constant are presented, with a bibliography, in a summary report by H. Edels (36). The time-constant which will now be determined agrees as to order of magnitude with that calculated from the work presented by Edels. Energy may be transferred from the electrons to the ions or atoms of the spark channel by means of

elastic collisions, inelastic collisions in which excitation and ionization are produced, and by emission and absorption of radiation. We consider only the transfer by elastic collisions; the resulting time-constant obtained will therefore be an upper limit to the true value. The reduction of mean free path of the electrons which is caused by the strong Coulomb interparticle fields will be neglected. This procedure will also tend to give a time-constant greater than the true value. The calculation will be carried out for conditions at current maximum, 1.9 microseconds after current initiation.

The simplified kinetic-theory value of the electron mean free path, based on the assumption of hard elastic spheres, is equal to the reciprocal of the geometric collision cross section of the atoms and ions with respect to electrons. The equation is

$$\ell_e = \frac{1}{N_g \pi r^2} \tag{5.1}$$

where

ℓ_e is the electron mean free path,

N_g is the particle density of atoms or ions, and

r is the radius of the elastic spheres representing the atoms or ions.

Since atomic particles, with few exceptions, all have essentially a radius of the order of one Angstrom, this value will be used in the present approximate calculation. The electron mean free path in the underwater spark at current maximum, calculated according to the above, is 207 Angstroms. This should be recognized as an upper limit to the true value since interparticle forces have been neglected. The electron collision frequency, which is the ratio of mean free path to average

random velocity, is given by

$$f_c = N_g \mu^2 \sqrt{\frac{8\pi kT}{m_e}} \qquad (5.2)$$

The average fraction of electron kinetic energy transferred to the heavier particles per elastic collision is approximately

$$\text{Fraction} \simeq \frac{8}{3}\frac{m_e}{M} \qquad (5.3)$$

where M will be taken to be the weighted average mass of the heavier particles (35, p. 43). If E is the average energy of the electrons, the following equation may be written:

$$\frac{dE}{dt} = -N_g \mu^2 \sqrt{\frac{8\pi kT}{m_e}}\ \frac{8}{3}\frac{m_e}{M} E \qquad (5.4)$$

The solution is an exponential with a time-constant:

$$\tau = \frac{3M}{\sqrt{8\pi m_e kT}\ N_g \mu^2} \quad \text{seconds.} \qquad (5.5)$$

If this time-constant is determined at current maximum for the underwater spark, the result is 7.9×10^{-11} seconds. This compares well with the value calculated from the work summarized by Edels, which leads to a time-constant of 3.4×10^{-11} seconds. Therefore, on the time scale of this investigation, where the gross aspects of the spark channel are varying slowly compared to 10^{-4} microseconds, the various particle types may be considered to be in thermal equilibrium. From the point of view of the detailed behavior of the processes taking place within the spark channel, the spark may be treated as a succession of steady-state arcs.

This would not be true if the spark temperature, dimensions, or current were to vary appreciably in times of the order of 10^{-4} microsecond.

Spectrum of the Underwater Spark

A small Hilger quartz spectrograph was used to confirm the conclusion that the underwater spark at high power levels radiates a pure continuum. No attempt was made to check the variation of intensity with wavelength; a spectrograph of greater dispersion would be required to get significant data. Kodak type 103-D (backed) plates were used. Wavelength calibration was carried out by means of a Hanovia 125-watt mercury arc lamp, and measured wavelengths were determined by use of a Hartmann diagram (37, p. 233). The spectrograph was found to have a dispersion of approximately 330 Angstroms per millimeter at 2300 Angstroms. The spectrum of the spark was found to be a continuum, devoid of any line structure, from 3400 Angstroms to 6900 Angstroms; this result was obtained independently of whether or not a one-mil tungsten initiating wire was used. The 6900-Angstrom limit was set by the sensitivity of the spectral plates. By using the spectrograph to measure spectral transmission, it was found that the 3400-Angstrom limit was set by the transmission limit of the plexiglas window in the water tank. The Ann Arbor city water was found to have appreciable transmission down to 2400 Angstroms. With no absorber between the spectrograph and the mercury arc except air, lines were visible down to about 2300 Angstroms.

In addition to having the foregoing properties, the underwater spark channel is a diffuse radiator. The Kerr cell photographs show that the spark channel has a sensibly uniform apparent brightness across its cross section, showing that the radiant intensity from a small area element obeys Lambert's law. This simplifies the interpretation of the

radiation measurements in terms of a channel surface temperature.

Measurement of Temperature

The temperatures corresponding to the random energies of various particle types in gas discharges at low pressures (including discharges which are usually called high pressure discharges) may be made by measuring the amount of spectral line broadening or the distribution of intensities of individual lines in spectral bands (36). This is in addition to the Langmuir probe technique which yields the electron temperature in low pressure discharges. In the absence of spectral lines or bands, one must resort to a measurement of the intensity of the continuum; if the continuum obeys Planck's law, then a discrete temperature may be associated with the random motion of the particles generating the continuum. A conventional method of determining the temperature of a blackbody radiator is to measure the relative radiant flux at two wavelengths, and the ratio determines the temperature. However, if measurements are to be made in the visible region of the spectrum, where water, plexiglas, and air are quite certainly transparent, and if the temperature is of the order of 30,000 degrees Kelvin, then the ratio of the two measurements is a very insensitive function of the temperature. This is because the visible region falls out on the "tail" of the Planck blackbody curve. To get the temperature with a reasonable degree of accuracy would require extremely precise measurements at the two selected wavelengths.

A more suitable method of measuring the temperature of a blackbody in the range of 30,000 degrees Kelvin is to make an absolute measurement of the radiant flux at one wavelength. Since the flux at a given wavelength varies exponentially with the temperature, this method is

capable of good accuracy. The temperature of the underwater spark was determined in this way. Two completely independent absolute measurements were made at two wavelengths. The two measurements serve to check each other and to confirm the conclusion that the spark does radiate as a blackbody.

The two narrow regions of the spectrum at which measurements were made were isolated by the use of Farrand interference filters. These filters consist of vacuum-deposited layers of certain materials, and they operate on the principle of the Fabry-Perot interferometer (18, p. 93). The filter used for the red measurement had a peak transmission of 38 percent at 6450 Angstroms and a half-bandwidth of 190 Angstroms. The blue measurement was made with a filter of 25 percent peak transmission at 4190 Angstroms and a half-bandwidth of 120 Angstroms.

The phototubes which were used for the temperature measurements were calibrated by use of a tungsten-ribbon microscope illuminating lamp (G. E. Type 18A, 6 volts, 18 amp.). This lamp has a filament well suited to radiation measurements, since the relatively cooler ends of the filament which are in contact with the supporting leads are not visible from the front (Fig. 31). The filament has a rectangular projected area of 0.19 x 0.80 centimeters as determined with a cathetometer, and the total temperature variation from the center to the ends was found to be approximately 20 degrees centigrade. The filament temperature as a function of lamp current was measured with two Leeds and Northrup disappearing filament optical pyrometers. These instruments were calibrated by use of a blackbody and give the apparent temperature on the basis of the intensity of radiation in the effective passband of the instrument red filter at about 6650 Angstroms (38, p. 1131). The

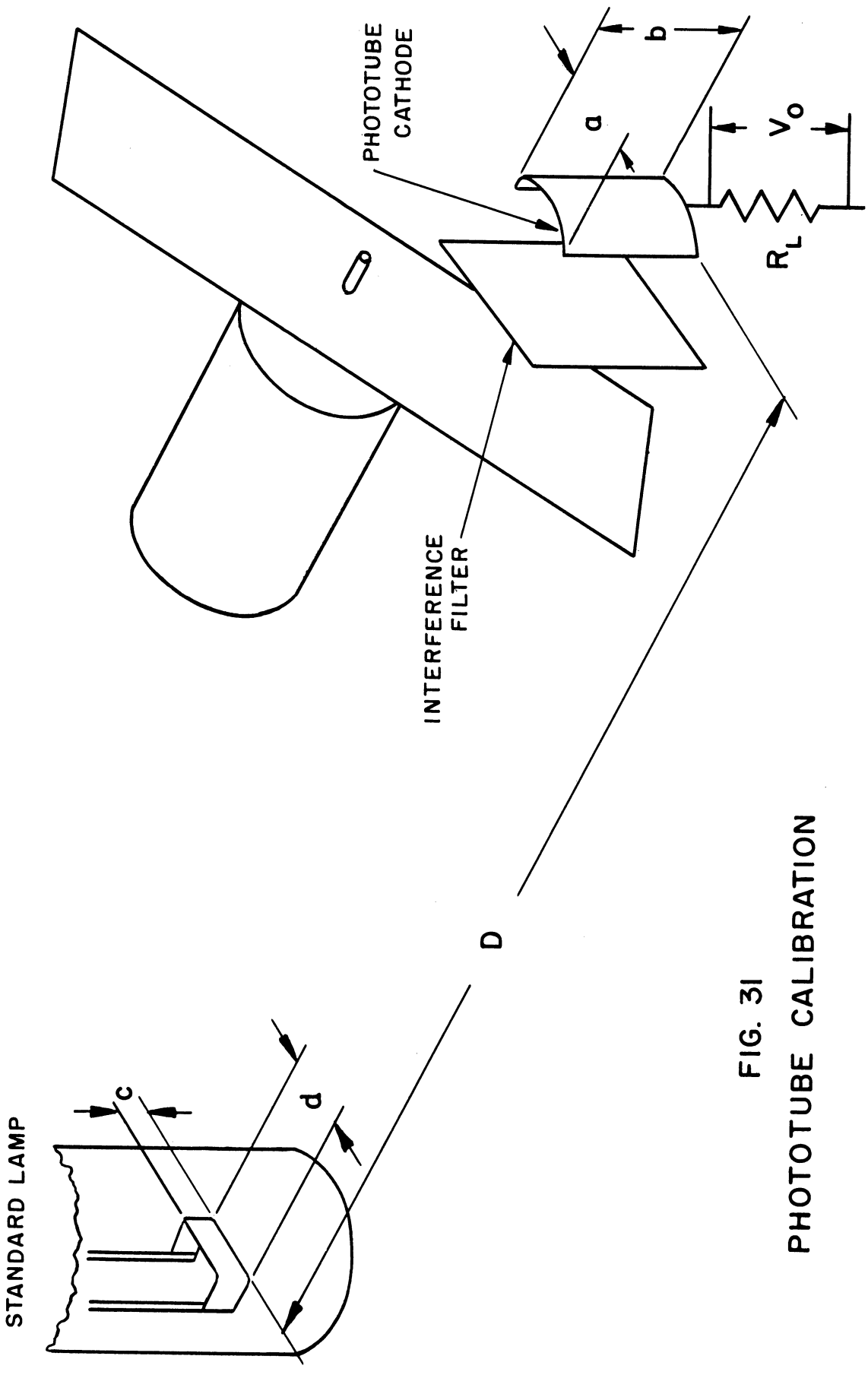

FIG. 31
PHOTOTUBE CALIBRATION

sensitivity of these instruments is such that a deliberate missetting of the calibrated potentiometer by as little as ± 10 degrees centigrade produces a very noticeable mismatch between the wire and the background. The readings taken with these two instruments agreed within several degrees.[1] The true temperature of the filament was calculated using the published values of spectral emissivity of tungsten at various temperatures (39). It was found necessary to operate the standardized lamp on direct current since the use of 60-cycle alternating current produced approximately 30-percent modulation of the light output in spite of the relatively large thermal capacity of the tungsten ribbon. Also, since the lamp was operated slightly above its rated current, care was taken to calibrate the phototubes before the lamp had appreciable additional operating time in order to minimize the effect caused by envelope blackening.

The measurement at the red end of the visible spectrum was made with a Type 926 phototube. This has an S-3 response and a rated sensitivity at 6450 Angstroms of 7.67×10^{-4} microamperes per microwatt. The blue measurement was made with a Type 929 phototube having an S-4 response and a rated sensitivity at 4190 Angstroms of 4.12×10^{-2} microamperes per microwatt. The phototubes were each mounted within a separate aluminum shielding box having a small window across which the interference filter could be placed. The circuits, shown in Fig. 32,

---

[1] It should be noted that a third L. and N. instrument, obtained from the metallurgical laboratory, did not agree with these two instruments. The reason was that this third pyrometer had been calibrated on a temperature standard having the same 6650A emissivity as some specific metal surface, and thus read the true temperature for that type of metal only.

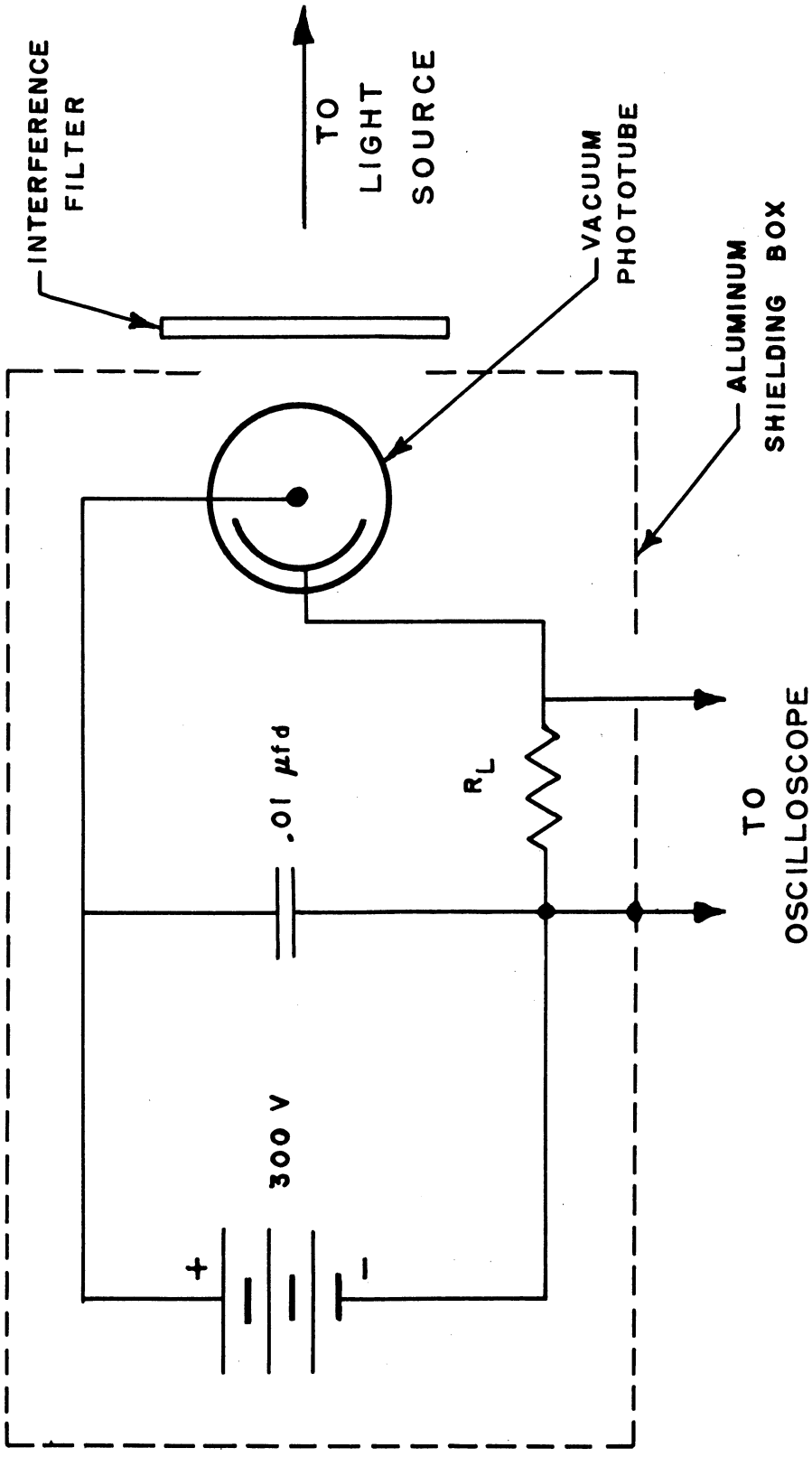

FIG. 32 PHOTOTUBE CIRCUIT

are conventional. The battery was a 300-volt Geiger counter battery, also enclosed within the box. The 0.01-microfarad capacitor assured that the tube voltage would remain near 300 even if the battery should develop appreciable internal resistance. The only part of the circuit exposed to stray pickup was the twisted pair of oscilloscope leads, which were less than one inch long.

For the calibration of the phototubes, a mechanical light chopper was used so that the resulting 53-cycle, square-wave signal could be amplified by the oscilloscope preamplifier (Fig. 31). The standard lamp filament was operated at a true temperature of 3143 degrees Kelvin. For the 926 phototube, D was 20 centimeters; the projected cathode area measured by a cathetometer was given by 1.5 x 2.4 centimeters, and a 0.120-volt signal was developed across the 343,000-ohm load resistor. The resulting sensitivity, based on two such calibrations, was found to be 6.15×10^{-4} microamperes per microwatt. For the 929 phototube, D was 19.8 centimeters, the measured projected cathode area was 1.6 x 2.2 centimeters, and a 0.135-volt signal was developed across the 57,200-ohm load resistor. The resulting sensitivity, based on two calibrations, was 4.70×10^{-2} microamperes per microwatt. The resistances of the load resistors were determined with a Leeds and Northrup type 5300 Wheatstone bridge. The sensitivity η of the phototube in microamperes per microwatt is given by

$$\eta = \frac{V_0 \pi D^2}{R_L J_\lambda E_{\lambda,T} (1.5 T_p \theta_{1/2})(a \times b)(c \times d)} \qquad (5.6)$$

where

J_λ is the intensity of radiation per micron of a blackbody at the true temperature of the lamp filament,

$\varepsilon_{\lambda,T}$ is the surface emissivity of tungsten at the appropriate wavelength and temperature,

T_{p0} is the peak transmission of the interference filter,

$B_{1/2}$ is the half-bandwidth of the interference filter,

and all remaining quantities are defined in Fig. 31.

The proper functioning of the two phototube circuits was thoroughly checked experimentally. In order to keep the response time of the circuits short, the load resistors used for the actual measurements were smaller than those used for calibration. By making reasonable assumptions as to the amount of stray lead capacitance, and considering the oscilloscope input capacitance, the calculated response time-constants were found to be less than one microsecond. To confirm the conclusion that the response times were short, a General Electric type FT-130 flash unit was used. The rated duration of the flash from this unit is two microseconds. All phototube circuits used for measurements successfully followed the two-microsecond pulse and, in addition, showed the successive smaller pulses which are the result of the decaying oscillatory current of the flash circuit. In both measurements and calibration, the phototube circuits were checked for stray electrical pickup by interposing an opaque, nonmetallic object in front of the phototube. In all cases stray pickup could not be detected until the sensitivity of the oscilloscope amplifier was increased by more than one order of magnitude. All phototubes were checked for gas amplification by maintaining a constant light flux and varying the anode voltage, meanwhile measuring the tube current with an accurate ammeter. The linear, almost horizontal characteristic showed that negligible gas was present. Finally, in both the calibration and measurements,

the linearity of response of the phototube and circuit was checked by varying the distance between the tube and the light source. The signals were found to obey the inverse-square law. An approximate calculation showed that the largest phototube currents which were encountered in any of the measurements were substantially less than one percent of the space-charge limited flow, eliminating the possibility of space-charge saturation of the phototube.

The light measurement in the red was made with a load resistor of 12,700 ohms, using a separation of 3.81 meters between the phototube and the underwater spark; the resulting oscillogram is shown in Fig. 33. The measurement in the blue was made with a load resistor of 2530 ohms, using a separation of 7.77 meters between the spark and the phototube; the resulting oscillogram is shown in Fig. 34. The shapes of these traces are the composite effect of an expanding channel and a decreasing temperature, so that the light output in the red reaches its maximum later than does the output in the blue. The long duration of light output from the spark compared to the time during which appreciable power is supplied to the spark is evidence that a large fraction of the energy is stored within the channel. Also, well-exposed Kerr cell photographs may be successfully taken of the spark channel at times even later than 20 microseconds, further confirming that the radiation continues long after appreciable electrical energy input to the channel has stopped.

In determining the temperatures from the light measurements the underwater spark may be treated as a diffusely radiating cylinder of length L and radius R. Let D be the distance separating the spark cylinder from a small unit area (Fig. 35). The unit area

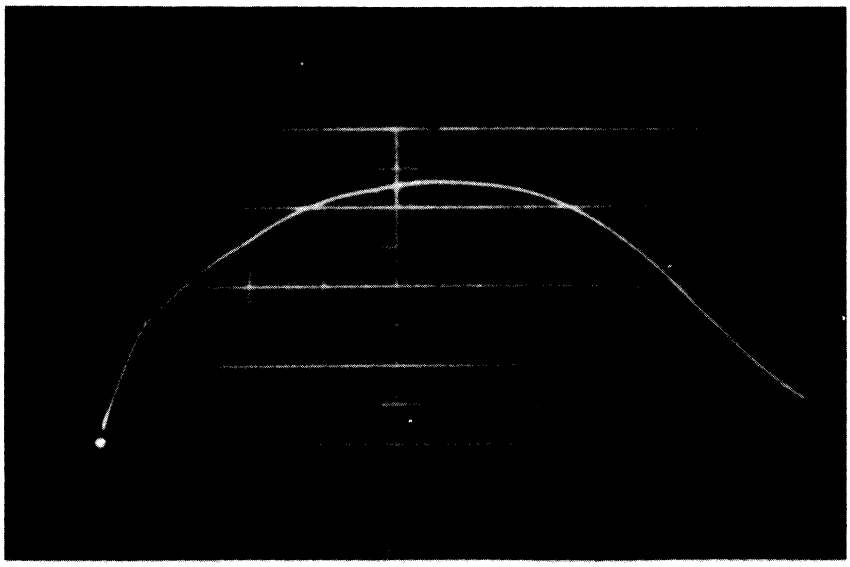

FIG. 33 OSCILLOGRAM OF LIGHT OUTPUT AT 6450 ANGSTROMS

SCALE FACTORS:

VERTICAL— 0.05 VOLT PER DIV.

HORIZONTAL— 4 MICROSEC. PER DIV.

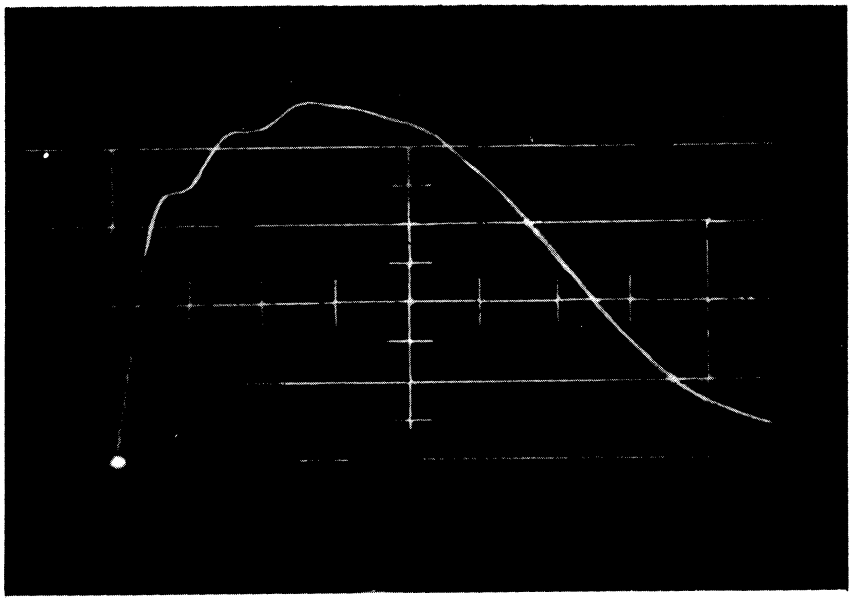

FIG. 34 OSCILLOGRAM OF LIGHT OUTPUT AT 4190 ANGSTROMS

SCALE FACTORS:

VERTICAL— 0.2 VOLT PER DIV.

HORIZONTAL— 4 MICROSEC. PER DIV.

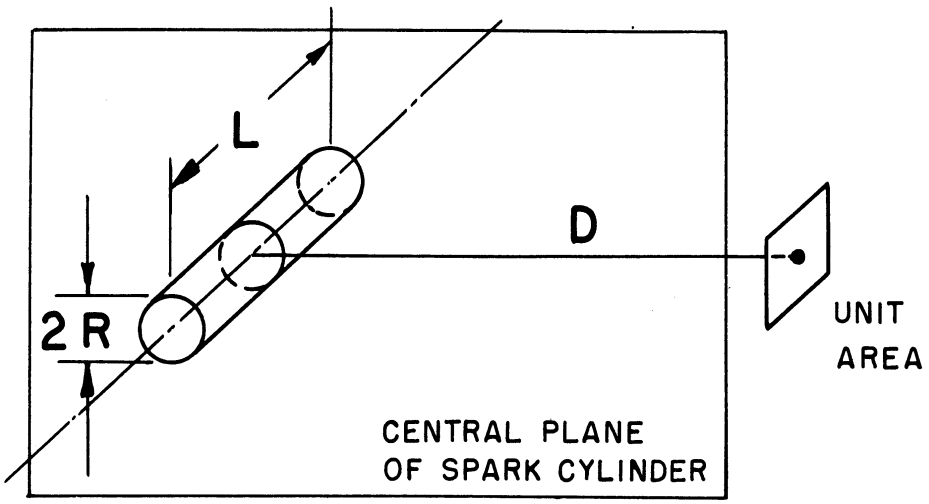

FIG. 35

GEOMETRY OF THE LIGHT MEASUREMENT

is located on the central plane of the cylinder and is oriented normal to the distance D. Then if D is large compared to the dimensions of the cylinder, the radiant flux E falling on the selected unit area is given by

$$E = \frac{J}{\pi} \frac{2RL}{D^2} \tag{5.7}$$

where J is the intensity of radiation through unit area of the cylinder surface. This equation, together with the phototube sensitivity η, interference filter constants, and signal voltage V_0, may be used to compute the intensity of radiation from the spark-channel surface; thus

$$J_\lambda = \frac{V_0 \pi D^2}{R_L \eta (1.5 T_p B_\lambda)(a \times b) 2RL} \tag{5.8}$$

where J_λ now refers to the spark-channel surface, and all other terms have the same meanings as defined for Equation 5.6 and 5.7. The value of J_λ as obtained from Equation 5.8 may be used with Planck's law to get the channel surface temperature. With the wavelength λ expressed in microns, the numerical form of Planck's law is

$$J_\lambda = 37{,}350\,\lambda^{-5}\left(e^{\frac{14380}{\lambda T}} - 1\right)^{-1} \qquad (5.9)$$

It will be noted that the product of peak transmission and half-bandwidth in Equations 5.6 and 5.8 has been multiplied by a factor 1.5. It was found, by integrating a typical transmission curve for an interference filter, that the transmission-bandwidth integral was very close to 1.5 times the product of peak transmission and half-bandwidth. The use of this factor in no way affects the calculated temperature for the spark since the factor appears once in calibrating the phototubes and once in calculating the temperatures, and in such a way as to cancel. The use of this factor, however, gives a suitably realistic calibration of the phototube sensitivity to use for comparison with the manufacturer's ratings, and it was therefore included.

The signal voltages scaled from the two light-measurement oscillograms, together with the resulting calculated temperatures, are summarized in Table I and presented graphically in Fig. 36. The average of the two temperature measurements was taken as the surface temperature of the underwater spark. While the spark-channel temperature measurements were in progress, the channel temperature was occasionally calculated from a red and a blue measurement for spark conditions somewhat different from those discussed in this study. The temperatures based on red measurements were consistently somewhat lower than those

TABLE I

SUMMARY OF TEMPERATURE MEASUREMENTS

TIME	VOLTS SIGNAL		TEMPERATURE °K		
μ sec	λ = 6450A	λ = 4190A	λ = 6450A	λ = 4190A	AVERAGE
1/2	.0264	.216	23,400	27,500	25,450
1	.0448	.344	26,200	29,100	27,650
1 1/2	.0575	.483	26,800	31,500	29,150
2	.0679	.602	27,200	32,800	30,000
2 1/2	.0782	.666	27,400	32,500	29,950
3	.0874	.690	27,800	31,400	29,600
3 1/2	.0920	.694	27,400	30,000	28,700
4	.0977	.698	27,100	28,900	28,000
4 1/2	.103	.726	27,000	28,400	27,700
5	.106	.768	26,500	28,600	27,550
5 1/2	.113	.805	26,600	28,400	27,500
6	.118	.832	26,800	28,200	27,500
6 1/2	.119	.846	26,200	27,800	27,000
7	.122	.846	25,800	27,200	26,500
7 1/2	.125	.846	25,700	26,600	26,150
8	.130	.851	25,800	26,200	26,000

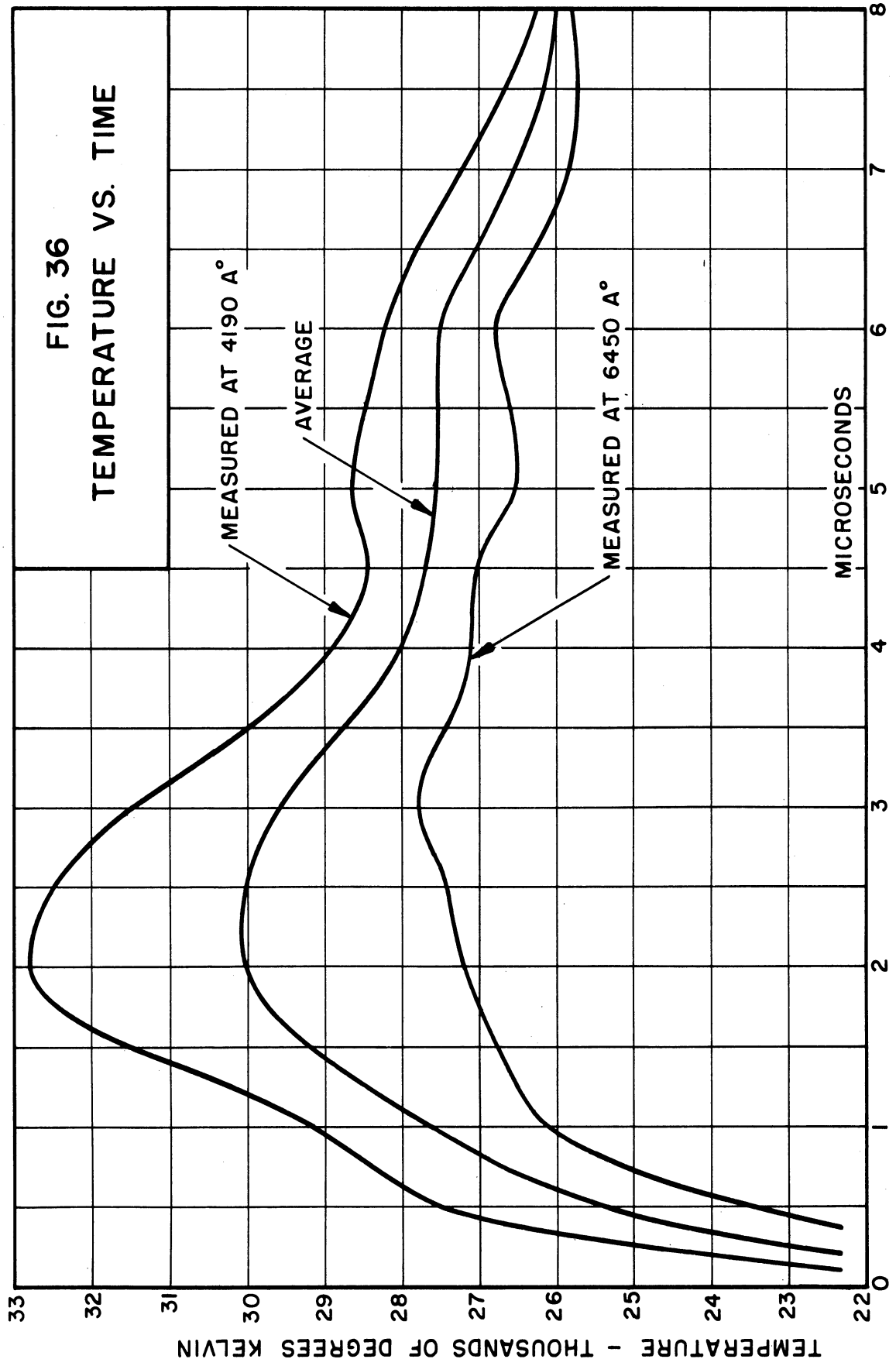
FIG. 36
TEMPERATURE VS. TIME
MEASURED AT 4190 A°
AVERAGE
MEASURED AT 6450 A°
MICROSECONDS
TEMPERATURE - THOUSANDS OF DEGREES KELVIN
0
1
2
3
4
5
6
7
8
22
23
24
25
26
27
28
29
30
31
32
33

based on blue measurements. This difference, if it actually exists, could be caused by either of two phenomena. First, in all the preceding work it was tacitly assumed that the spark-channel surface had a spectral emissivity of unity. If the emissivity is less than unity, even though it may be independent of wavelength, then the true surface temperature will be greater than that determined from either the red or blue measurement; and the blue measurement will always give the higher temperature. The second possibility is that the spark plasma has a different absorption coefficient for red and for blue radiation. Aller shows that a star at 29,600 degrees Kelvin has a greater absorption coefficient for red light than it has for blue light (40, p. 186). Thus the blue radiation from the underwater spark would be emitted from plasma layers which are on the average somewhat deeper below the channel surface, and hence would correspond to a somewhat higher temperature.

Internal Temperature of the Underwater Spark

The spark temperature measurements which have been described have yielded essentially the surface temperature. Without doubt the internal temperatures are higher, but probably not by a very great factor. This conclusion follows from several considerations. In spite of a diligent search for a filamentary central hot core in the spark channel, none has been found. Such a constricted core could arise because of the pinch effect. The absence of this central core is further indicated by the small calculated central pinch pressure as compared to the average overall pressure of the spark channel. As a result the density of current distribution across the channel cross section is believed to be fairly constant so that power is supplied

approximately uniformly throughout the channel volume. Since most of this energy is stored in the plasma, the amount by which the gas is heated in any small volume does not vary appreciably across the cross section. Also, the generation of the shock wave is the major power loss from the spark channel during the time that current flows, and since all volume elements in the channel would expand uniformly, the shock-wave energy is uniformly abstracted from the channel without the necessity of being transferred to the channel walls by thermal conduction due to a temperature gradient. The thermal conductivity of the spark plasma is calculated later in this dissertation. In order to supply the energy at the spark channel wall necessary to convert liquid water to plasma at the required rate, a central temperature of the order of three million degrees Kelvin would be required. This temperature is unrealistically high, and not necessary, since wall recombination of plasma ions will be found to be more than ample to supply the induction energy of the incoming water.

A further indication that the plasma temperature does not vary widely across the channel cross section is the insensitivity of the major spark parameters to the ratio of channel cross sectional area to lateral area. No matter how ruthlessly the channel is flattened by being placed between two closely spaced parallel surfaces, the light output, intrinsic brightness, peak current, and current damping are not changed to any great degree. One would not expect this behavior if the spark channel had an extremely hot core.

Even if the spark channel should be found to have a significantly greater central temperature compared to the surface temperature, the channel energy balance to be described later is not appreciably affected. It will be indicated in the energy balance study that the density

of energy storage in the spark plasma is roughly independent of temperature over a range at least as wide as from 30,000 degrees to 200,000 degrees Kelvin. Therefore, the energy stored in the spark channel depends primarily only on the channel size and plasma pressure.

CHAPTER VI

THE ENERGY BALANCE

The fundamental spark quantities, the current, the channel diameter, the channel pressure, and the surface temperature have been determined as functions of time. These quantities, together with the equivalent circuit of the discharge circuit, permit the calculation of an energy balance. The total energy which has been transferred to the spark channel from the discharge circuit at any given instant of time may be computed purely as a circuit problem. From this energy one then subtracts the total energy which has, until the selected instant, been abstracted from the spark channel by mechanical work output (the shock-wave generation), radiation, and thermal conduction. It should be noted here that energy utilized in heating, dissociating, and ionizing additional water molecules at the channel surface should not be subtracted, since this energy remains within the spark channel. The result of this analytical procedure is the amount of energy actually resident within the spark channel at the selected instant of time.

The second stage of the energy balance is a determination of the amount of energy within the spark channel at the desired instant by use of the channel pressure, temperature, Saha's equation, and the equation of state of the discharge plasma. This gives the energy which has been stored in ionization, dissociation, excitation, and random kinetic energy of the various constituent particles of the spark channel. The resulting stored energy may be compared with that

previously obtained as mentioned in the preceding paragraph. Agreement between these two values of stored energy indicates that an accounting for all the energy put into the spark channel has been made. In succeeding paragraphs a detailed description is given of the procedure which was followed to obtain the energy balance of the underwater spark as outlined above.

Circuit Input Energy to the Underwater Spark

The first steps in calculating the energy balance are most readily followed by reference to Table II. Column 1 gives the times during the spark cycle which were selected for calculation. Intervals of one-quarter microsecond were selected for the first four microseconds, and intervals of one-half microsecond were selected for the next four microseconds. An additional entry at the current maximum, 1.9 microseconds, is also included. This range of eight microseconds after current began flowing encompasses the interesting and most important part of the spark cycle. The data taken during the first one-quarter microsecond after current initiation are not reliable or particularly significant because of sensitivity to variations of triggering and initiating of the oscilloscope sweep. This does not imply, however, that a detailed study of the very early stages of the underwater spark would not be fruitful. A study could be made of the spark characteristics during the first half-microsecond utilizing faster sweeps and different trigger arrangements. One would then be concerned with events taking place in time intervals of the order of hundredths of a microsecond.

Column 2 is the spark current, obtained by scaling the oscillogram of voltage developed by the current shunt (Fig. 37). Column 3 is the

TABLE II (A)

CIRCUIT ENERGY BALANCE

1	2	3	4	5	6
TIME	CURRENT	$\frac{di}{dt}$	$\int_0^t i\,dt$	CAPACITOR VOLTAGE	INSTANTANEOUS CAPACITOR POWER
μ sec	amperes	$\frac{\text{amperes}}{\text{second}}$	coulombs	kilovolts	megawatts
		($\times 10^9$)	($\times 10^{-3}$)		
0	0	52.2	0	25.00	0
1/4	13,700	58.0	1.70	24.71	338
1/2	31,000	65.4	7.20	23.76	736
3/4	46,600	59.8	16.9	22.08	1030
1	58,700	49.6	29.9	19.84	1164
1 1/4	70,100	40.0	46.1	17.05	1196
1 1/2	78,300	27.4	64.7	13.96	1094
1 3/4	83,400	13.5	84.9	10.37	864
1.9	85,000	0	97.5	8.19	696
2	84,500	-5.16	106	6.70	566
2 1/4	81,500	-13.8	127	3.10	252
2 1/2	76,900	-23.8	147	-0.28	-21.6
2 3/4	69,000	-37.6	165	-3.40	-234
3	57,300	-48.4	181	-6.20	-356
3 1/4	44,700	-58.0	194	-8.40	-376
3 1/2	29,800	-59.8	203	-10.00	-298
3 3/4	15,450	-53.4	209	-11.00	-170
4	3,090	-49.6	211	-11.40	-35.2
4 1/2	-19,050	-39.2	207	-10.60	+202
5	-34,600	-23.8	194	-8.40	291
5 1/2	-42,900	-10.6	174	-5.00	214
6	-43,600	+6.50	152	-1.30	56.6
6 1/2	-38,400	15.1	132	+2.30	-88.4
7	-27,000	27.6	115	5.10	-138
7 1/2	-10,420	37.6	106	6.75	-70.5
8	+7,820	30.8	105	6.81	+53.2

TABLE II (B)

CIRCUIT ENERGY BALANCE

1	7	8	9	10	11
	INSTANTANEOUS POWER			CUMULATIVE ENERGY INTO SPARK	
TIME	CIRCUIT LOSS	POWER TO INDUCTANCE	SPARK POWER		CAPACITOR ENERGY CONTENT
μ sec	megawatts	megawatts	megawatts	joules	joules
0	0	0	0	0	1810
1/4	7.9	206	124	19	1770
1/2	40.5	527	168	54	1640
3/4	92.0	725	213	102	1420
1	145	757	262	158	1140
1 1/4	207	756	233	220	844
1 1/2	258	558	278	286	566
1 3/4	294	293	277	359	311
1.9	305	0	391	413	194
2	301	-113	378	451	130
2 1/4	280	-292	264	528	27.8
2 1/2	250	-475	203	588	0.23
2 3/4	201	-674	239	644	33.5
3	139	-720	225	699	112
3 1/4	84.4	-675	214	755	204
3 1/2	37.5	-464	128	809	290
3 3/4	10.1	-214	34	835	351
4	4.0	- 39.8	1/2	838	376
4 1/2	15.4	194	-7	837	326
5	50.5	214	26	839	204
5 1/2	77.9	118	18	851	72.6
6	80.1	-73.6	50	868	4.9
6 1/2	62.1	-151	1/2	878	15.4
7	30.8	-194	25	886	75.5
7 1/2	4.6	-102	27	899	132
8	2.6	+ 62.5	-12	902	134

TABLE II (C)

CIRCUIT ENERGY BALANCE

1	12	13	14	15
TIME	INDUCTANCE ENERGY	ENERGY TO RESISTANCE	TOTAL ENERGY	ERROR
μ sec	joules	joules	joules	joules
0	0	0	1810	0
1/4	24	1	1814	+4
1/2	125	7	1826	+16
3/4	283	23	1828	+18
1	446	53	1797	-13
1 1/4	640	97	1801	- 9
1 1/2	797	155	1804	- 6
1 3/4	905	225	1800	-10
1.9	940	270	1817	+ 7
2	930	300	1811	+ 1
2 1/4	864	373	1793	-17
2 1/2	769	440	1797	-13
2 3/4	619	496	1792	-17.5
3	427	539	1777	-33
3 1/4	260	567	1786	-24
3 1/2	116	582	1796	-13.5
3 3/4	31	587	1804	- 5.5
4	1	589	1804	- 6
4 1/2	47	591	1801	- 9
5	156	607	1806	- 3.5
5 1/2	240	640	1803	- 6.5
6	247	681	1801	- 9
6 1/2	192	717	1803	- 7
7	95	741	1797	-12.5
7 1/2	14	749	1794	-16
8	8	750	1794	-16

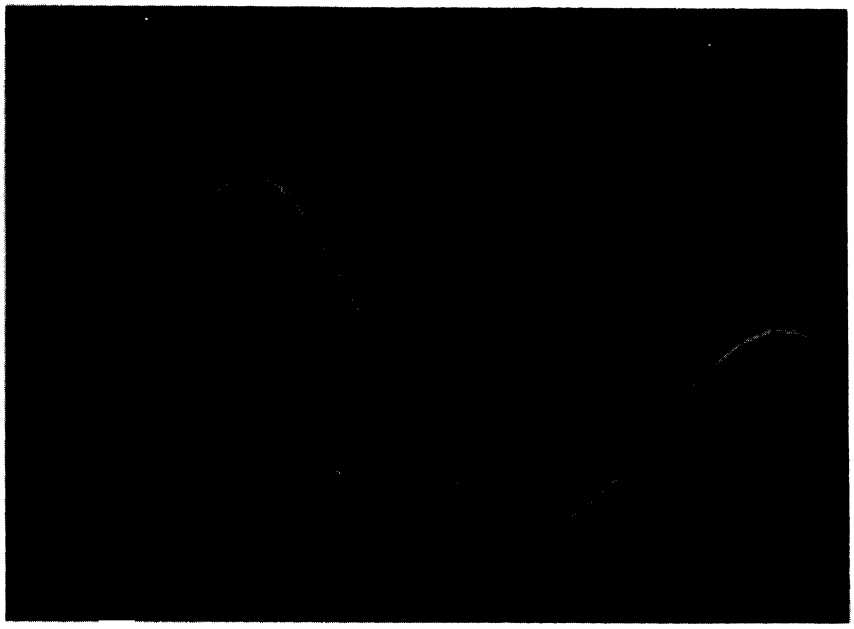

FIG. 37 OSCILLOGRAM OF SPARK CURRENT

SCALE FACTORS:

VERTICAL— 200 VOLTS PER DIV.

HORIZONTAL— 1 MICROSEC. PER DIV.

time rate of change of current, obtained by plotting the current as a function of time and measuring the slope of the curve. Column 4 is the integral of the current from the instant of current initiation to the selected instant of time. It is thus the total charge transferred, and it is obtained by graphically integrating the current curve mentioned above. Column 5, the capacitor voltage, is obtained by subtracting from 25 kilovolts the total change in capacitor voltage which is computed from total charge transferred divided by capacity. Columns 6 to 9 give various instantaneous powers. The capacitor power is the instantaneous power supplied to the discharge circuit, given by capacitor voltage times current. The power dissipated as circuit losses is given by i^2R, where R is the effective total series resistance of the

circuit including the current shunt. The power to the circuit inductance is obtained from $iL\frac{di}{dt}$. If the entries in Columns 7 and 8 are algebraically subtracted from the entry in Column 6, the power being supplied to the underwater spark is obtained, as entered in Column 9 and plotted in Fig. 38.

Columns 10 through 15 are various energy quantities. Column 10 is the total energy which has been supplied to the spark up until the selected instant of time. It is obtained by graphical integration of the spark power curve. Column 11 is the amount of energy remaining in the capacitor, $1/2\ CV^2$. Column 12 is the energy stored in the magnetic field surrounding the discharge circuit, $1/2\ LI^2$. Column 13 is the total energy which has been dissipated up until the selected instant as circuit losses, obtained by graphical integration of the circuit power-loss curve. Column 14 is obtained by adding the entries in Columns 10 to 13. If the accuracy of the analysis were perfect, this column would read 1810 joules, the original stored energy, at all instants of time. Column 15 presents the deviation of the Column 14 entries from 1810 joules, and thus it represents the error, in joules, of the entire circuit analysis. The greatest error is found to be 33 joules out of 1810, or 1.82 percent.

This excellent agreement, which holds throughout the entire time interval being considered, serves to confirm the reliability of the measurements. If an erroneous procedure were involved in the analysis, one would expect the possibility of agreement at one instant of time, with a systematically varying error at earlier and later times. Thus it is satisfactory to consider that we have available, in Column 10, the energy which has been transferred to the spark as a function of

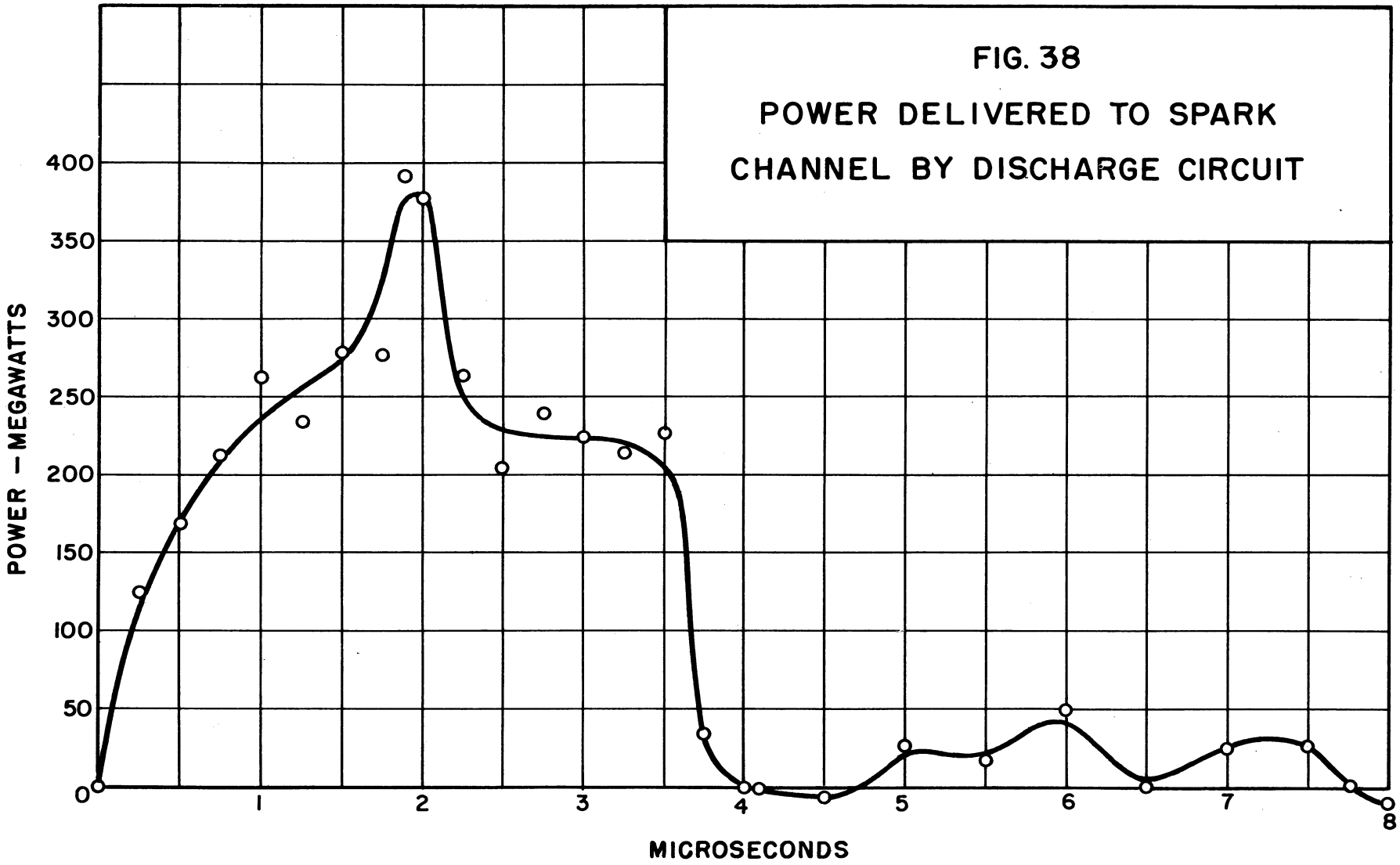
FIG. 38
POWER DELIVERED TO SPARK
CHANNEL BY DISCHARGE CIRCUIT
POWER – MEGAWATTS
400
350
300
250
200
150
100
50
0
1
2
3
4
5
6
7
8
MICROSECONDS

time. It should be noted that these results do not involve any assumptions as to the nature of the circuit element (the spark) which is connected between the spark electrodes. It is purely a circuit problem, and it would be a valid procedure no matter what might be connected between the electrodes. Also, the transfer to the spark channel of 902 joules out of a stored energy of 1810 joules represents an exceptionally high efficiency of energy transfer, much higher than has been reliably reported previously.

Energy Losses from the Underwater Spark

The next step in the energy balance calculation, determination of the energy losses from the spark channel, may be followed by reference to Table III. Column 1, as before, presents the selected times for which calculations are made. In Column 2 are presented the spark-channel diameters calculated from the equation of spark-channel growth, which in turn is based on the channel diameters scaled from the enlarged Kerr cell photographs. In Columns 3 to 6 are channel cross sectional area, channel lateral area (cylindrical surface area), channel volume, and wall velocity. These geometric quantities follow from the channel-diameter data and a constant spark length of 1.5 centimeters. The external pressure exerted by the spark channel is presented in Column 7. This pressure is calculated from the shock-wave relation, Equation 4.11, derived earlier. The mechanical power output of the spark channel is now calculable, being the product of external pressure, lateral area, and wall velocity. The results are presented in Column 9 and plotted in Fig. 39. As will be evident shortly, the power supplied to the shock wave is the most important power loss from the channel during the early stages of the spark, and

TABLE III (A)

SPARK ENERGY BALANCE

1	2	3	4	5	6
TIME	CHANNEL DIAMETER	CHANNEL CROSS-SECTION AREA	CHANNEL LATERAL AREA	CHANNEL VOLUME	CHANNEL WALL VELOCITY
μ sec	meters	square meters	square meters	cubic meters	meters / second
	($\times 10^{-3}$)	($\times 10^{-6}$)	($\times 10^{-4}$)	($\times 10^{-9}$)	
0	0	0	0	0	∞
1/4	.813	.52	.382	7.8	913
1/2	1.25	1.22	.588	18.4	657
3/4	1.55	1.88	.730	28.3	541
1	1.80	2.54	.847	38.1	471
1 1/4	2.02	3.20	.952	48.0	423
1 1/2	2.22	3.80	1.05	57.0	388
1 3/4	2.41	4.55	1.14	68.3	361
1.9	2.51	4.95	1.18	74.3	348
2	2.58	5.22	1.22	78.3	338
2 1/4	2.75	5.93	1.30	89.0	320
2 1/2	2.91	6.64	1.37	99.6	305
2 3/4	3.05	7.30	1.44	109.5	291
3	3.20	8.04	1.51	121	280
3 1/4	3.34	8.77	1.57	132	268
3 1/2	3.46	9.40	1.63	141	259
3 3/4	3.60	10.2	1.70	153	251
4	3.72	10.8	1.75	163	243
4 1/2	3.96	12.3	1.87	184	230
5	4.17	13.6	1.96	204	219
5 1/2	4.39	15.1	2.07	227	208
6	4.60	16.6	2.16	249	200
6 1/2	4.79	18.0	2.26	270	193
7	4.98	19.5	2.35	292	186
7 1/2	5.17	21.0	2.43	315	180
8	5.34	22.4	2.52	336	174

TABLE III (B)

SPARK ENERGY BALANCE

1	7	8	9	10	11
TIME	CALCULATED EXTERNAL PRESSURE	AVERAGE PINCH PRESSURE	SHOCK-WAVE POWER	SHOCK-WAVE ENERGY	CHANNEL TEMPERATURE
μ sec	atm	atm	megawatts	joules	degrees Kelvin
0	∞	—	∞	—	——
1/4	32,300	181	112.6	27.5	23,000
1/2	19,400	390	75.0	44.5	25,450
3/4	14,200	—	56.1	65.6	26,700
1	11,600	676	46.2	78.4	27,650
1 1/4	9960	—	40.1	89.2	28,500
1 1/2	8800	—	35.6	98.7	29,150
1 3/4	7900	—	32.4	107	29,750
1.9	7600	735	31.2	112	29,950
2	7300	—	30.0	115	30,000
2 1/4	6810	—	28.2	122	30,100
2 1/2	6320	—	26.4	129	29,950
2 3/4	6040	—	25.2	135	29,850
3	5640	204	23.8	142	29,600
3 1/4	5350	—	22.5	147	29,150
3 1/2	5150	—	21.8	153	28,700
3 3/4	4850	—	20.6	158	28,300
4	4700	1/2	20.0	163	28,000
4 1/2	4410	—	18.9	173	27,700
5	4070	44	17.5	182	27,550
5 1/2	3870	—	16.7	190	27,500
6	3720	57	16.1	198	27,500
6 1/2	3530	—	15.4	206	27,000
7	3380	—	14.8	214	26,500
7 1/2	3280	—	14.4	221	26,150
8	3080	1 1/3	13.5	228	26,000

TABLE III (C)

SPARK ENERGY BALANCE

1	12	13	14	15
TIME	RADIANT POWER	RADIANT ENERGY	CHANNEL ENERGY (CURVE A, FIG. 42)	PLASMA CONDUCTIVITY (EXPERIMENTAL)
μ sec	megawatts	joules	joules	$\frac{\text{mhos}}{\text{meter}}$
0	0	0	0	-
1/4	.346	.075	-8.6	43,700
1/2	1.41	.300	+9.6	70,000
3/4	2.10	.714	35.7	81,000
1	2.84	1.32	78.4	77,700
1 1/4	3.56	2.12	128.7	99,000
1 1/2	4.30	3.11	184	87,000
1 3/4	5.10	4.30	247	82,600
1.9	5.42	5.10	296	56,000
2	5.58	5.64	330	54,300
2 1/4	6.06	7.10	399	63,500
2 1/2	6.29	8.65	450	65,600
2 3/4	6.48	10.3	498	40,900
3	6.59	11.9	545	27,200
3 1/4	6.42	13.5	594	15,900
3 1/2	6.28	15.1	641	11,100
3 3/4	6.15	16.7	660	10,300
4	6.06	18.2	656	
4 1/2	6.24	21.2	643	inaccurate region
5	6.40	24.4	633	
5 1/2	6.70	27.6	633	
6	7.00	31.2	638	
6 1/2	6.83	34.6	637	
7	6.55	38.0	634	
7 1/2	6.42	41.2	637	
8	6.52	44.5	629	

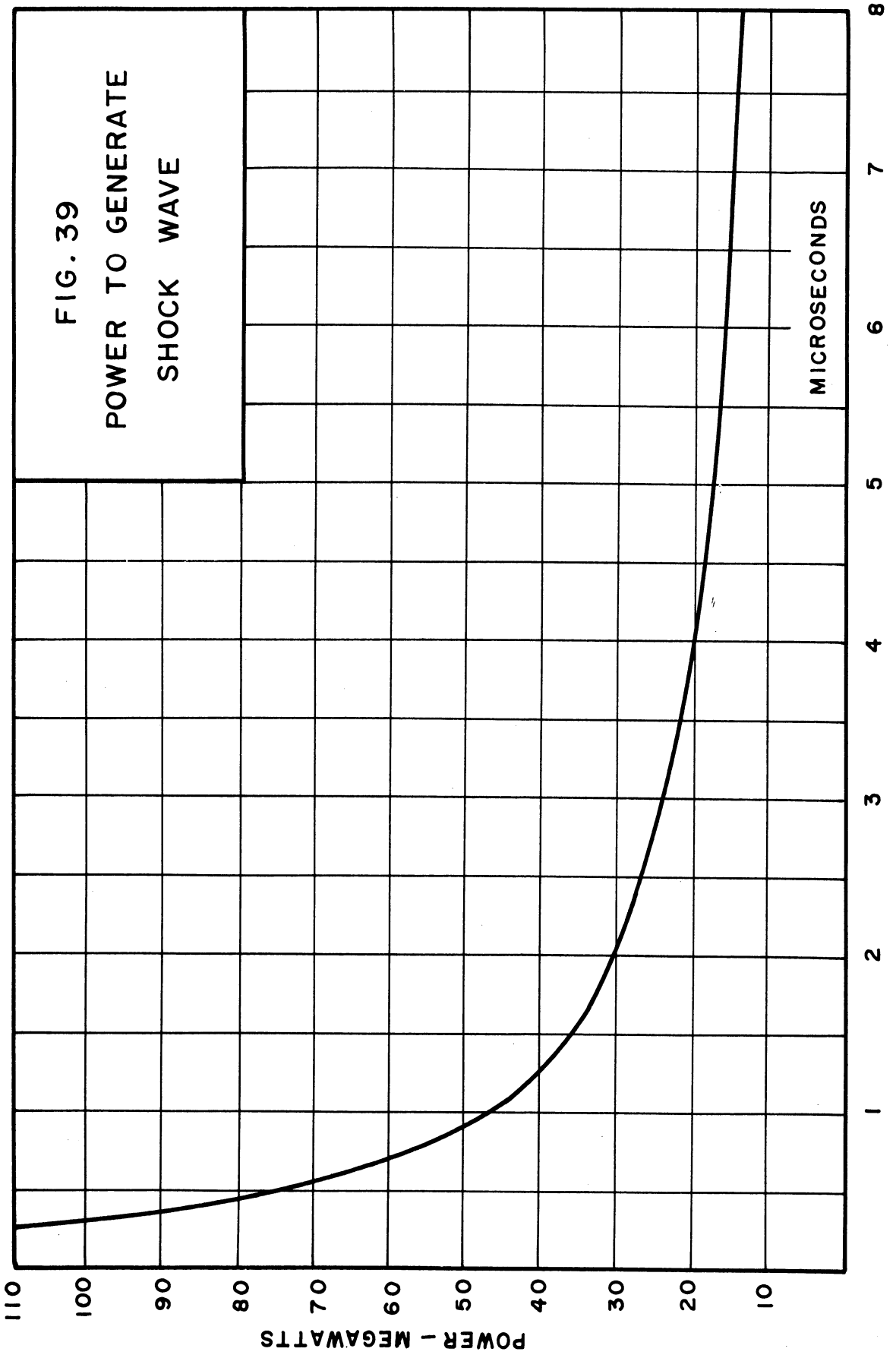
FIG. 39
POWER TO GENERATE
SHOCK WAVE
MICROSECONDS
1
2
3
4
5
6
7
8
POWER - MEGAWATTS
10
20
30
40
50
60
70
80
90
100
110

it remains twice as great as the radiation loss at eight microseconds after spark initiation. Column 10 is the graphical integral of the shock-wave power; thus there is available, at any selected time, the total energy which has been employed in shock-wave generation.

In Column 11 is presented the spark-channel surface temperature as obtained by averaging the two independent measurements at 6450 Angstroms and 4190 Angstroms (See Table I). Column 12 contains the rate of energy loss from the spark due to rediation, calculated by means of the Stefan-Boltzmann law using the temperature in Column 11. The Stefan-Boltzmann law is

$$J = \sigma T^4 \tag{6.1}$$

where

J is the total intensity of radiation of all wavelengths from a blackbody surface,

σ equals 5.67×10^{-8} watts per square meter per degree Kelvin to the fourth power, and

T is the temperature in degrees Kelvin.

In this calculation the spark-channel surface was considered to be a diffuse blackbody radiator. It was further assumed that radiant energy of all wavelengths leaves the channel and is absorbed within, or transmitted by, the surrounding water. This assumption was made because of the absence of data on the spectral reflectivity of a water surface. The assumption implies that no radiant energy is reflected back into the channel at the channel surface. The curve of radiant power is given in Fig. 40. The integral of the radiant power is given in Column 13. Finally, the net amount of energy stored in the spark

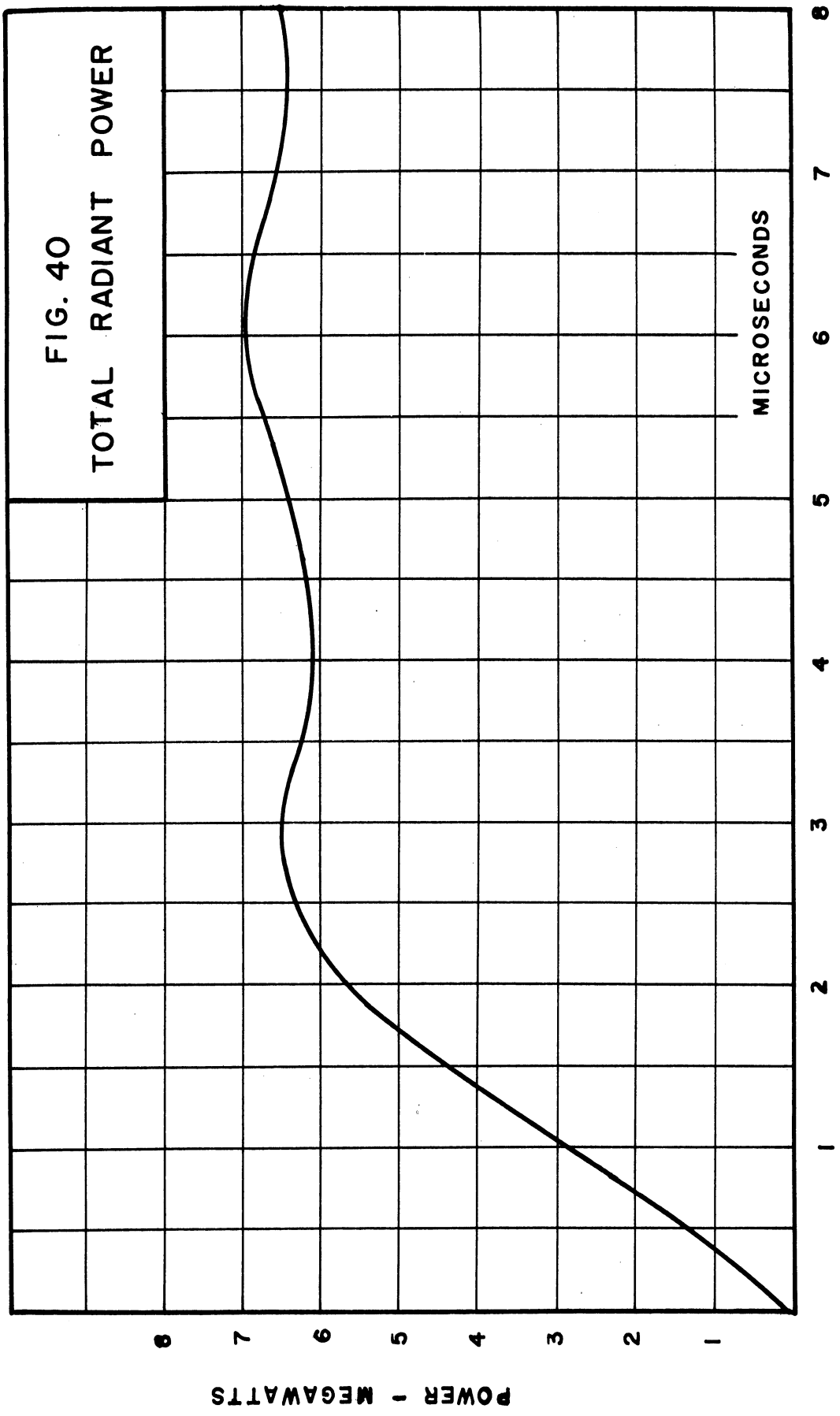
FIG. 40
TOTAL RADIANT POWER
MICROSECONDS
1
2
3
4
5
6
7
8
POWER - MEGAWATTS
1
2
3
4
5
6
7
8

channel, as a function of time, is given in Column 14. It is computed as spark input energy, Column 10 of Table II, minus the two major energy losses, shock-wave generation and radiation as given in Columns 10 and 13 of Table III.

Thermal conduction from the underwater spark channel appears to be insignificant by comparison to the mechanical and radiant energy losses. The evaluation of the conduction loss is a transient heat problem, since on a microsecond time scale the temperatures in the water adjacent to the channel would not achieve equilibrium values. The rigorous mathematical evaluation of this loss is difficult because of its transient nature and because of the cylindrical geometry. The size of the cylinder and its temperature are both functions of time. Churchill presents a solution to the problem of transient flow of heat in a planar case (41, p. 110). Use of this relation, together with rather conservative approximations, leads to the conclusion that at current maximum, the thermal conduction loss is less than three megawatts and the total thermal energy loss up to that time is ten joules. If this result is only approximately correct, then neglecting the loss by thermal conduction will not introduce appreciable error in the spark energy balance. Further, most of this loss is to the water immediately adjacent to the spark channel. When this water is finally inducted into the channel by vaporization at the channel surface, the energy is reintroduced into the channel and is therefore not lost.

Particle Balance

The first part of the energy balance has now been completed. The second part of the calculation consists of determining the amount of

energy which the constituent particles of the spark channel would store at the experimentally determined pressure and temperature. The energy is stored in the spark channel in several ways. The water molecules constituting the channel gas are heated from room temperature, dissociated, excited, ionized, and the resulting product particles are given the random kinetic energy associated with the channel temperature. The means for determining the degrees of dissociation, excitation, and ionization, and consequently the stored energy, are provided by the experimental temperature, the calculated pressure, Saha's ionization equation (which incidentally includes the Boltzmann relation), a "Saha-like" dissociation relation, and an equation of state relating the pressure, temperature, and particle density of the gaseous sytem. The calculation is essentially a particle balance.

By use of the appropriate gas law and the temperature and pressure, one first determines the total number density of all types of particles in the spark channel. The ideal gas law will be used initially in the present calculations; subsequently it will be concluded that the spark-channel gas is nonideal because of Coulombic interparticle forces. It will also be assumed that the gas temperature is constant and equal to the surface temperature throughout the channel volume. It will be shown later that this assumption is justified for the present calculation, since the amount of energy stored in the spark channel is not appreciably altered by a wide variation of temperature.

The types of particles which could possibly be found in the spark channel are water molecules, hydrogen molecules, oxygen molecules, hydrogen atoms, oxygen atoms, hydrogen ions (protons), singly or multiply ionized oxygen, and electrons. There also could be neutral,

singly ionized, or multiply ionized tungsten and copper from the initiating wire and the electrodes. It will be considered that negligible ozone is present in the spark channel since this compound is not produced appreciably in sparks and is very unstable at temperatures above 1000 degrees centigrade (42, pp. 13, 37). Hydroxyl (OH) groups also would be present in negligible amounts since the dissociation energy is only about four electron volts. Negative hydrogen ions formed by electron attachment will be neglected since Linder reports that they are not important in glow discharges in water vapor (43). Given the amount of tungsten and copper present in the channel, and the total pressure and temperature, one can in principle set up a sufficient number of simultaneous algebraic equations to be able to solve for the number densities of all particle types. Most of the equations will be nonlinear, resulting in a very intractable set of equations to solve. It will turn out that some particle types will be present in the channel in such small numbers that their presence may be neglected. This reduces the complexity of the equations to a reasonable level.

Copper from the spark electrodes will be eliminated from consideration because the spark does not last long enough for appreciable numbers to migrate into the channel. For example, at current maximum, the final particle balance will lead to a mobility of 2.4×10^{-6} meters per second per volt per meter. This value is an upper limit to the mobility of the copper since it is based on the simplfied kinetic theory value neglecting interparticle fields. Taking an upper limit to the spark-channel electrical gradient of about 3.3×10^{5} volts per meter, and considering that the spark lifetime does not

exceed 25 microseconds, one finds the maximum distance of migration of copper into the channel is 2×10^{-5} meters. This is very small compared to the spark-channel length of 1.5×10^{-2} meters. Tungsten from the initiating wire will also be eliminated from consideration, since the final results of the calculations will show that the effect of tungsten is negligible even though it has a lower ionization potential than oxygen or hydrogen and hence is more highly ionized. The calculations will also show that there is no appreciable multiple ionization of the oxygen atoms, and so only neutral and singly ionized oxygen need be considered.

The degree of dissociation of water, oxygen, and hydrogen molecules will be analyzed using a relation developed by Gibson and Heitler from quantum statistics (44). This equation, recently considered by Aller (40, p. 91), gives the relative abundances of molecules and atoms at thermal equilibrium in a reversible reaction of the type

$$A + B \rightleftharpoons AB \tag{6.2}$$

The relation is similar to Saha's ionization equation, except that there are additional terms which arise as a result of internal degrees of freedom of the molecule. The relation is

$$\frac{P_A P_B}{P_{AB}} = \frac{g_A g_B}{g_{AB}} \left[\frac{2\pi M kT}{h^2} \right]^{3/2} \frac{h^2}{8\pi^2 I} \left(1 - e^{-S}\right) e^{-\frac{D}{kT}} \tag{6.3}$$

where

$S = \frac{h\nu}{kT}$,

P_A, P_B, P_{AB} - partial pressures of the A, B, and AB components,

g_A, g_B, g_{AB} - statistical weights of the type A, B, and AB particles,

M - reduced mass, $M = \frac{M_A M_B}{M_A + M_B}$,

k - the Boltzmann constant,

T - absolute temperature (^{o}K),

h - Planck's constant,

I - moment of inertia of the type AB molecule,

ν - fundamental vibrational frequency of the type AB molecule, and

D - dissociation energy of the type AB molecule (joules).

Table IV contains the fundamental molecular constants which were used for calculations with Equation 6.3 (45, p. 362). While Equation 6.3 is strictly applicable only to the dissociation of diatomic molecules,

TABLE IV

MOLECULAR CONSTANTS

MOLECULE	DISSOCIATION ENERGY joules	CHARACTERISTIC FREQUENCY cycles per second	MOMENT OF INERTIA kilogram square meters
O_2	8.15×10^{-19}	4.73×10^{13}	19.2×10^{-47}
H_2	7.04×10^{-19}	12.79×10^{13}	0.467×10^{-47}
H_2O	(4.0×10^{-19})[1]	4.5×10^{13} to 11.1×10^{13}	1×10^{-47} to 3×10^{-47}

[1](Taken from Reference 43)

we will apply it here also to the dissociation of the triatomic water molecule and recognize that the results are an approximation in this case. The values of the moment of inertia and characteristic vibrational frequency of water are different in different directions, hence a range of values is given. A further approximation used in these calculations is to assume that the ratio of statistical weights in Equation 6.3 is unity. This approximation is frequently made in calculations relating to dissociation and ionization; the departure of the ratio from unity is usually small enough so that its effect is negligible by comparison with the exponential terms in the equation.

The calculation of the degree of dissociation of water at 30,000 degrees Kelvin was carried out by choosing the values of I and ν to obtain the least dissociation; so the calculation provides the minimum value to be expected. Making use of the ideal gas law to convert partial pressure to particle density, one obtains from Equation 6.3

$$\frac{n_{H_2}\, n_{O_2}}{n_{H_2O}} = 3.08 \times 10^{28} \text{ per meter}^3 \qquad (6.4)$$

where n_{H_2}, n_{O_2}, and n_{H_2O} signify the number density of the hydrogen, oxygen, and water molecules respectively. We now assume that the products of dissociation, H_2 and O_2, are not further dissociated, or ionized, or otherwise made unavailable for recombination into H_2O. This is again an assumption which leads to a lower limit of calculated dissociation, since any process which tends to make the dissociation products unavailable for recombination will tend to drive the reaction 6.2 toward the left. Now one has the stoichiometric relation for water,

$$n_{H_2} = 2\, n_{O_2} \qquad (6.5)$$

and it will soon be shown that at t = 1.9 microseconds (current maximum),

$$n_{H_2} + n_{H_2O} = 0.514 \times 10^{27} \text{ per meter}^3 \qquad (6.6)$$

The set of simultaneous Equations 6.4, 6.5, and 6.6 may be solved for n_{H_2O} to give

$$n_{H_2O} = 4.3 \times 10^{24} \text{ per meter}^3 . \qquad (6.7)$$

The total density of all particle types will subsequently be found by use of the channel pressure, temperature, and the ideal gas law. At current maximum the result will be 2.02×10^{27} per cubic meter. It may therefore be seen that at most the fraction of water molecules is very much less than one percent. On this basis the number of water molecules will be assumed negligible.

The same procedure may be applied to the dissociation of oxygen molecules. When this is done, one obtains from Equation 6.3

$$\frac{(n_O)^2}{n_{O_2}} = 0.158 \times 10^{29} \text{ per meter}^3 \qquad (6.8)$$

Subsequent analysis will show that at current maximum,

$$2n_{O_2} + n_O = 0.511 \times 10^{27} \text{ per meter}^3 \qquad (6.9)$$

Solving 6.8 and 6.9 for n_O and n_{O_2} gives

$$n_O = 0.48 \times 10^{27} \text{ per meter}^3 \qquad (6.10)$$

$$n_{O_2} = 0.015 \times 10^{27} \text{ per meter}^3 \qquad (6.11)$$

Thus there are less than three percent as many oxygen molecules as there are oxygen atoms. In the case of hydrogen dissociation, it is only necessary to compare the relative values of D, I, and ν for oxygen

and hydrogen and note the resulting effects produced in Equation 6.3. The conclusion is that the hydrogen will be more dissociated than the oxygen. Thus we may conclude that there is a negligible number of undissociated molecules in the spark channel; the total number present is probably substantially less than two percent of the total number of particles of all types.

The result of eliminating from consideration some of the particle types which have a possibility of being present in the spark channel is to reduce a complicated set of simultaneous equations to a more simple set. The particle types remaining may now be determined by the following particle-balance equations:

$$n_{HI} + n_{HII} + n_{OI} + n_{OII} + n_e = N \tag{6.12}$$

$$n_{HI} + n_{HII} = 2 n_{OI} + 2 n_{OII} \tag{6.13}$$

$$n_{HII} + n_{OII} = n_e \tag{6.14}$$

$$n_{HII} n_e = n_{HI} S_H \tag{6.15}$$

$$n_{OII} n_e = n_{OI} S_O \tag{6.16}$$

The symbols have the following meanings:

N - total density of particles of all types,

n_{HI} - density of neutral hydrogen atoms,

n_{HII} - density of singly ionized hydrogen,

(similarly for oxygen),

n_e - electron density,

S_H - Saha factor for hydrogen, and

S_O - Saha factor for oxygen.

Equations 6.15 and 6.16 are Saha thermal ionization equations, which give the degree of ionization of the hydrogen and oxygen in the spark channel. Each Saha factor is a function of temperature and of the combined energy-level structure of the ion and corresponding atom involved in the equation. A discussion of the origin and interpretation of the Saha equation as well as a derivation is given in Appendix A. For the present, the Saha factor is given by the expression:

$$S = \frac{2\,B'(T)}{B(T)}\left(\frac{2\pi m_e k}{h^2}\right)^{3/2} T^{3/2} e^{-\frac{11{,}600\,V}{T}} \qquad (6.17)$$

The symbols designate the following:

- $B'(T)$ - partition function of the ion (a function of T),
- $B(T)$ - partition function of the atom (also a function of T),
- m_e - mass of the electron, and
- V - ionization potential of the atom (in volts).

The other symbols have the usual meanings.

The partition functions are determined from the energy-level diagram of the appropriate atom or ion. In general, for a quantized atomic system, the partition function is given by

$$B(T) = \sum_i g_i \cdot e^{-\frac{\mathcal{E}_i}{kT}} \qquad (6.18)$$

where g_i are the statistical weights of the energy levels as determined from the spectral terms, and $\mathcal{E}_i$ are the energies of the levels above the ground state in joules. Unfortunately the partition function for an atom or ion is not convergent; the g_i factors in Equation 6.18 in general increase as the principal quantum number (n) increases, but the $\mathcal{E}_i$ are bounded by the ionization potential of the atom or ion. The

problem of deciding how many terms to use in calculating the partition function of an atomic system (there are, of course, an infinite number of energy levels for an atom) is a fundamental problem in the field of atomic physics. There are two methods which have been evolved for deciding how many terms should be used, one due to Urey and Fermi and the other due to Planck (46, p. 574). The method of Urey and Fermi is much the simpler conceptually; it is referred to as the method of excluded volumes. In this method it is assumed that the atom or ion can be excited to a level only as high as that which will make its volume equal to the average volume of space available to the atom or ion. Excitation to a higher level is therefore excluded, since the excitation electron would then more appropriately belong to a nearby atom or ion. A simplified form of this method will be used in the present study to evaluate partition functions and also to decide how many of the atomic or ionic energy levels are available for excitation. It should be noted that the viewpoint just presented implies that a reduced ionization potential should be used in the Saha equations. The amount of reduction of ionization potential thus obtained is not far different from that calculated by Unsold, and discussed by Burhorn, Maecker, and Peters (4).

The neutral hydrogen and oxygen atoms and the oxygen ions in the underwater spark plasma will be excited into energy levels above the ground state so that appreciable energy is stored in excitation. Boltzmann's relation describes the population of the i level as compared to the total population of all levels of the atom as

$$\frac{n_i}{n} = \frac{g_i}{B(T)} e^{-\frac{\varepsilon_i}{kT}} \qquad (6.19)$$

In this equation n_i is the average number of atoms of a given type in the i level, and n is the total number of atoms of that type present. The other symbols have their usual meanings. Thus the simultaneous particle-balance equations, 6.12 through 6.16, are supplemented by a set of relations of type 6.19, one Boltzmann relation being necessary for each excited level in each of the three types of excitable particles present in the spark channel. Fortunately, each Boltzmann relation introduces one new variable, i. e., the population of an excited level, and one new equation into the set of simultaneous particle-balance equations. The result is that 6.12 through 6.16 may be solved simultaneously first, and later one may introduce Boltzmann relations one by one to get the populations of excited levels.

Equations 6.12 through 6.16 will be solved for three selected instants during the spark cycle. The three sets of results, which yield the amounts of energy stored in the spark channel, conform to a simple pattern which will allow interpolation of the amount of energy storage to other moments of time. The particular moments selected are one-half microsecond, 1.9 microseconds (current maximum), and four microseconds (first current zero) after initiation of current. The calculation at current maximum will be presented in detail; only the results will be given for the other times.

The value of N in Equation 6.12 is determined using the ideal gas law and the temperature and average pressure in the spark channel. The effect of pinch force is included as described earlier in this dissertation. The value of N is 2.02×10^{27} particles of all types per cubic meter. The energy levels and spectral term types for calculating partition functions were taken from tables of the National Bureau of

Standards (47). The following were obtained from Equation 6.18 using the method of excluded volumes and a temperature of 29,950 degrees Kelvin.

$$\begin{aligned} &\text{Hydrogen atom:} && B(T) = 2.154 \\ &&& V = 10.6 \text{ volts} \\ &\text{Oxygen atom:} && B(T) = 11.76 \\ &&& V = 10.6 \text{ volts} \\ &\text{Oxygen ion:} && B(T) = 7.67 \\ &&& V = 27.3 \text{ volts} \end{aligned} \tag{6.20}$$

The appropriate Saha factors are then found from 6.17 to be

$$\begin{aligned} S_H &= 0.193 \times 10^{27} \text{ per meter}^3 \\ S_O &= 0.271 \times 10^{27} \text{ per meter}^3 \end{aligned} \tag{6.21}$$

The solutions of the particle-balance equations at the current maximum, taking into account the Boltzmann relations 6.19 to get the degrees of excitation of the various levels, are given on the left side of Table V.

The next step in the determination of the energy in the spark channel is to associate a certain amount of energy with each of the particle types in Table V. This is most conveniently done by constructing a dissociation and ionization table for a single water molecule. This is shown in Table VI. The table presents the energy requirements to dissociate and ionize an isolated water molecule in varying degrees. The conditions presented in any row are independent of the particular sequence of steps selected to reach that stage of dissociation or ionization. The average energy stored in random particle motion is given for the spark temperature at current maximum, 29,950 degrees Kelvin. Also it should be noted that the table lists the ionization potentials for an isolated atom. When the atoms are closely spaced, as in a high pressure plasma, the reduced ionization potentials 6.20 should be used. This was done in the present energy-balance calculation. The right

TABLE V

PARTICLE BALANCE AT 1.9 MICROSECONDS

PARTICLE TYPE	PARTICLE DENSITY per cubic meter	ENERGY PER PARTICLE electron volts	ENERGY DENSITY electron volts per cubic meter
	($\times 10^{26}$)		($\times 10^{27}$)
Neutral hydrogen			
ground state	6.75	7.2	4.86
first excited state	0.52	17.4	0.905
Ionized hydrogen	3.01	17.7	5.34
Neutral oxygen			
ground state	2.48	7.2	1.79
first excited state	0.645	9.2	0.593
second excited state	0.055	11.4	0.063
third excited state	0.061	16.5	0.101
Ionized oxygen			
ground state	0.977	17.7	1.73
first excited state	0.675	21.0	1.42
second excited state	0.210	22.7	0.477
third excited state	0.0092	32.6	0.030
fourth excited state	0.0042	40.8	0.017
Electrons	4.48	3.9	1.907
Total	2.02×10^{27}		19.23×10^{27}

TABLE VI

ENERGY OF DISINTEGRATION OF A WATER MOLECULE
(29,950 °K.)

PRODUCT	ENERGY REQUIRED	TOTAL ENERGY	NUMBER OF PARTICLES	ENERGY PER PARTICLE		
				DISINTEGRATION	KINETIC ENERGY AND VAPORIZATION	TOTAL
	electron volts	electron volts		electron volts	electron volts	electron volts
H_2O (vapor)	0	0	1	0	0.6	0.6
$H_2 + 1/2\ O_2$	2.50	2.50	1 1/2	1.66	4.3	5.9
$H_2 + O$	2.54	5.04	2	2.52	4.2	6.7
$2H + O$	4.36	9.40	3	3.13	4.1	7.2
$H^+ + H + O + e$	13.5	22.9	4	5.75	4.1	9.8
$2H^+ + O + 2e$	13.5	36.4	5	7.28	4.0	11.3
$2H^+ + O^+ + 3e$	13.6	50.0	6	8.33	4.0	12.3
$2H^+ + O^{++} + 4e$	34.9	84.9	7	12.1	4.0	16.0
$2H^+ + O^{+++} + 5e$	54.9	139.8	8	17.5	4.0	21.5
$2H^+ + O^{++++} + 6e$	77.0	216.8	9	24.1	4.0	28.1

side of Table V contains the appropriate amount of energy expended in producing the various particle types, including energy of excitation. The dissociation energy of the water molecule has been equally portioned among the three product particles, two hydrogens and one oxygen. The ionization energy is associated with the corresponding product ion, allocating the resulting electron only its average random kinetic energy. This latter procedure makes it unnecessary to subdivide the number of electrons present into groups according to their origin. When the energy density per particle type, the last column in Table V, is summed over all particle types, the resulting total energy density is 19.2×10^{27} electron volts per cubic meter, or 3.08×10^{9} joules per cubic meter.

We next consider the contribution to the stored energy in the spark channel due to the presence of the tungsten atoms from the initiating wire. This problem, and the one to be considered shortly concerning the amount of doubly ionized oxygen in the spark channel, are treated as perturbations on the solution for dissociation and single ionization of water which has already been obtained. This results in linearization of the Saha equations, and simplifies the solution. The results of the calculations show that the procedure is justified.

The volume of the initiating wire allows one to calculate reliably the total number of tungsten atoms and ions present in the spark channel. The result, using the channel volume at current maximum, leads to a total tungsten density of 0.663×10^{25} atoms and ions per cubic meter. It is assumed that the number of additional electrons provided to the spark channel by ionization of tungsten is negligible compared to the

number already present from ionization of water products. Further, to simplify the calculation, the partition-function ratio is taken as unity. The resulting (linear) set of simultaneous equations is therefore

$$n_{WI} + n_{WII} + n_{WIII} + n_{WIV} + n_{WV} = 0.663 \times 10^{25} \text{ per meter}^3 \quad (6.22)$$

$$\frac{n_{WII}}{n_{WI}} = \frac{S_{I-II}}{n_e} = \frac{S_{I-II}}{0.448 \times 10^{27}} \quad (6.23)$$

$$\frac{n_{WIII}}{n_{WII}} = \frac{S_{II-III}}{n_e} \quad (6.24)$$

$$\frac{n_{WIV}}{n_{WIII}} = \frac{S_{III-IV}}{n_e} \quad (6.25)$$

$$\frac{n_{WV}}{n_{WIV}} = \frac{S_{IV-V}}{n_e} \quad (6.26)$$

The symbols have the following meanings:

n_{WI} - number density of neutral tungsten,

$n_{WII---V}$ - number density of tungsten ions, and

S_{I-II} - Saha factor for 1st ionization of tungsten.

In calculating the Saha factors a temperature of 29,950 degrees Kelvin was used, and the approximate values of the reduced ionization potentials were used in the exponential term.[1]

The solutions to Equations 6.22 to 6.26 are presented in the second column of Table VII. The number of additional electrons supplied

---

[1]The calculated energy stored in ionization of the tungsten is not seriously affected by the amount by which the ionization potential is reduced.

TABLE VII

TUNGSTEN IONIZATION AT 1.9 MICROSECONDS

PARTICLE TYPE	PARTICLE DENSITY per cubic meter ($\times 10^{24}$)	ENERGY PER PARTICLE electron volts	ENERGY DENSITY electron volts per cubic meter ($\times 10^{25}$)
Neutral tungsten	1.45	5.0	0.725
Singly ionized tungsten	3.28	11.3	3.71
Doubly ionized tungsten	1.57	21.6	3.39
Triply ionized tungsten	0.025	40.7	0.102
Quadruply ionized tungsten	0.000013	68.5	0.000089
Electrons (from tungsten)	6.50	4.0	2.60
Total	12.83×10^{24}		10.53×10^{25}

to the spark channel by ionization of tungsten may now be calculated; the result is 0.650×10^{25} per cubic meter. This is small compared to 0.448×10^{27} already present, which justifies the original assumption. The energy per particle in Table VII is based on four electron volts for average kinetic energy, one electron volt for converting the metallic tungsten to vapor, and the reduced ionization potentials mentioned previously. When the total amount of energy stored in ionization of tungsten is summed, the result is 1.69×10^{7} joules per cubic meter. This is about one-half percent of the energy stored by the hydrogen and oxygen originating from the water. The energy stored by the tungsten would be somewhat greater than that calculated above because excitation of the lower energy levels of the tungsten atoms and ions has been neglected. However, even if this factor were taken into account, the conclusion would still remain that negligible energy is stored in the spark channel by the tungsten from the initiating wire

It is advisable at this point to check the assumption of negligible second ionization of the oxygen in the spark channel. The reduced second ionization potential of oxygen corresponding to the particle density in the underwater spark is about 27.8 volts. The Saha factor is found to be 2.68×10^{23} per cubic meter at a temperature of 29,950 degrees Kelvin, assuming unity for the partition-function ratio. The Saha equation is then

$$\frac{n_{OIII}}{n_{OII}} = \frac{2.68 \times 10^{23}}{0.448 \times 10^{27}} = 5.50 \times 10^{-4} \qquad (6.27)$$

Substitute the value of n_{OII} from Table V to get

$$n_{OIII} = 1.03 \times 10^{23} \text{ per cubic meter} \qquad (6.28)$$

This is, of course, completely negligible compared to the densities of other particle types in the spark channel.

The conclusion has now been reached that at the first current maximum, the energy calculated to be stored in dissociation, ionization, excitation, and random kinetic energy in the underwater spark is 3.08×10^9 joules per cubic meter. The entire process, involving Equations 6.12 through 6.16 and 6.19, may now be repeated for any other selected instant of time. This was done for one-half microsecond and for four microseconds after current initiation. The results of these calculations are presented in Tables VIII and IX. The corresponding calculated stored energies are 6.99×10^9 joules per cubic meter at one-half microsecond and 1.82×10^9 joules per cubic meter at four microseconds.

An interesting and useful relationship may now be noted, based on the data in the preceding calculations. By comparing the calculated energy densities to the corresponding channel pressures (modifying the pressures given in Table III by adding the appropriate pinch pressure), one notes that the two quantities are proportional to each other within an accuracy of about 12 percent. The ratio of the two quantities is presented as a function of time in Fig. 41. This relationship was investigated further. The density of energy stored in the products of dissociation and ionization of water was calculated at various pressures and temperatures by use of equations of the type represented by 6.12 through 6.16. The results are presented in Table X. They show that the density of energy storage is almost independent of temperature over a wide range, but that the energy density is approximately directly proportional to pressure. This independence of energy density on the temperature

TABLE VIII

PARTICLE BALANCE AT 1/2 MICROSECOND

PARTICLE TYPE	PARTICLE DENSITY per cubic meter ($\times 10^{26}$)	ENERGY PER PARTICLE electron volts	ENERGY DENSITY electron volts per cubic meter ($\times 10^{27}$)
Neutral hydrogen			
ground state	28.1	6.4	18.0
first excited state	1.66	16.6	2.76
Ionized hydrogen	3.74	17.0	6.35
Neutral oxygen			
ground state	11.2	6.4	7.16
first excited state	2.76	8.4	2.32
second excited state	0.220	10.6	0.232
third excited state	0.214	15.7	0.336
Ionized oxygen			
ground state	1.32	17.0	2.25
first excited state	0.835	20.3	1.69
second excited state	0.248	22.0	0.545
third excited state	0.008	31.9	0.026
fourth excited state	0.0004	40.1	0.002
Electrons	6.15	3.3	2.03
Total	5.65×10^{27}		43.67×10^{27}

TABLE IX

PARTICLE BALANCE AT 4 MICROSECONDS

PARTICLE TYPE	PARTICLE DENSITY per cubic meter ($\times 10^{26}$)	ENERGY PER PARTICLE electron volts	ENERGY DENSITY electron volts per cubic meter ($\times 10^{27}$)
Neutral hydrogen			
ground state	3.86	7.2	2.78
first excited state	0.227	17.4	0.395
Ionized hydrogen	1.85	17.7	3.28
Neutral oxygen			
ground state	1.48	7.2	1.07
first excited state	0.366	9.2	0.336
second excited state	0.029	11.4	0.033
third excited state	0.028	16.5	0.046
Ionized oxygen			
ground state	0.632	17.7	1.12
first excited state	0.398	21.0	0.835
second excited state	0.119	22.7	0.270
third excited state	0.0039	32.6	0.013
fourth excited state	0.0002	40.8	0.0008
Electrons	3.00	3.9	1.17
Total	1.20×10^{27}		11.35×10^{27}

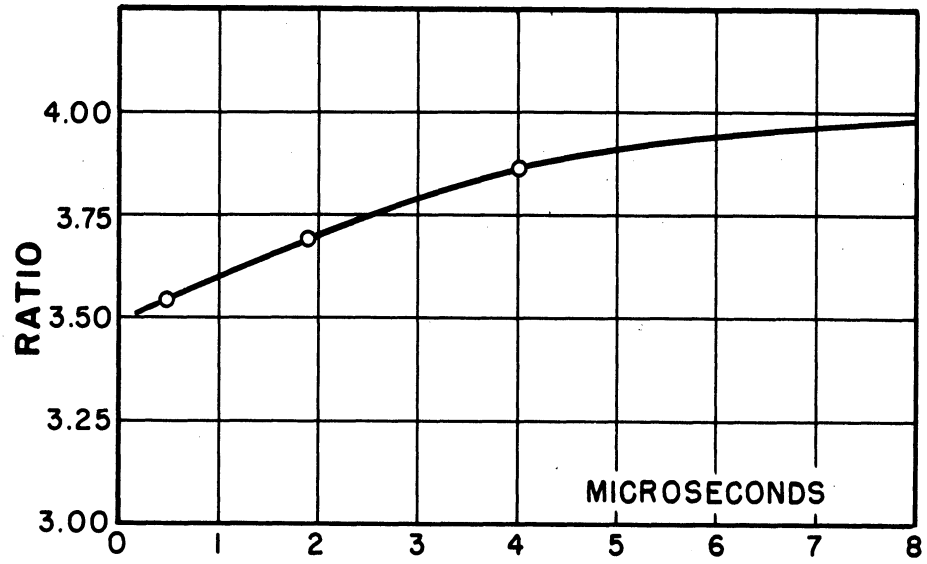

FIG. 41 RATIO OF ENERGY DENSITY TO CHANNEL PRESSURE

TABLE X

STORED ENERGY DENSITY IN WATER

(excitation energy neglected)

PRESSURE atm	TEMPERATURE degrees Kelvin	ENERGY DENSITY joules per cubic meter
4,150	31,500	1.45×10^9
8,300	31,500	2.80×10^9
20,000	31,500	6.38×10^9
8,300	40,000	2.73×10^9
8,300	60,000	2.62×10^9
8,300	200,000	2.78×10^9

Highly ionized tungsten from the initiating wire contributes an additional 0.72×10^9 joules per cubic meter at 200,000 ^{o}K.

may be physically interpreted. For a given pressure, the total particle density N is inversely proportional to temperature, so as the temperature is increased, one has fewer total particles but they are more highly ionized. The two counteracting effects approximately cancel over the ranges of pressure and temperature being considered here. It is for this reason that the exact value of temperature at the center of the spark channel is not necessary for the purposes of determining an energy balance, provided that the temperature is not appreciably higher than 200,000 degrees Kelvin.

The Energy Balance for the Underwater Spark

The entire energy balance may now be summarized graphically; see Fig. 42. Curve A is the energy stored in the spark channel determined by subtracting the shock-wave and radiant energies from the energy input to the spark from the discharge circuit. Curve B is the energy stored in the spark channel calculated from the pressure, temperature, and channel size by use of the particle-balance equations. Points on Curve B other than t = 1/2, 1.9, and 4 microseconds were obtained by using the extrapolated values of energy-density-to-pressure ratio given in Fig. 41. Agreement between Curves A and B would indicate a complete accounting of all the energy which has been supplied to the spark channel at any instant of time.

Channel Magnification

The disagreement of Curves A and B of the energy balance can be qualitatively and semiquantitatively resolved. It is immediately evident that the lack of agreement at times earlier than 1.6 microseconds is principally caused by a determination of pressure which leads to a

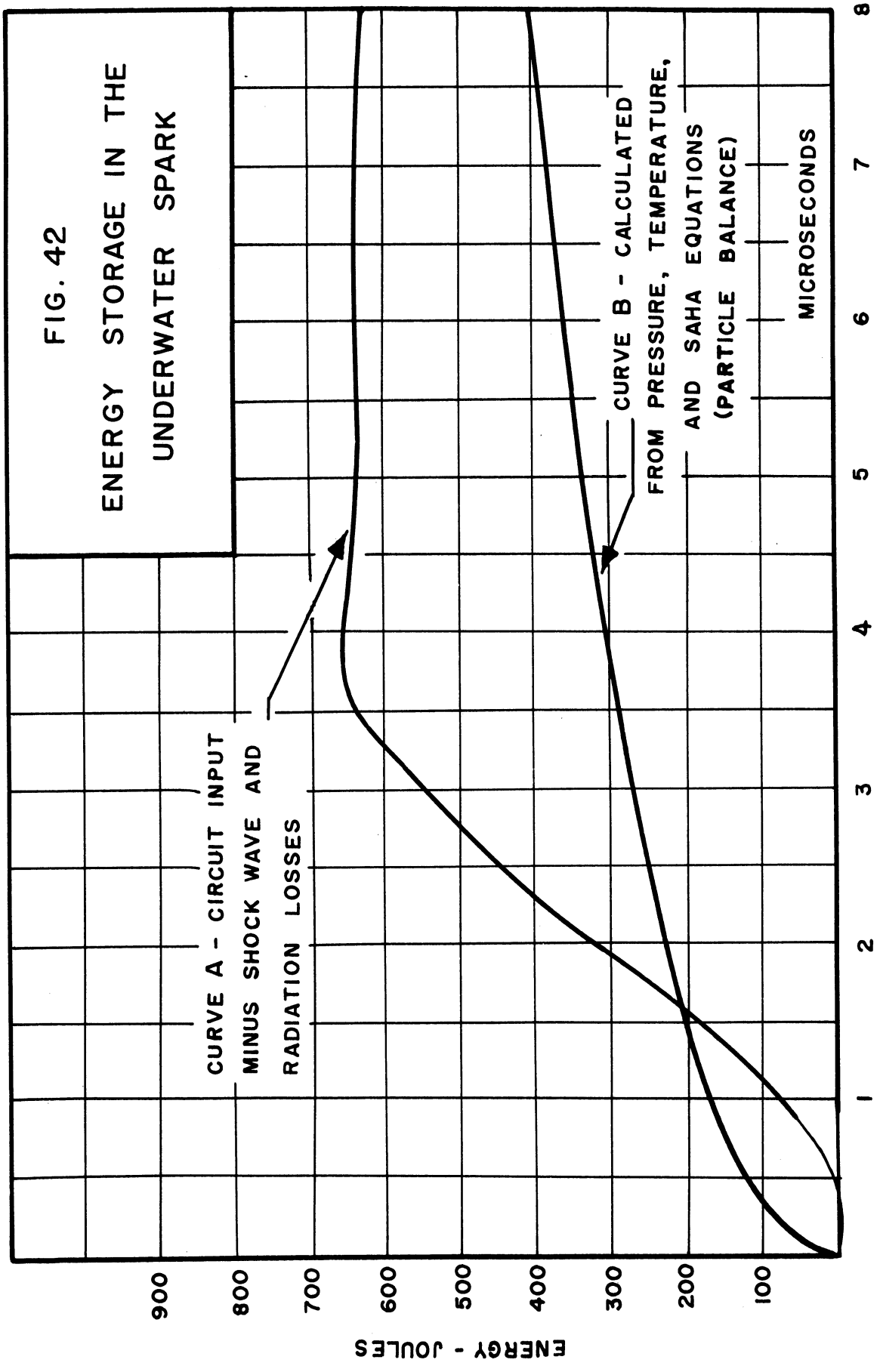
FIG. 42
ENERGY STORAGE IN THE UNDERWATER SPARK
CURVE A - CIRCUIT INPUT MINUS SHOCK WAVE AND RADIATION LOSSES
CURVE B - CALCULATED FROM PRESSURE, TEMPERATURE, AND SAHA EQUATIONS (PARTICLE BALANCE)
ENERGY - JOULES
900
800
700
600
500
400
300
200
100
1
2
3
4
5
6
7
8
MICROSECONDS

value higher than the true value. This is caused by a measured rate of channel expansion which is greater than the true rate. Optical magnification of the channel image by the compressed water of the shock wave and random error of measurement can account for the discrepancy. It will be shown later in this paper that vaporization of liquid water at the channel surface produces no appreciable error.

It was shown in Chapter IV dealing with the shock wave that there is a large pressure gradient in the water adjacent to the channel surface which is caused primarily by geometrical divergence of the water flow lines. At one microsecond this amounts to 21,500,000 atmospheres per meter, and at one-half microsecond it is 58,000,000 atmospheres per meter. These pressure gradients were converted to refractive-index gradients by use of the equation of state of water (Equation 4.1) and the constant ratio of $n - 1$ to ρ. The result is

$$\frac{dn}{dr} = \left(\frac{\rho}{\rho_0}\right)\frac{(n_0-1)}{7(P+B)}\frac{dP}{dr} \qquad (6.29)$$

where n_0 is the index of refraction of water at normal density, ρ_0. The refractive-index gradients at the channel surface were computed to be 87 per meter at one microsecond, and 163 per meter at one-half microsecond. It is relatively easy to derive this useful optical law. The radius of curvature of a light ray traversing a medium in which the index of refraction is a continuous function of position is given at any point by dividing the index of refraction at that point by the component of the vector gradient of the index of refraction which is perpendicular to the direction of the ray. The radius vector is coplanar with the gradient of the index and with the direction of the ray. Using this, we find that the radius of curvature of a ray leaving

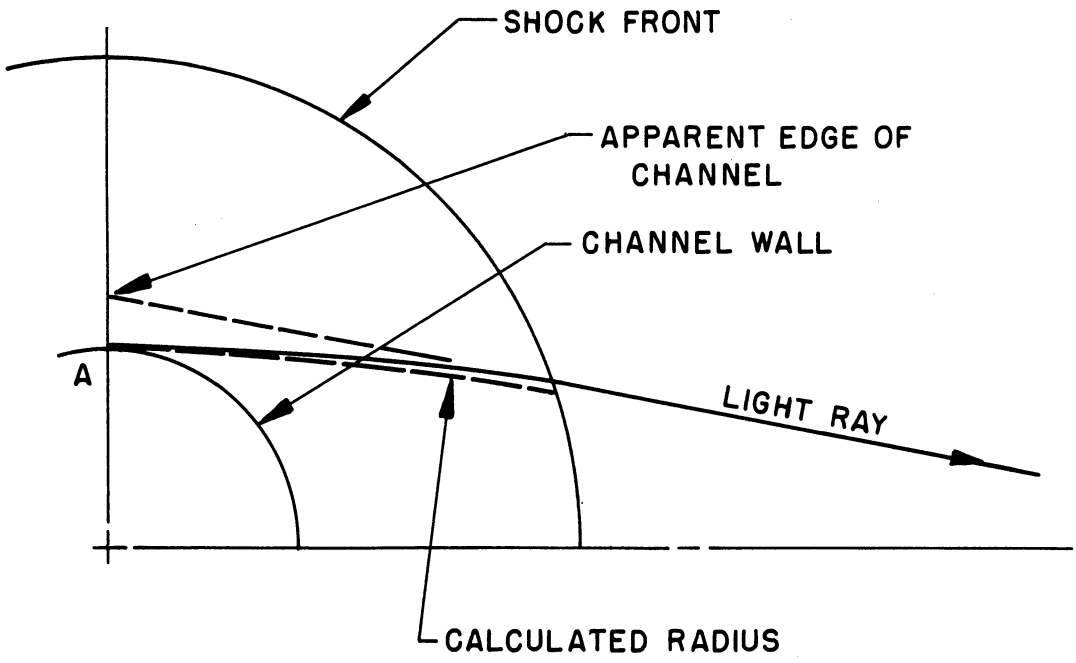

FIG. 43 APPROXIMATE DETERMINATION OF CHANNEL MAGNIFICATION

the channel at a grazing angle in a plane normal to the channel axis is 16 millimeters at one microsecond and is 8.8 millimeters at one-half microsecond. These represent very appreciable amounts of curvature, and their resulting effect in magnifying the channel may be approximately determined as is shown in Fig. 43. This figure is a section through the spark channel normal to the spark axis. The smaller circle represents the channel at a given instant. The concentric outer circle is the estimated position of the shock front at the same instant. A ray leaving the channel tangentially at A starts out along the circle of large radius. Since the pressure gradient decreases with increasing distance from the channel, the ray actually follows a path of continually increasing radius. The pressure variation away from the channel surface is not known, so that an approximation to the

actual path should be used in the figure. As the ray passes through the shock front, it is refracted away from the normal by an amount dependent on the shock-front pressure ratio, which is also unknown. This latter refraction must be appreciable, however, since some of the Kerr cell photographs show clearly the location of the shock front as a consequence of the optical distortion of the image of a background object. By carefully laying out, to scale, diagrams similar to Fig. 43, and making reasonable assumptions concerning the amount of bending produced within the compressed region and at the outer boundary, it was concluded that the channel magnification at one-half and one microsecond should be between 10 and 15 percent. In what follows, the amount of magnification will be taken to be 10 percent, which is representative of the order of magnitude to be expected.

Fig. 44 is a plot of channel size versus time for the first four microseconds. The indicated points are the measured diameters, and the solid curve is the size calculated from Equation 3.4. The measured diameters are first reduced by 10 percent as an approximate compensation for refractive magnification. Until the present, the Kerr cell photographs have been treated as having been taken at the midpoint of the one-quarter-microsecond exposure interval. Considering that the channel image is expanding during this interval, the time of the exposure should more appropriately be taken as the end of the interval as far as channel size is concerned. To take this into consideration, the measured points in Fig. 44 are additionally shifted one-eighth microsecond later in time. The points finally obtained are circumscribed by a rectangle, one side of which represents an uncertainty of about 5 percent in the mechanics of measuring the channel diameter,

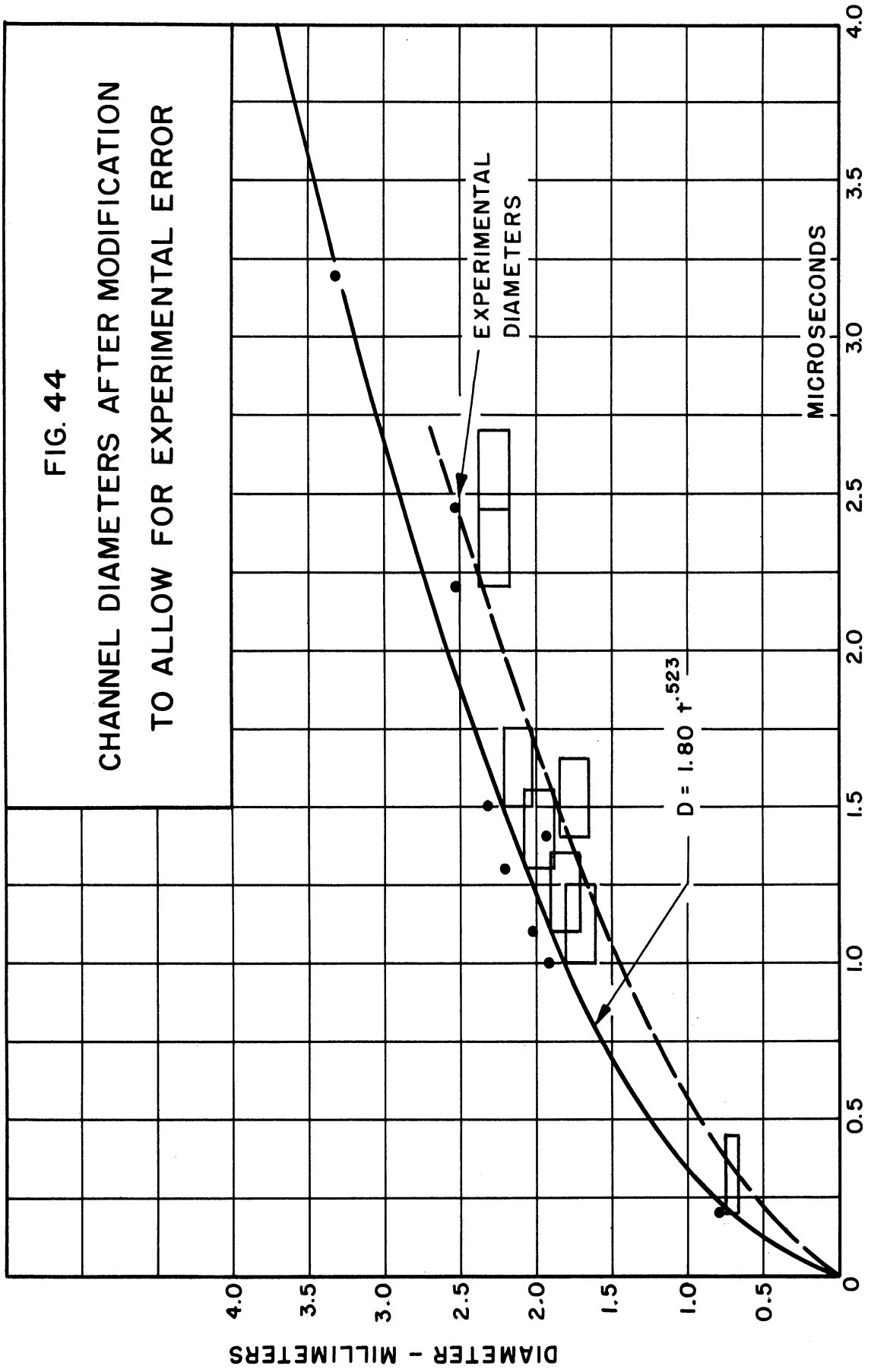
FIG. 44
CHANNEL DIAMETERS AFTER MODIFICATION
TO ALLOW FOR EXPERIMENTAL ERROR
EXPERIMENTAL DIAMETERS
D = 1.80 t^.523
DIAMETER - MILLIMETERS
MICROSECONDS
0
0.5
1.0
1.5
2.0
2.5
3.0
3.5
4.0

the other side allowing for a jitter of plus or minus one-eighth microsecond in the triggering of the Kerr cell. The dotted curve in Fig. 44 gives a lower rate of channel expansion, which is consistent with the experimental channel diameters as modified according to the foregoing considerations.

The effect of using this reduced rate of channel expansion for calculation of the energy balance at one-quarter microsecond is shown in Fig. 45. This figure shows the energy-balance curves (Curves A and B of Fig. 42) for the first microsecond. Considering the energy balance at one-quarter microsecond, the modified rate of channel expansion obtained from Fig. 44 becomes 800 meters per second rather than the previous value of 913 meters per second. This gives a calculated pressure of 25,000 atmospheres rather than 32,300 atmospheres obtained previously. All three factors which are used in calculating the power to the shock wave, i. e., the pressure, channel lateral area, and wall velocity, are smaller than were used in the original calculation. As a result the new shock-wave power is found to be 50.8 megawatts instead of the previous value of 112.6 megawatts. Assuming that the energy to the shock wave is reduced by the same ratio, then only 12.4 joules have been dissipated in this manner rather than 27.5 joules. If one subtracts 12.4 joules from the energy which has been supplied to the spark, 19 joules, one finds that Curve A should be replaced by a new curve (Curve C in Fig. 45) which passes through 6.6 joules at one-quarter microsecond.

The effect of the reduced rate of expansion on Curve B at one-quarter microsecond may be calculated. With a lower pressure of 25,000 atmospheres, a lower value of energy density in the spark channel is

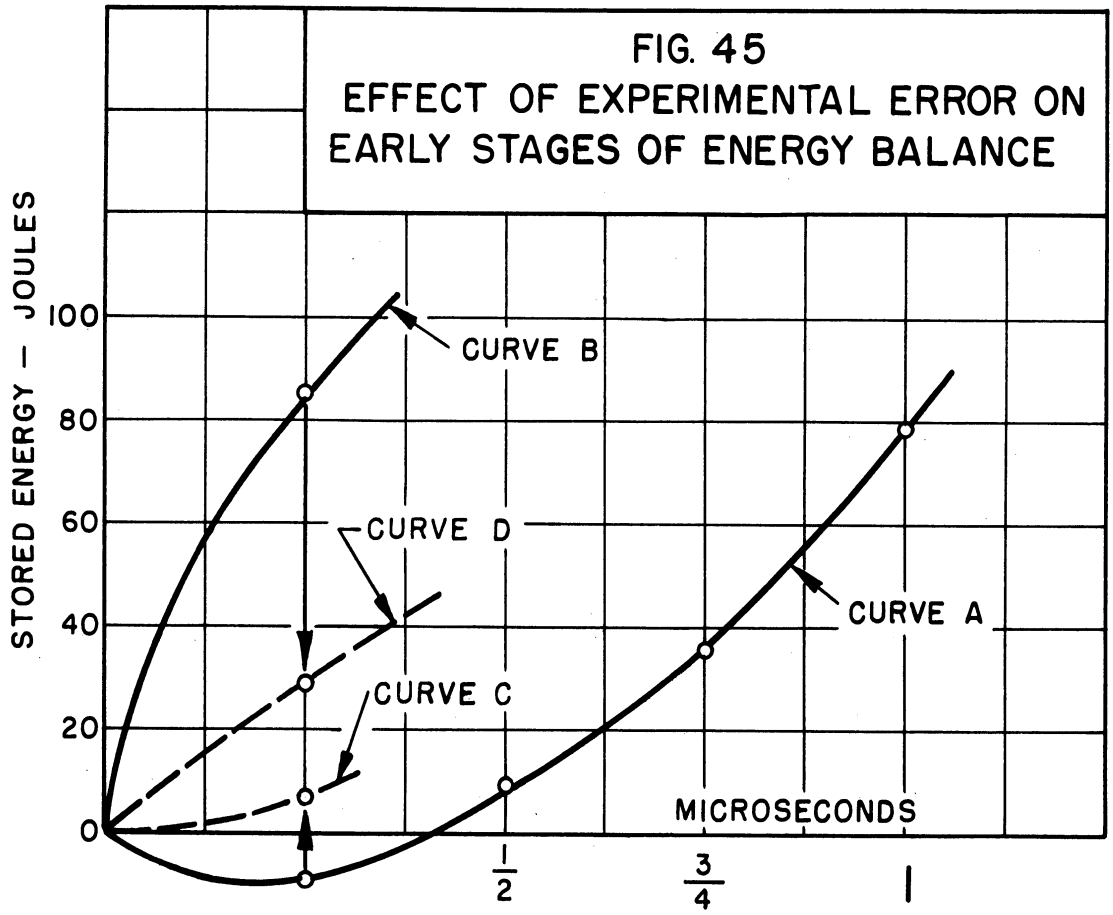

obtained (Fig. 41). The new energy density is 8.43×10^{9} joules per cubic meter. With the smaller channel volume of 3.43×10^{-9} cubic meters, the spark channel stores an energy of 28.9 joules. Thus Curve B should be replaced by a new curve (Curve D in Fig. 45) which passes through 28.9 joules at one-quarter microsecond rather than through 85 joules. Therefore, the effect of a smaller measured rate of channel expansion is to lower Curve B to Curve D and raise Curve A to Curve C, tending to bring them closer to agreement. In view of the approximate nature of the determination of the amount of refractive channel magnification, one would expect that if it is greater than the 10 percent which has been assumed, the two energy balance curves would be brought even closer together. The effects just discussed, which tend to raise Curve A and lower Curve B of the energy balance, would

not be appreciable very much later in the spark cycle, since the increase in channel size due to optical magnification would be a smaller percentage of the actual channel diameter.

Internal Pressure

We next turn to the discrepancy between Curves A and B of the energy balance (Fig. 42) substantially later than 1.6 microseconds. The accuracy of the higher Curve A depends on the accuracy with which the circuit input energy to the spark has been determined and on the accuracy of determination of the energy supplied by the spark to radiation and mechanical work output to the shock wave. The former is amply accurate for the present analysis. The radiation and shock-wave energies, which are obtained by integration of the corresponding power curves, grow progressively more accurate at later times since the early errors caused by optical channel magnification and jitter in the timing circuits become a smaller fraction of the total energy integrals. It is unlikely, then, that Curve A is very much in error at times later than 1.6 microseconds. There is, however, a valid objection to the procedure used in obtaining Curve B. In solving the particle-balance equations, the total particle density was computed from the measured pressure and temperature by means of the ideal gas law. It would be very surprising if the ideal gas law were to apply to the plasma of the underwater spark. The particle density is of the order of one-tenth that found in liquids and solids, and the high degree of ionization, about 30 percent, produces long-range interparticle forces. In fact, plasmas of only 5-percent ionization are considered as being "completely ionized," meaning that the interparticle Coulomb forces play a dominant role in determining the properties of the plasma. The

effect of these interparticle forces on the equation of state of the underwater spark plasma will now be considered from the viewpoint of internal gas pressure.

The subject of pressure in a gas may be organized according to the following viewpoint. If one begins with a given amount of an ideal gas, i.e., one having no interparticle forces and particles of zero volume, and considers it in free space, the volume of space which is occupied would tend to expand due to the kinetic motion of the particles. The average pressure on a surrounding envelope which would be required to constrain these particles to a given volume is called the kinetic pressure, $P_{kinetic}$. If each particle has a certain volume, or if each particle exerts a force of repulsion on every other particle, then the tendency to expand is further increased, and the necessary amount of increase of constraining pressure is called the repulsion pressure, $P_{repulsion}$. The tendency toward expansion produced by the preceding two effects may be inhibited by two additional factors. If there are also attraction forces between the particles, then the necessary constraining pressure from the enclosing envelope is reduced, and the amount of this reduction is called the attraction pressure, $P_{attraction}$. Further, if some of the gas particles are charged, and if there is a net transfer of charge through the volume of the gas, i.e., an electric current, then the resultant magnetic field due to this current produces average forces on the moving charged particles tending to force them together. Thus the necessary pressure applied to the gas by the surrounding envelope is reduced by an additional amount, called the pinch pressure, P_{pinch}. The remaining pressure on the surrounding envelope necessary to constrain the gas to a constant

volume is called the external pressure, $P_{external}$. The relations may be summarized by the following equation:

$$P_{external} + P_{pinch} + P_{attraction} = P_{kinetic} + P_{repulsion} \tag{6.30}$$

Often the repulsion and attraction pressures are grouped together and called the dynamic pressure. In addition, some authors call the difference of these two pressures the attraction pressure, since the effect of attraction forces usually predominates at the particle densities for which computations are most frequently made. Also, the difference between the attraction and repulsion pressures is often called the internal pressure. For solids and liquids at normal conditions the kinetic and internal (or dynamic) pressures are very large, their small difference being equal to one atmosphere.

The pinch pressure in Equation 6.30 may be approximately computed. The pinch pressure at any radius in a circular conductor of radius R, caused by a total current I which is assumed to be uniformly distributed over the cross section, is given by (48, p. 286)

$$P_{pinch} = \frac{\mu_o \mu_r I^2}{4\pi^2 R^4}\left(R^2 - r^2\right) \frac{\text{newtons}}{\text{meter}^2} \tag{6.31}$$

where μ_o equals $4\pi \times 10^{-7}$ $\frac{\text{henrys}}{\text{meter}}$, and μ_r is the relative permeability of the material of the conductor. This equation is an approximation for the present application, since the current density in the spark channel is not known to be uniform. The parabolic pressure distribution of Equation 6.31, when integrated over the channel circular cross section, gives an average channel pinch pressure of one-half the pressure at the center:

$$\text{Average } P_{\text{pinch}} = \frac{\mu_0 \mu_r I^2}{8\pi^2 R^2} \frac{\text{newtons}}{\text{meter}^2} \qquad (6.32)$$

This is the pinch pressure to be used in Equation 6.30, and its effect has already been taken into consideration in the energy-balance relations.

Our immediate objective is to obtain the kinetic pressure in the spark plasma, since it is the pressure which may be used together with the temperature and the ideal gas law to calculate the total particle density. The external pressure in Equation 6.30 is already known. It is the pressure which the spark exerts on its environment and is therefore the calculated pressure obtained from the rate of channel expansion. The problem therefore reduces to evaluating the attraction and repulsion pressures. These will be considered together, and the term internal pressure will be applied to the result obtained by subtracting the repulsion pressure from the attraction pressure.

Much effort has been devoted in the past to the problem of computing the internal pressure which arises in a gas due to interparticle forces. This effort takes the form of computing the virial coefficients in the equation of state of the gas. One has all the physical information necessary for such a computation when the interparticle potential is given as a function of particle separation. In general, this potential is also a function of the angular orientation of the particles, but the anisotropic properties of the particles are often neglected because the resulting analysis becomes much more complicated otherwise. For uncharged particles, the interparticle potential has a form similar to that in Fig. 46 (Ref. 49, p. 131). If the particle density is such that the average interparticle separation gives an

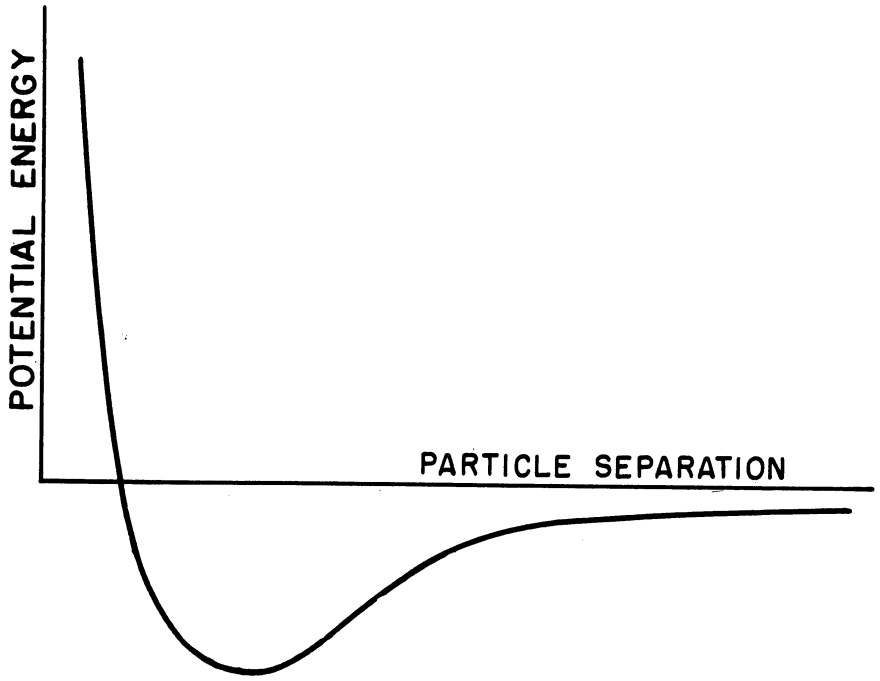

FIG. 46 TYPICAL INTERPARTICLE POTENTIAL ENERGY

average attraction force, then the net pressure will be an attraction pressure. If the density were great enough so that the average particle separation resulted in predominantly repulsion forces, then the resulting pressure would be a repulsive pressure. Such "super density" is seldom attained on the earth, even in solids. Equations have been developed from which the net attraction or internal pressure may be calculated (46, pp. 244, 290). The relationships will not be given here since there are three reasons why they do not apply to a highly ionized plasma. First, the attraction pressure calculation requires evaluation of an integral which does not converge for an interparticle force law which decreases less rapidly than the inverse fourth power of the separation as the separation approaches infinity. Use of the inverse-square Coulomb law does not give a determinate answer, since the Coulomb attraction is a "long-range" force. The second reason is very closely allied to the first. The derivation of the equation for internal pressure assumes that only binary collisions

occur. Where the long-range Coulomb forces predominate, a particle is continually being deflected by other particles; all interactions are multibody encounters. Indeed, it appears that the concept of collisions and mean free path should not properly be applied to particles with inverse-square force laws. The third reason why the attraction pressure relation does not apply to a plasma is that the derivation assumes that all particles of the gas exert forces which are described by the identically same force law on all other particles of the gas. In the highly ionized plasma there are attraction forces between some pairs of particles, repulsion forces between other pairs, attraction forces due to polarization of the neutral particles by the charged particles, and no forces at all between the pairs of neutral particles. (We assume here that the effects of short range Van der Waals forces between atoms may be neglected compared to the effects of Coulomb forces.)

The approach to the approximate calculation of the internal pressure in the underwater spark plasma is based on the concept of the Debye length. Debye and Huckel defined this length in the course of studying strong electrolytes. Fowler presents a discussion of the subject and gives the relation for the Debye length λ_D as follows (46, p. 272) (the equation has been converted to rationalized MKS units:

$$\lambda_D = \left(\frac{\varepsilon_0 \varepsilon_r kT}{e^2 \sum_\beta z_\beta^2 n_\beta} \right) \text{meters.} \qquad (6.33)$$

where $\varepsilon_0 \varepsilon_r$ is the dielectric constant of the medium containing the ionized particles,

q_e is the charge on the electron,

Z_β is the number of units of charge on the β-type ion, and

n_β is the average particle density of the β-type ion.

The summation is extended over all types of ionized particles.

The Debye length is the distance from an ion at which its potential field is reduced by local polarization of the charged region in its vicinity to 1/e of what it would be if the ion were isolated. This shielding distance has been interpreted by various authors as the effective distance that the field of a given ion penetrates a charged region. Within a sphere of this radius surrounding the ion, individual particle-particle interactions must be considered. Outside this sphere only collective particle motions affect the ion, and so the charged medium may be treated as a continuum having the average net charge of the region (50). The Debye length in the plasma of the underwater spark at current maximum is found to be 3.8 Angstrom units. However, the average interparticle spacing is 10 Angstrom units. The use of the Debye length under such conditions is probably not rigorously correct, but this result does suggest that the plasma surrounding any given ion may be treated as a charge continuum without introducing an order-of-magnitude error. The internal pressure will be determined assuming that the plasma is a continuum external to a sphere having a volume equal to the average volume occupied by a plasma particle.

Consider a sphere of radius R surrounding a charged particle, where the volume within the sphere is the average volume per particle in the plasma. The polarization of the plasma may be represented by the image charge of the ion in the plasma continuum; the image charge may in turn be represented by a uniformly distributed charge on the sphere

surface equal in magnitude to the ion charge. If a reference direction is chosen through the ion and its associated concentric sphere, and the component of net force on the surface charge in the reference direction is integrated over a hemisphere, one obtains the force in the reference direction on the hemisphere, and hence on the plasma, due to the presence of the ion (Fig. 47). The same magnitude of force is exerted on the second enclosing hemisphere tending to hold the two together. This force, divided by the cross-sectional area of the sphere, is the internal pressure created by the interionic forces. The result is

$$P_{internal} = \frac{q^2}{32\pi^2 \varepsilon_o R^4} \qquad (6.34)$$

where

q is the ion charge,

R is the radius of the sphere having a volume equal to the average volume per particle, and

ε_o is the dielectric constant of free space.

This relation is applied in the following manner:

$$P_{external} + P_{pinch} + P_{internal} = P_{kinetic} = NkT \qquad (6.35)$$

At current maximum, $P_{external} + P_{pinch}$ is equal to 8.33×10^8 newtons per square meter. Substitution in 6.35 gives

$$8.33 \times 10^8 + \frac{q^2}{32\pi^2 \varepsilon_o} \left(\frac{4\pi N}{3}\right)^{4/3} = NkT \qquad (6.36)$$

If the appropriate values are substituted for current maximum, and the equation solved for N, one gets $N = 2.54 \times 10^{27}$ per cubic meter. Thus the total particle density at current maximum should be 2.54×10^{27}

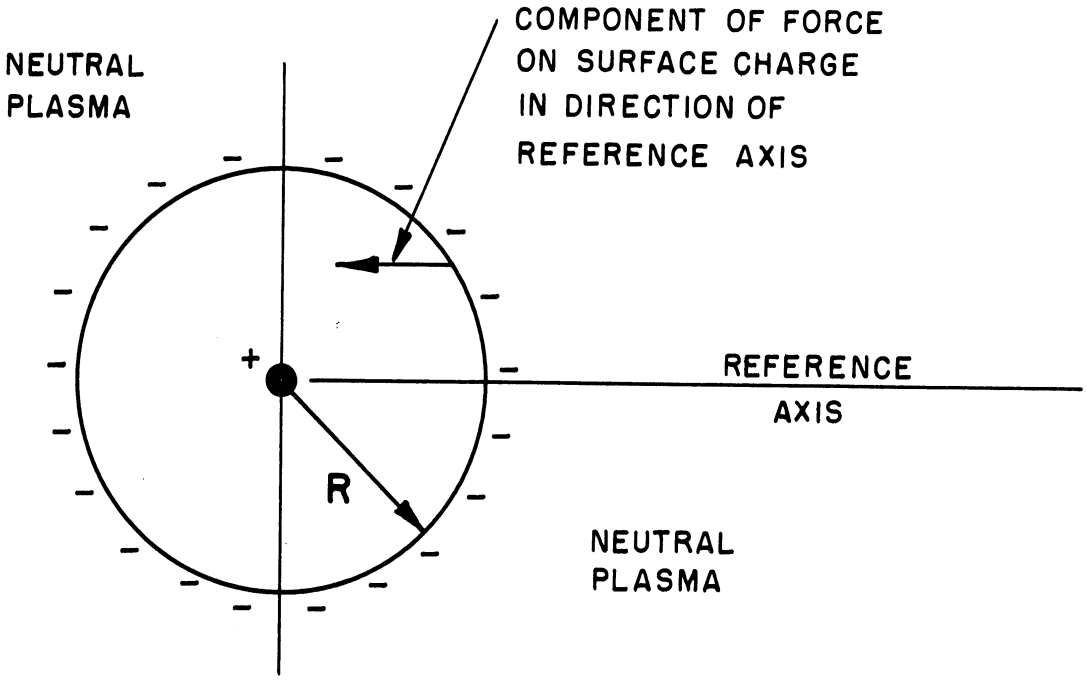

FIG. 47

CALCULATION OF INTERNAL PRESSURE

rather than the value formerly obtained by use of the ideal gas law of 2.06×10^{27}. If the new N is now substituted in the $P_{internal}$ term in Equation 6.36, one finds an internal pressure of 2170 atmospheres. Thus the internal pressure is found to be of the same order of magnitude as the external pressure, resulting in a substantial increase in the kinetic pressure. If one carried out the preceding calculation for later times in the spark cycle, the internal pressure would not be as large a fraction of the external pressure, but it would be of the same order of magnitude. The significance to be attached to this result is that the plasma of the underwater spark is not an ideal gas, so that the internal pressure due to interionic forces is an appreciable factor in the equation of state of the gas. The fact that Curve A of the spark-channel energy-balance curves lies appreciably above Curve B (Fig. 42) may be taken as experimental evidence for the existence of this plasma

internal pressure.

It would be appropriate, at this point, to recalculate the particle balance for the underwater spark using the new value of total particle density N. Equations 6.12 to 6.16 and 6.19 could be solved again in the manner already discussed. The result would be that Curve B of the energy balance (Fig. 42) would be brought into closer agreement with Curve A. Such a recalculation will not add significantly to the theory of the underwater spark and is therefore beyond the scope of this study.

CHAPTER VII

ADDITIONAL CALCULATIONS BASED ON THE RESULTS OF THE ENERGY BALANCE

One may now make use of the results of the energy balance to carry out certain auxiliary calculations of interest. One of these concerns the amount of water necessary to make up the spark-channel plasma. Fig. 48 is a curve of the number of water molecules composing the plasma as a function of time. By taking the slope of this curve at current maximum, 1.9 microseconds, one obtains the rate at which water is being inducted into the channel volume. The result, 0.97×10^{25} molecules per second, multiplied by the energy necessary to convert liquid water to spark plasma, about 35 electron volts per molecule, gives the power required at the channel surface. The result shows that the plasma must supply 55 megawatts to the channel wall in order to induct water at the required rate. We will conclude shortly that the plasma has a thermal conductivity of 86 watts per meter per degree Kelvin. If it is assumed that the electrical power input to the spark is uniformly distributed throughout the channel volume, and that the required energy is carried to the wall purely by thermal conduction, then the central temperature on the spark axis would have to be of the order of three million degrees in order to transfer the necessary energy to the channel wall. Such a large temperature does not seem consistent with the experimental fact that the apparent brilliance and the electrical behavior of the spark are not markedly changed by flattening the spark between parallel glass plates.

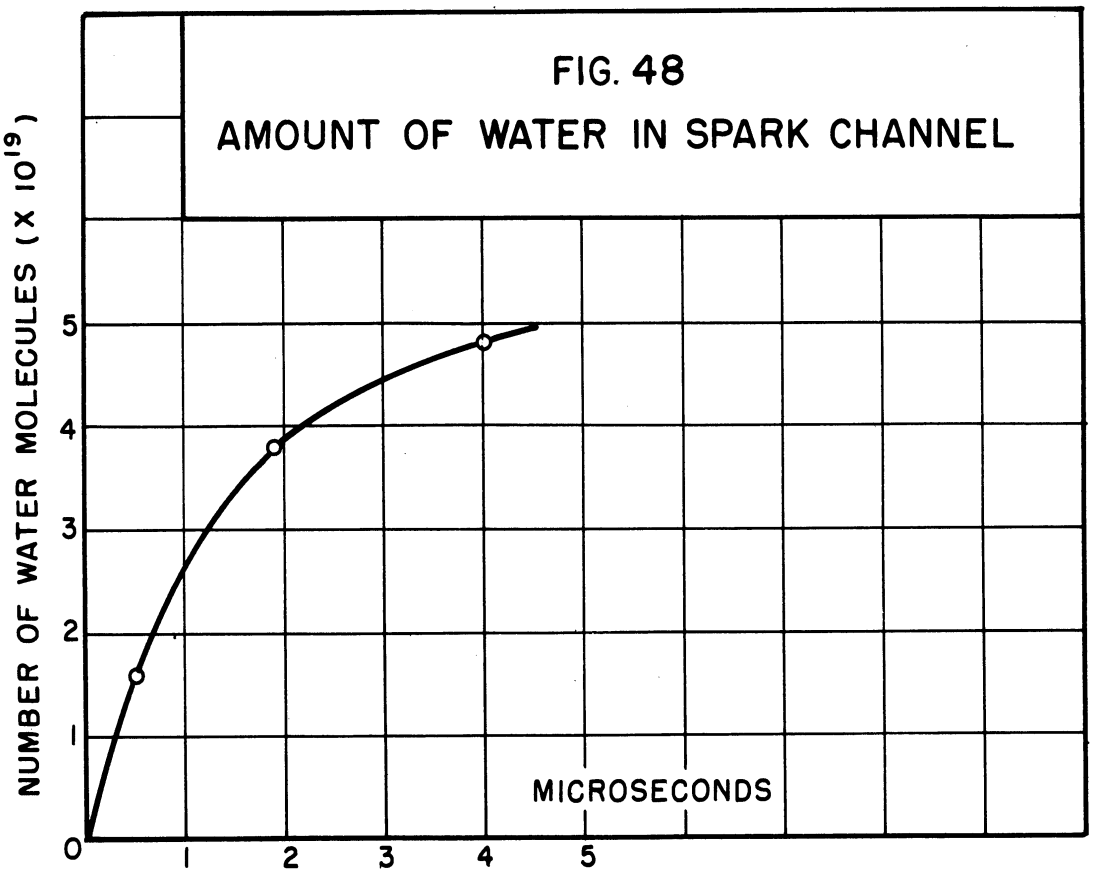

There is another mechanism capable of supplying the required wall energy without the requirement of a high thermal gradient. This is wall recombination of plasma ions. For low pressure gas discharges, wall recombination is the principal inverse process of the ionization processes taking place in the channel. This is to be expected since recombination will never occur in a two-body encounter in which the participating positive and negative charges have appreciable relative angular momentum. A third body must intercede in order to cause the recombination to take place. In the rarefied gas of a low pressure discharge there are negligible numbers of three-body encounters, so the discharge wall serves as the only available third body in the recombination process. In high pressure discharges appreciable numbers of multibody encounters take place so that recombination of ions occurs

chiefly throughout the volume to such an extent that volume recombination is the most important inverse process of the ionization. However, wall recombination would be still taking place in exactly the same manner as in a low pressure discharge. An estimate of the amount of wall recombination for the underwater spark may be made. The electrons, because of their greater random thermal velocities, will collide with the channel wall much more often than the positive ions. Therefore, the factor which limits the rate of wall recombination is the rate at which positive ions reach the wall. The rate of arrival due to random thermal motion is given by the following (51, p. 373):

$$L = n\left(\frac{kT}{2\pi m}\right)^{1/2} \qquad (7.1)$$

where

L is the rate of arrival per unit area,

n is the average particle density, and

m is the mass of the particles.

For the conditions in the underwater spark at current maximum this relation gives 2.17×10^{30} ions per second per square meter. If all ions which reach the wall recombine, thus giving up their ionization energy, there is available at the spark-channel wall a power of 438 megawatts. This is approximately eight times the required amount. It requires, then, a recombination of only one-eighth of the ions colliding with the channel wall to supply the necessary wall energy. The reason why only one-eighth would recombine is not immediately evident. The channel wall is a very complicated region, as will now be discussed.

It should be realized that the channel wall is not a liquid-gas interface. Since the pressures in the vicinity of the underwater spark

are far above the critical pressure of water, the transition from liquid to plasma gas is continuous, with no change of phase (vaporization) being necessary. Further, the thermal gradient in this transition region is probably very high. If the thermal gradient times the average mean free path of the particles in this region is large compared to the temperature of the particles, then thermodynamic equilibrium does not exist near the channel wall. Further, the existence of an internal pressure in the plasma would call for a particle-density gradient in this region. Also, there is probably a substantial electrical gradient near the wall as a result of the differing mobilities of electrons and ions. Finally, the magnetic field due to the spark current is very strong at the channel wall, about 13.5 webers per square meter (135,000 gauss) at current maximum. A detailed analysis of this region would be very complex. We regard the channel wall in this investigation as a relatively thin region in which the temperature, the degrees of dissociation, excitation, and ionization, and the particle density all gradually undergo a continuous transition from liquid water to highly ionized plasma.

There are other interesting characteristics of the underwater spark which may be calculated. The rate of induction of water molecules into the spark plasma enables one to compute the resulting contribution to the rate of channel expansion caused by water vaporization at the channel wall. This contribution does not generate shock-wave pressure and could cause an error in the pressure calculations. However, the vaporization at the channel surface is found to contribute a wall velocity of only 10 meters per second at current maximum. This is negligible compared to the measured rate of expansion of 348 meters per

second. Additional information of interest, obtainable from the particle-balance results, is that the plasma at current maximum has a mass density of 0.016 grams per cubic centimeter, the underwater spark is a low-gradient electrical discharge, and the high magnetic field is not effective in reducing the electron mobility within the spark plasma since the electron cyclotron radius is large compared to the electron mean free path.

Electrical Conductivity of the Plasma

Because the interionic forces play so important a part in the interactions between particles constituting a highly ionized plasma, one cannot use the conventional simplified kinetic-theory values for mean free path and the several transport coefficients. Any computation based on the gas model which consists of hard elastic spheres gives a mean free path greater than the true value, resulting in exaggerated values for the mobility, diffusion coefficients, and thermal conductivity. Gvosdover has developed an expression for the effective collision cross section for electrons moving through positive ions (10, 52). From this a mobility, and consequently an electrical conductivity, may be calculated. The equation for electron mobility based on the Gvosdover cross section has been presented by Glaser (10). Converting this relation to the form to give electrical conductivity, and converting to MKS units, one gets

$$\sigma = \frac{6.28 \times 10^{-21} (kT)^{3/2}}{\beta e^2 m_e^{1/2} \ln\left(1.67 \times 10^{-10} \frac{kT}{\beta e^2 n_e^{1/3}}\right)} \frac{\text{mhos}}{\text{meter}} \qquad (7.2)$$

where

σ is the electrical conductivity,

e is the charge on the electron,

m_e is the mass of the electron,

n_e is the electron density,

k is Boltzmann's constant, and

T is the temperature in degrees Kelvin.

For the plasma of the underwater spark at current maximum, the Gvosdover relation gives an electrical conductivity of 5.4×10^4 mhos per meter. More recently Spitzer and Harm have developed a theory for the thermal and electrical conductivity in a completely ionized gas (53). "Completely ionized" is considered to mean at least approximately 5-percent ionization, so that effects of long-range Coulomb forces predominate. The conventional definition of mean free path is not used in their work; the equivalent of mean free path is the distance a particle travels, on the average, until it suffers a total deflection of 90 degrees. The equation for electrical conductivity developed by Spitzer and Harm, when converted to MKS units, is

$$\sigma = \frac{1.26 \times 10^{-20} \, (kT)^{3/2} \, \gamma_E}{e^2 Z m_e^{1/2} \ln \left[\frac{0.994 \times 10^{-15} \, (kT)^{3/2}}{e^3 n_e^{1/2} Z (1+Z)^{1/2}} \right]} \quad \frac{\text{mhos}}{\text{meter}} \qquad (7.3)$$

where

Z is the mean ionic charge, given by $Z = \sum_i \frac{n_i Z_i^2}{n_e}$ with the summation extended over all ion types,

γ_E is a function of Z, equal to 0.582 for $Z = 1$, and

all other symbols have the same meanings as given for Equation 7.2.

Applying the theory of Spitzer and Harm to the underwater spark plasma at current maximum, the electrical conductivity is found to be 10×10^4 mhos per meter. Both of the preceding calculated conductivities are quite significant, since the value obtained experimentally from the present study is 5.6×10^4 mhos per meter at the current maximum (Column 15 of Table III). In order to investigate the effect of temperature of the underwater spark on its electrical conductivity, the theory of Spitzer and Harm was applied to the case mentioned earlier where the spark plasma was assumed to have a temperature of 200,000 degrees Kelvin. The resulting value of electrical conductivity is 21.4×10^4 mhos per meter. Therefore, if the spark plasma were heated from 29,950 degrees to 200,000 degrees Kelvin at a constant pressure of 8300 atmospheres, the electrical conductivity would approximately double.

Thermal Conductivity of the Plasma

The theory of Spitzer and Harm may be applied to calculate the thermal conductivity of the plasma of the underwater spark at current maximum. The equation, in MKS units, is

$$K = \frac{1.23 \times 10^{-19} k (kT)^{5/2} \delta_T}{e^4 m_e^{1/2} Z \ln\left[\frac{0.994 \times 10^{-15} (kT)^{3/2}}{e^3 m_e^{1/2} Z (1+Z)^{1/2}}\right]} \quad \frac{\text{watts}}{{}^\circ K \text{ meter}} \qquad (7.4)$$

where

δ_T is a function of Z, equal to 0.225 for $Z = 1$, and all other symbols have the same meanings as in Equations 7.2 and 7.3.

The above equation yields a value of 86.2 watts per meter per degree Kelvin for the thermal conductivity of the underwater spark plasma. This is approximately one-fifth the conductivity of metallic copper or silver. There are no experimental data in this investigation suitable for checking this result. Thermal conduction, which refers to the rate at which energy is transported in a material due to a temperature gradient, may occur by several processes. If there is a thermal gradient, then there is a gradient of the average random kinetic energies of the particles of the plasma. This gives the classical conductivity of the gas. However, there may also be a dissociation gradient, an excitation gradient, and an ionization gradient. These gradients may be large in a temperature range in which the degrees of dissociation, excitation, or ionization are rapidly varying functions of the temperature. Interdiffusion of particles from regions of different degrees of dissociation, excitation, or ionization, therefore, may contribute appreciably to the rate of energy transfer along the thermal gradient, and hence to the thermal conductivity. A third factor, radiation, may also contribute to the thermal conductivity since the radiation from a hotter region contains more energy (Stefan-Boltzmann law) than the radiation from a cooler region. The net result of the radiant energy interchange is a transfer of energy along the thermal gradient. Hocker and Schulz have presented some initial work regarding thermal conductivity in gases (54). They subdivide the thermal conductivity into components due to kinetic motion of the atoms, kinetic motion of the electrons, molecular dissociation, and atomic ionization. For the present study of the underwater spark, the contributions to the plasma thermal conductivity due to dissociation, excitation, ionization, and radiation were evaluated by an approximate first order method. For the conditions

in the underwater spark, all contributions were found to be negligible compared to the expected conductivity caused by random motion of the plasma particles.

CHAPTER VIII

APPLICATION OF THE UNDERWATER SPARK

The emphasis in this investigation has been to consider the underwater spark as a research tool for the study of high-pressure, high-temperature electrical discharges. It will not be amiss, however, to describe some applications of the spark which depend on its external characteristics. The first of these characteristics having applicational potential is the very high surface brightness, which is a consequence of the 30,000-degree temperature and the high particle density. Since the spark radiates as a diffuse blackbody at a known temperature, and the channel dimensions are known, one may compute the amount of radiation over any solid angle and over any spectral range by use of Planck's law. Unless the light is to be used for visual illumination, which is quite unlikely, one should express the flux in absolute units (watts) rather than in luminous units (lumens). If a phototube or photographic film is to be used to detect the light from the spark, then the spectral response of the tube or film should be used, in contrast to using the response curve of the human eye as is done when one wishes to determine visual effectiveness. As it happens, the radiation from the underwater spark has a large output in the ultraviolet, where films and photosurfaces have maximum sensitivity. Even with water, lucite, and air interposed in the optical path of an optical system, one has available the radiation down to 3400 Angstroms. Since air and water transmit reasonably well down to approximately 2200 Angstroms, a suitably mounted quartz window and quartz camera optics would give a large

increase in actinic or photoemissive effectiveness.

The light output of the spark lasts about 28 microseconds as a consequence of the considerable storage of energy in ionization and excitation. This duration is short enough for photography of moderately fast-moving objects such as water droplets in a flowing stream of water, but for more rapidly moving objects which one encounters in ballistic or supersonic-flow problems the duration must be reduced. A preliminary investigation of the use of the underwater spark as a light source was made (55). In this, attempts were made to reduce the duration of underwater spark light output by abbreviating the input current. The attempts were fruitless, since the light duration remained about the same as before, but the peak light output was reduced because of a lower energy input. Various mechanical shutters were then tried, and one was evolved which is capable of closing in about one microsecond. This is the "shatter shutter," shown in Fig. 49. The glass block shown is painted black except for a small aperture for light to pass through. The initial light output of the spark is not modified until the high pressure shock wave passes through the glass. This shock front stresses the glass beyond its elastic limit, producing a large number of fine cracks (crazing). This process of cracking is called secondary fracture and, of course, advances through the glass at sonic velocity (about 5300 meters per second) in contrast to primary fracture, or ordinary cracking, which progresses at subsonic velocity (56). The result is that the glass block is rapidly converted into a translucent body which scatters the light and causes it to be absorbed by the blackened walls. By this method the duration of the light pulse has been reduced to about two microseconds with no diminution of the initial light output.

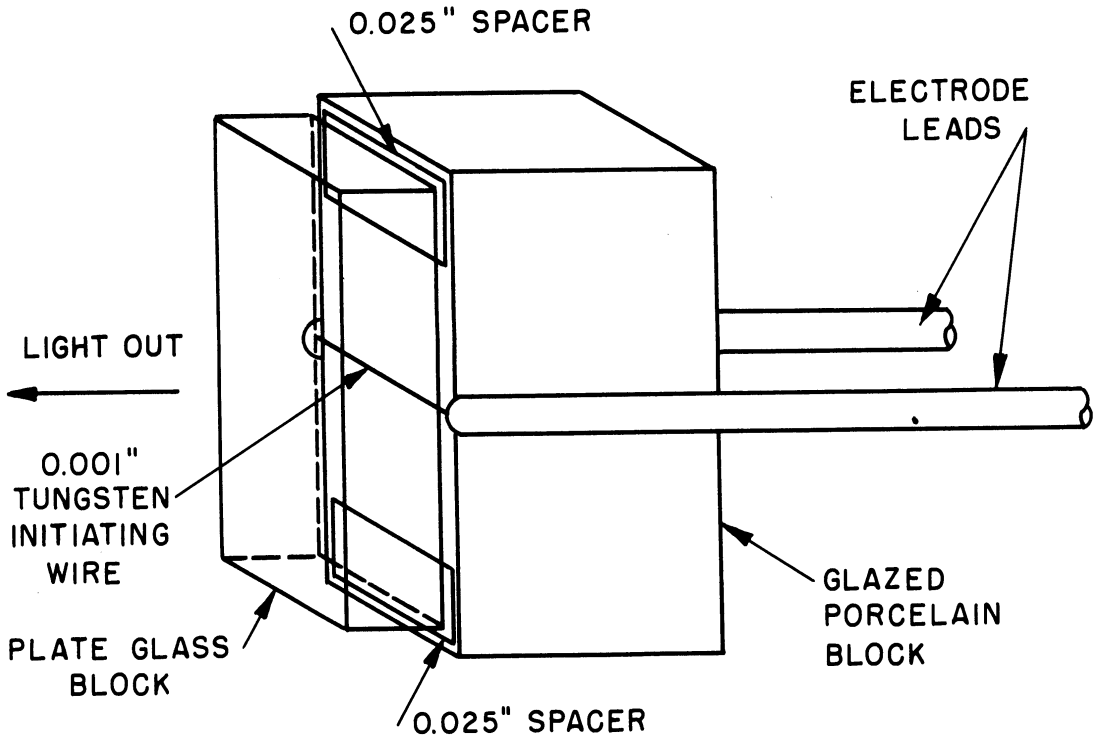

FIG. 49 SHATTER SHUTTER

The primary applications of the underwater spark would be where source brightness is of primary importance, such as in interferometer, schlieren, and shadowgraph systems. As an example of the high surface brightness, a shadowgraph of a drafting compass was taken by use of the underwater spark and a shatter shutter with only a 1/16-inch square opening for the light to pass through. The two-microsecond light pulse amply exposed the film placed 29 feet away. The shadow produced by the compass, which was located 18 inches from the film, shows very fine detail, with clear diffraction patterns evident at the edges and corners.

Sonic or Pressure Source

Other applications of the underwater spark utilize the mechanical, or shock-wave, output of the rapidly expanding channel. H. C. Early

has used the pressure pulse to punch various-shaped holes in sheet metal. A hole of the desired shape is cut in a block of steel. This block plays the part of the die in conventional punching practice. The metal to be punched is placed in contact with this backing-block, and an underwater spark is produced adjacent to the metal sheet. Steel sheets of 42 mils thickness have been successfully punched, as well as aluminum and copper sheets. Inasmuch as static pressures of the order of several thousand atmospheres would be required to shear these sheet metals, this serves as an order-of-magnitude check on the pressures as calculated in this investigation.

Rust and Drubba have applied the underwater spark as a sonic source for underwater echo sounding (17). The energy is stored on a two-microfarad capacitor charged to about three kilovolts. With their apparatus soundings have been taken at a depth of 35 meters.

Elastic Constants of Materials at High Stress

It is possible that the underwater spark could be utilized to obtain the elastic constants of materials at high transient stress. There is increasing interest in this subject as a result of the more severe requirements placed on materials in turbines, projectiles, and aircraft (57, 58, 59). No investigation of this application of the underwater spark has yet been undertaken. In some of the Kerr cell photographs the position of the shock front in the water is made evident by the refractive discontinuity in the image of an object such as a screen in the background of the photograph. A prism of the material to be studied could be placed so that the shock wave passing through it would be refracted due to the difference in sonic velocity in the material and in the water. A Kerr cell photograph showing the

refracted shock front and a portion of the unrefracted shock front would give the angle of refraction. This, together with the prism angle, would enable one to obtain the velocity of the shock wave in the material. Since the velocity is given by the square root of the ratio of elasticity to density, the elasticity could be calculated. Water has an acoustic impedance approximately one-tenth that of most metals so that approximately two-thirds of the shock-wave energy would be reflected at each metal-water interface due to impedance mismatch. However, a stored energy greater than that used in the present study, as well as suitable focussing methods, could be utilized to compensate for these losses.

APPENDIX A

THE SAHA THERMAL-IONIZATION EQUATION

The Saha equation is a product of the field of astrophysics. Astronomers noted that spectra taken of light from the surface layers of the sun showed lines corresponding to ions of a higher level of ionization than the lines which appeared in spectra of light from deeper-lying layers. This phenomenon would suggest that the outer layers of the sun are hotter than the inner layers, provided that one assumed that the Boltzmann relation describes the equilibrium populations of ionized levels as well as the excited levels of the atoms. This picture of an astral body being hotter on the outside than on the inside was inconsistent with the fundamental concepts of stellar dynamics. It was concluded therefore that pressure as well as temperature must control the levels of ionization of a gas, whereas the excited levels are affected only by the temperature. The physical reason for this difference may be visualized. In both ionization and excitation processes, the elevation of a gas particle to a higher level may be brought about by similar physical events. However, the decay back to lower levels is fundamentally very different in the two cases. For excitation decay, a second particle, an electron, is not required. Thus an excited atom, whether in a dense gas or isolated in empty space, would have the same probability of decaying regardless of the presence of other particles (We neglect here the distortion of the atom which may take place in a dense gas.). However, for ionization decay, an electron is required. An ionized atom, isolated in free space,

would never decay, whereas it would return to its lower level rapidly if immersed in a cloud of electrons. The probability of decay is strongly affected by the presence of other particles. The equilibrium populations of ionized levels therefore depend on gas pressure as well as temperature.

In 1920 Saha suggested that thermal ionization could be treated as an equilibrium chemical reaction (60). The degree of reaction, which depends on the molar concentrations of the reacting components, would therefore be analogous to the degree of ionization, which depends on the electron concentration. The analysis will be briefly outlined (61, pp. 402-414). Consider an equilibrium reaction given by the following reaction equation:

$$\sum_i n_i A_i \rightleftharpoons \sum_j n_j A_j - U \qquad \text{(A.1)}$$

where n_i, n_j are the number of moles of reacting components A_i, A_j. U is the energy required per mole to drive the reaction toward the right. The condition for chemical equilibrium at any temperature and pressure is given by the law of mass action, which is

$$\left(\frac{\prod_j x_j^{n_j}}{\prod_i x_i^{n_i}}\right) p^{\left(\sum n_j - \sum n_i\right)} = K \qquad \text{(A.2)}$$

where

p is the total pressure,

x_i, x_j are mole fractions of reacting components A_i, A_j, and

K is the equilibrium constant, a function only of the temperature.

The value of K is obtained from Nernst's equation (61, p. 412):

$$\ln K = -\frac{U}{RT} + \frac{1}{R}\int \frac{\int\left(\sum_j n_j c_{pj} - \sum_i n_i c_{pi}\right)dT}{T^2}\,dT + \frac{\Delta S_0}{R} \qquad \text{(A.3)}$$

where c_{pi}, c_{pj} are specific heats at constant pressure. When these relations are applied to an ionization reaction, the thermal ionization equation is obtained except for an integration constant, $\frac{\Delta S_0}{R}$. This integration constant plays the part of the ratio of fundamental constants and partition functions in the complete equation and cannot be evaluated without the use of statistical mechanics.

The preceding method of obtaining the thermal-ionization equation has followed its historical development, but this is not the most desirable method of derivation. There are several assumptions which had to be made which would cast doubt on its general validity, although the final equation is the same as that obtained by other methods. A first assumption is implied when one compares thermal ionization to a chemical reaction. In a chemical reaction, the reacting particles interact by approaching each other closely, i. e., by colliding. Therefore, it is questionable whether the equation so derived would apply to an ionized gas in which thermal equilibrium is attained in large measure by radiative energy transfer. A second assumption, inherent in the analogy between a chemical reaction and an ionized gas, follows from the fact that a chemical reaction is electrically neutral; there are always the same number of positive charges involved as there are negative charges. One would then question whether the resulting equation applies to a gas which is made up predominantly of charges of one sign. Other assumptions of a more direct nature also were required in the

preceding derivation. All the components of the gas were assumed to be ideal, and the law of partial pressures was employed. And finally, the specific heat at constant pressure of all components of the gas, ions, atoms, and electrons was considered to be 5/2 R per mole. These assumptions would seem to limit the applicability of Saha's equation quite stringently. Nevertheless, a derivation of the equation by statistical mechanics methods, in which none of the preceding assumptions is necessary, leads to the same result except for the integration constant mentioned earlier. The derivation by use of the law of mass action and Nernst's equation has served its purpose as the avenue through which the concept of thermal ionization was first developed, but another method of derivation is more direct and general.

Menzel has presented a derivation of the Saha equation based on the methods of statistical mechanics (62). Thermal ionization is introduced in such a way that it may be described by means of the Boltzmann relation. The Saha equation is thus shown to be a special form of the Boltzmann relation, and its description of the populations of ionized levels is completely in harmony with the description of the relative populations of excited levels within the atoms or ions by the Boltzmann relation. The importance of this derivation is that some of the restrictive assumptions necessary in the older derivation are removed. The only two assumptions which are necessary in the Menzel derivation are that the gas must be in thermodynamic equilibrium and that the effects produced by interparticle fields must be negligible. The mechanism of energy interchange between particles is not restricted to collisions only, there is no necessity of assuming 5/2 R as the constant-pressure specific heat of all particle types present, and the

gas is not required to be electrically neutral. There may be a considerable excess of positive ions or of electrons. It is thus seen that the Saha ionization equation is not necessarily applicable to the highly ionized plasma of the underwater spark, since there is evidence that the interparticle Coulomb forces are quite appreciable. A justification for the applicability of the Saha equation to a dense ionized gas may sometime in the future be evolved utilizing the concept of the Debye shielding distance. In the plasma of the underwater spark the Debye length is less than the average particle spacing, hence the effective field of an ion does not extend greatly beyond its nearest neighbors. This leads to the conclusion that the interparticle forces are not spatially extensive enough to modify seriously the form of the Saha equation.

The derivation of the Saha equation will be carried out from the viewpoint of statistical mechanics. Let $n_{\alpha\beta}$ be the particle density of atoms which have been ionized α times and excited to the β energy level, and let $g_{\alpha\beta}$ be the statistical weight obtained from the spectral term of the α-ionized ion excited to the β level. The symbol n_α will signify the total number density of atoms of all levels of excitation in the α-ionized state. $B_\alpha(T)$ is the partition function of the atom in the α-ionized state. The number of electrons per unit volume will be designated by n_e. The following relation is immediately obvious:

$$\sum_\beta n_{\alpha\beta} = n_\alpha \tag{A.4}$$

The Boltzmann relation for the excitation within the α stage of ionization may be written as

$$\frac{n_{\alpha\beta}}{n_\alpha} = \frac{g_{\alpha\beta}}{B_\alpha(T)} e^{-\frac{\chi_{\alpha\beta}}{kT}} \qquad (A.5)$$

where $\chi_{\alpha\beta}$ is the energy of the β-excited level above the ground state for the α-ionized atom. In all that follows, the various terms are considered to be the time-average densities of the various particle types averaged over a time interval long compared to the time scale of the microscopic interparticle interactions. The symbol χ_α will designate the ionization energy measured from the ground state of the α-times ionized atom.

We consider only single ionization in the present derivation, but it should be realized that the same procedure can be applied to obtain an identical equation relating any two successive stages of ionization. In other words, the resulting relation is independent of the particular α chosen.

Consider an energy-level diagram for a normal nonionized atom (Fig. 50a). The Boltzmann equation will be applied to relate the population of electrons in the energy gap, $d\mathcal{E}$, of the continuum to the population of electrons in such bound (discrete) states of the atom which result in placing it in its ground level. Then the number of electrons in the gap, $d\mathcal{E}$, will be integrated over all energies of the continuum, and the result should give the total number of free (unbound) electrons.

The unit of volume of configuration space will be chosen to be the average volume occupied by a singly ionized atom in its ground state. The size of this volume is therefore $\frac{1}{n_{11}}$ (Fig. 50b). In general there will be more than one electron within this volume, but in

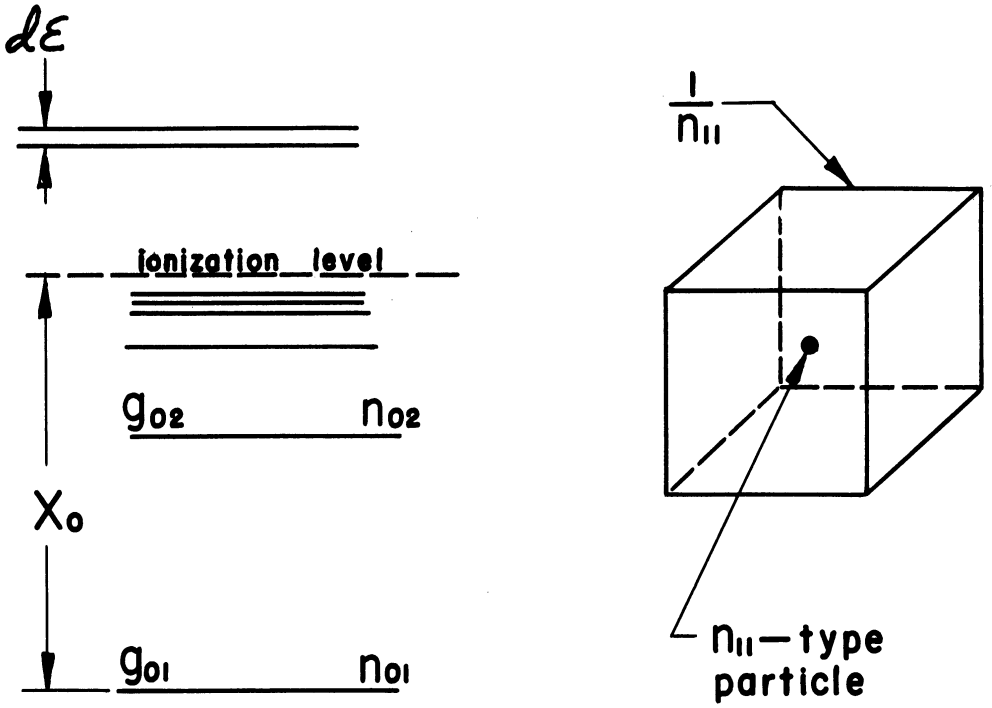

(a) (b)

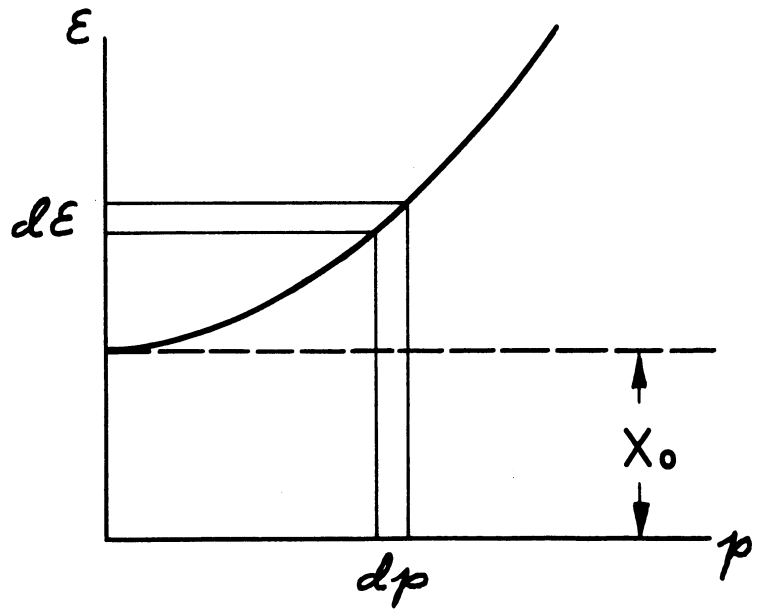

(c)

FIG. 50 FIGURES FOR DERIVATION OF SAHA IONIZATION EQUATION

any case it will contain $\frac{n_e}{n_{11}}$ electrons. There is no restriction here that the number of electrons shall equal the number of ions; the gas can contain predominantly charges of either sign if desired.

It is necessary to assign a statistical weight to the energy gap, $d\mathcal{E}$. In classical statistics, the statistical weight would be taken to be proportional to the volume occupied in six-dimensional phase space by electrons in the energy range, $d\mathcal{E}$, and in the volume $\frac{1}{n_{11}}$. In the present quantum statistical viewpoint, we divide the phase space up into six-dimensional volume units equal to h^3 (h is Planck's constant). Each h^3 volume can contain at most two electrons. The justification for this procedure is that this assignment of weights leads to a compatibility, or consistency, between quantum and classical statistics (63, p. 190). It is a form of the correspondence principle. An incremental volume in phase space is given by

$$d^6v = dp_x\,dp_y\,dp_z\,dx\,dy\,dz \qquad \text{(A.6)}$$

where x, y, z and p_x, p_y, p_z are coordinates and conjugate momenta respectively. The units of this volume increment are cubic joule-seconds. The number of possible electronic states within this volume unit is

$$d^6g_e = \frac{2}{h^3}\,dp_x\,dp_y\,dp_z\,dx\,dy\,dz \qquad \text{(A.7)}$$

Since the distribution in momentum space is isotropic, this may be rewritten as

$$d^4g_e = \frac{2}{h^3}\,4\pi p^2\,dp\,dx\,dy\,dz \qquad \text{(A.7a)}$$

where p is the total momentum. The statistical weight dg to be assigned to the gap $d\mathcal{E}$ is therefore the number of electronic states in the interval $d\mathcal{E}$ and in the volume $\frac{1}{n_{11}}$ multiplied by the statistical weight of the ion in the ground state, thus

$$dg = g_{11} \frac{2}{h^3} (4\pi p^2 dp) \frac{1}{n_{11}} \tag{A.8}$$

The relation between the momentum p and the energy $\mathcal{E}$ is given as follows, using the ground state of the atom as reference:

$$\mathcal{E} = \chi_0 + \frac{p^2}{2m_e} \tag{A.9}$$

This relation is plotted in Fig. 50c. It should be noted that use of this expression implies directly that there are no interparticle forces between the ion and any of the free electrons. If there were, there would be a potential energy term in Equation A.9. We now write Boltzmann's relation for the energy increment $d\mathcal{E}$ and the ground state of the atom as

$$\frac{\text{Number of electrons in } d\mathcal{E} \text{ and in } \frac{1}{n_{11}}}{\text{Weight of } d\mathcal{E}} = \frac{\left(\frac{n_{01}}{n_{11}}\right)}{g_{01}} e^{-\frac{\mathcal{E}}{kT}} \tag{A.10}$$

This is now rewritten as

$$\left.\begin{matrix}\text{Number of electrons in} \\ d\mathcal{E} \text{ and } \frac{1}{n_{11}}\end{matrix}\right\} = \left(g_{11} \frac{2}{h^3} 4\pi p^2 dp \frac{1}{n_{11}}\right)\left(\frac{n_{01}}{n_{11} g_{01}}\right) e^{-\frac{\chi_0 + \frac{p^2}{2m_e}}{kT}} \tag{A.10a}$$

This expression should be integrated over all energies from χ_0 to infinity. However, to any given number of states in the energy interval $d\mathcal{E}$, there may be ascribed an exactly equal number of states in the

corresponding interval dp (See Fig. 50c). The integration may therefore be carried out over p in momentum space from zero to infinity, rather than over $\mathcal{E}$ from χ_0 to infinity. The integral will give the number of electrons in the volume $\frac{1}{n_{11}}$, which is $\frac{n_e}{n_{11}}$, as

$$\frac{n_e}{n_{11}} = \int_{p=0}^{\infty} \left(g_{11}\frac{2}{h^3}4\pi p^2 dp \frac{1}{n_{11}}\right)\left(\frac{n_{01}}{n_{11}g_{01}}\right) e^{-\frac{\chi_0}{kT}} e^{-\frac{p^2}{2m_e kT}} \quad \text{(A.11)}$$

This is rewritten as

$$n_e = \frac{2(4\pi)}{h^3}\frac{g_{11}}{g_{01}}\frac{n_{01}}{n_{11}} e^{-\frac{\chi_0}{kT}} \int_0^{\infty} p^2 e^{-\frac{p^2}{2m_e kT}} dp \quad \text{(A.11a)}$$

Integration gives

$$n_e = \frac{2(4\pi)}{h^3}\frac{g_{11}}{g_{01}}\frac{n_{01}}{n_{11}} e^{-\frac{\chi_0}{kT}} \left[(2m_e kT)^{3/2}\frac{\pi^{1/2}}{4}\right] \quad \text{(A.12)}$$

Now apply Equation A.5 for α equal to zero and one, and β equal to one; the result gives Saha's ionization equation as

$$\frac{n_e n_1}{n_0} = \frac{2B_1(T)}{B_0(T)}\frac{(2\pi m_e kT)^{3/2}}{h^3} e^{-\frac{\chi_0}{kT}} \quad \text{(A.13)}$$

This is the Saha thermal-ionization equation in its most general form, involving the minimum of restrictive assumptions. When this equation is encountered in the literature, it is usually in a modified form. Often the electron density is replaced by electron pressure by use of the ideal gas law, $P_e = n_e kT$. Also, one occasionally sees the

equation with n_e set equal to n_i ; this latter modification requires electrical neutrality and the presence of only one type of ionizing element, and limits the application of the equation to one stage of ionization only. Finally, the equation is frequently seen in terms of logarithms to the base ten. In this case the terms on the left side of Equation A.13 are replaced by their equivalents in terms of the fractional degree of ionization and the total pressure; this procedure involves assuming that the ideal gas law and the law of partial pressures apply and therefore may limit the general applicability of the equation.

As given in the form of Equation A.13, the Saha equation is readily adaptable to several forms of the problem of thermal ionization. It describes the relative population in any ionization level, say the n^{th} level, to the population in the n+1 level. Therefore, a series of Saha equations can describe an ionized gas containing particles in any number of ionized levels. This procedure is not often necessary, however, since Russell has shown that for a gas containing only a single element capable of several levels of ionization, atoms in only two adjacent levels will be present in appreciable numbers at any one time (64). If the partition functions in Equation A.13 are replaced by the statistical weights of the ground states of the atom and ion, then the populations of the ground states of the atom and ion are obtained. Finally, one may show that the Saha equation contains the Boltzmann relation by treating the atom in its ground state and in its first excited state as two separate atom types having different ionization potentials. Applying the Saha equation to the ionization from these two levels will give the Boltzmann relation for the two lower levels of the atom.

APPENDIX B

LIST OF REFERENCES

1. Suits, C. G., "The Determination of Arc Temperature from Sound Velocity Measurements," Physics, 6, 190 (1935).

2. Suits, C. G., "A Study of Arc Temperatures by an Optical Method," Physics, 6, 315 (1935).

3. Suits, C. G., "High Pressure Arcs in Common Gases in Free Convection," Physical Review, 55, 561 (1939).

4. Burhorn, F., Maecker, H., and Peters, T., "Temperaturmessungen am wasserstabilisierten Hochleistungsbogen," Zeitschrift für Physik, 131, 28 (1951).

5. Peters, T., "Temperatur- und Strahlungsmessungen am wasserstabilisierten Hochdruckbogen," Zeitschrift für Physik, 135, 573 (1953).

6. Elenbaas, W., The High Pressure Mercury Vapor Discharge (North-Holland Publishing Co., Amsterdam, 1951).

7. Anderson, J. A., and Smith, S., "General Characteristics of Electrically Exploded Wires," Astrophysical Journal, 64, 295 (1926).

8. Conn, W. M., "Studien zum Mechanismus von elektrischen Drahtexplosionen," Zeitschrift für angewandte Physik, 7, 539 (1955).

9. Eiselt, B., "Über den Ablauf von Drahtexplosionen," Zeitschrift für Physik, 132, 54 (1952).

10. Glaser, G., "Über die Erzeugung sehr hoher Temperaturen im Hochleistungsfunken," Zeitschrift für Naturforschung, 6A, 706 (1951).

11. Glaser, G., "Zur Lichtemission stromstarker Funkenentladungen," Optik, 7, 33, 61 (1950).

12. Angerer, E., and Joos, G., "Die Absorptionsspektren der Elemente der Eisengruppe," Annalen der Physik, 379, 743 (1924).

13. Wilson, E. D., "Temperature of the Underwater Spark As Computed from Distribution of Intensity in OH Absorption Bands," Journal of the Optical Society of America, 17, 37 (1928).

14. Wyneken, I., "Die Energieverteilung im kontinuierlichen Spektrum des Aluminium-Unterwasserfunkens," Annalen der Physik, 86, 1071 (1928).

15. Slepian, J., Denault, C. L., and Strom, A. P., "Dielectric Strength of Water in Relation to Its Use in Circuit Interrupters," Transactions of the American Institute of Electrical Engineers, 60, 389 (1941).

16. Früngel, F., "Zum mechanischen Wirkungsgrad von Flüssigkeitsfunken,"

Optik, 3, 124 (1948).

17. Rust, H. H., and Drubba, H., "Praktische Anwendung des Unterwasserfunkens als Impuls-Schallgeber für die Echolotung," Zeitschrift für angewandte Physik, 5, 251 (1953).

18. Jenkins, F. A., and White, H. E., Fundamentals of Physical Optics (McGraw-Hill, New York, 1937).

19. Glasoe, G. N., and Lebacqz, J. V., Pulse Generators, Vol. 5, M.I.T. Radiation Laboratory Series (McGraw-Hill, New York, 1948).

20. Ende, W., "Beitrag zur Kenntnis der Kurzschlussfunken," Annalen der Physik, 17, 460 (1933).

21. Kleen, W., "Über den Durchgang der Elektrizitat durch metallische Haardrahte," Annalen der Physik, 403, 579 (1931).

22. Nagaoka, H., and Futagami, T., "Electric Explosions," Scientific Papers of the Institute of Physical and Chemical Research (Tokyo), 8, 269 (1928).

23. Lord Rayleigh, F. R. S., "On the Instability of Jets," Proceedings of the London Mathematical Society, 10, 4 (1878).

24. (no author), "Russian Thermonuclear Experiments," Nucleonics, 14, 36 (1956).

25. Meek, J. M., and Craggs, J. D., Electrical Breakdown of Gases (Oxford University Press, London, 1953).

26. Bridgman, P. W., The Physics of High Pressures (Bell and Sons, London, 1949).

27. Truesdell, C., "Precise Theory of the Absorption and Dispersion of Forced Plane Infinitesimal Waves According to the Navier-Stokes Equations," Journal of Rational Mechanics and Analysis, 2, 643 (1953).

28. Courant, R., and Friedrichs, K. O., Supersonic Flow and Shock Waves (Interscience Publishers, New York, 1948).

29. Cole, R. H., Underwater Explosions (Princeton University Press, New Jersey, 1948).

30. Evans, G. W. Faulkner, F. D., Lockhart, B. I., and Perry, C. L., "Shock Produced by a Spherical Piston of Radius a(t)," Stanford Research Institute Project No. PU-1123, (Stanford Research Institute, Stanford, California, June, 1954, to May, 1955).

31. Schaaffs, W., "Untersuchungen an Funkenschallwellen mit Hilfe von Röntgenblitzen," Zeitschrift für Naturforschung, 4a, 463 (1949).

32. Wahr, J. C., McCormick, W. W., and Sawyer, R. A., "Relative Time Dependence of the Emission of Line and Background from the Vacuum Spark," Journal of the Optical Society of America, 43, 805 (1953).

33. Finkelnburg, W., Atomic Physics (McGraw-Hill, New York, 1950).

34. Finkelnburg, W., Kontinuierliche Spektren (Julius Springer, Berlin, 1938).

35. Cobine, J. D., Gaseous Conductors (McGraw-Hill, New York, 1941).

36. Edels, H., "The Determination of the Temperatures of an Electrical Discharge in a Gas," Report L/T 230, British Electrical and Allied Industries Research Association, London, England, 1950.

37. Sawyer, R. A., Experimental Spectroscopy (Prentice-Hall, New York, 1944).

38. Forsythe, W. E., "Optical Pyrometry," Temperature, Its Measurement and Control in Science and Industry, 1939 Symposium of the American Institute of Physics (Reinhold Publishing Corp., New York, 1941).

39. Forsythe, W. E., and Worthing, A. G., "The Properties of Tungsten and the Characteristics of Tungsten Lamps," Astrophysical Journal, 61, 146 (1925).

40. Aller, L. H., Astrophysics, the Atmospheres of the Sun and Stars (Ronald Press, New York, 1953).

41. Churchill, R. V., Modern Operational Mathematics in Engineering (McGraw-Hill, New York, 1944).

42. Vosmaer, A., Ozone, Its Manufacture, Properties, and Uses (D. van Nostrand, New York, 1916).

43. Linder, E. G., "Dissociation of Water in the Glow Discharge," Physical Review, 38, 687 (1931).

44. Gibson, G. E., and Heitler, W., "Die chemische Konstante in der neuen Quantenstatistik," Zeitschrift für Physik, 49, 465 (1928).

45. Stuart, H. A., Molekulstruktur (Julius Springer, Berlin, 1934).

46. Fowler, R. H., Statistical Mechanics, Second Edition (Cambridge University Press, Cambridge, 1936).

47. Moore, C. E., Atomic Energy Levels, Volume I (National Bureau of Standards Circular No. 467, Government Printing Office, June, 1949).

48. Attwood, S. S., Electric and Magnetic Fields, Third Edition (John Wiley and Sons, New York, 1949).

49. Slater, J. C., Introduction to Chemical Physics (McGraw-Hill, New York, 1939).

50. Pines, D., and Bohm, D., "A Collective Description of Electron Interactions: Collective versus Individual Particle Aspects of the Interactions," Physical Review, 85, 338 (1952).

51. Dow, W. G., Fundamentals of Engineering Electronics, Second Edition (John Wiley and Sons, New York, 1952).

52. Maecker, H., "Der elektrische Lichtbogen," Ergebnisse der exakten Naturwissenschaften, 25, 310 (1951).

53. Spitzer, L., and Harm, R., "Transport Phenomena in a Completely Ionized Gas," Physical Review, 89, 977 (1953).

54. Hocker, V. K., and Schulz, P., "Über die Wärmeleitung in der Hochstrombogensäule," Zeitschrift für Physik, 4A, 266 (1949).

55. Early, H. C., and Martin, E. A., "The Underwater Spark, A Light Source of High Intrinsic Brilliance," Communication and Electronics, A. I. E. E., No. 22, 788 (1956).

56. Pugh, E. M., Heine-Geldern, R., Foner, S., and Mutschler, E. C., "Glass Cracking Caused by High Explosives," Journal of Applied Physics, 23, 48 (1952).

57. Goranson, R. W., Bancroft, D., Burton, B. L., Blechar, T., Houston, E. E., Gittings, E. F., and Landeen, S. A., "Dynamic Determination of the Compressibility of Metals," Journal of Applied Physics, 26, 1472 (1955).

58. Walsh, J. M., and Christian, R. H., "Equation of State of Metals from Shock Wave Measurements," Physical Review, 97, 1544 (1955).

59. Rinehart, J. S., and Pearson, J., Behavior of Metals Under Impulsive Loads (American Society for Metals, Cleveland, 1954).

60. Saha, M. N., "Ionization in the Solar Chromosphere," London Philosophical Magazine, 40, 472 (1920).

61. Zemansky, M. W., Heat and Thermodynamics, Third Edition (McGraw-Hill, New York, 1951).

62. Menzel, D. H., "A Simple Derivation of the Dissociation Formula," Proceedings of the National Academy of Sciences, 19, 40 (1933).

63. Gurney, R. W., Introduction to Statistical Mechanics (McGraw-Hill, New York, 1949).

64. Russell, H. N., "The Theory of Ionization and the Sun Spot Spectrum," Astrophysical Journal, 55, 124 (1922).